POLITECNICO DI TORINO

Master of Science's Degree in Aerospace Engineering

Master Thesis

Numerical simulation of high-speed and high temperature reacting flows using a commercial CFD software

Relatore
Domenic D'Ambrosio

Studente
Salvatore Esposito

Summary

Hypersonic flows are a field of great interest since the sixties of last century because they occur in the planetary entry of space probes and they have recently attracted renovated attention due to development of hypersonic cruise missiles. Currently, the dominating method of study for high Mach number flows is Computational Fluid Dynamics (CFD), which have become sufficiently powerful, and have replaced the old analytic methods. In the present work, a computational model has been developed for simulating flows of a multicomponent air mixture around a hypersonic cruise missile (HCM) using the commercial CFD software STAR-CCM+. The investigations aim at verifying, first of all, the effective occurrence of chemical reactions of an air mixture of eleven species (N, N_2, O, O_2, NO, N^+, O^+, N_2^+, O_2^+, NO^+, e^-), then to evaluate the possible presence of the ionized particles species and finally to assess whether their amount is high enough to generate an appreciable electric field or not. The software set-up choices were made to match assumptions required for analytical models which describe aerothermo-chemical effects in the proximity to the missile nose. Starting from a Mach number equal to 10, several simulations have been carried out, applied to the basic geometry of the nose, and different thermo-chemical models have been considered. Furthermore, since the considered model included a multicomponent gas mixture, multicomponent diffusive mechanisms have been implemented, where binary diffusion coefficients and gradients of temperature effects have been considered. Good convergence of solution was observed for all cases presented since every investigation has been carried out with a proper numeric discretization scheme and fine enough grids to avoid numerical instabilities and to guarantee adequately accurate results. The investigations showed the occurring of reactions and revealed the appearance of ionized particles. These phenomena strongly affect flow field properties. Reactions influence heat flow at wall in stagnation region, while a distribution of charged particles induces an electric field which may give to the missile a stealth property, as well as conditioning transport mechanisms. These considerations make hypersonic flow fields fundamental to investigate and our results confirmed how significant thermo-chemical effects are for HCMs features.

Contents

List of Tables

List of Figures

[empty]

Chapter 1

Overview

1.1 Introduction

The hypersonic flows have been studied for decades under a variety of interests, spacing from entry vehicle, through civil transportation, till modern hypersonic weapons. However all the aerospace vehicles and weapon, that operate within this regime are strongly affected by the profound aero-thermochemical phenomena that are encountered at such high speeds. Understanding processes induced by high speeds requires, not only knowledge of aerodynamics but also of heat transfer and chemistry. Flow fields in hypersonic regime are, in fact, much different from the ones experienced in supersonic aerodynamics. High temperatures, induced by shockwaves in hypersonic regime, trigger thermo-chemical processes which strongly changes the characteristics of the flow field. Phenomena such as vibrational excitation, dissociation and ionization, affect the chemical composition of air and its properties, adding complexity to the physical problem and making the hypersonic flight a difficult case to model. However, as computational tools develops, utilizing Computational Fluid Dynamics (CFD) and multi-physics modeling has made the study of hypersonic flow fields more affordable. A commercial CFD software will be used in this work to study the properties of the flow field surrounding a Hypersonic Cruise Missile (HCM), through the development of a computational model able to point out the thermo-chemical processes induced by high temperatures. In particular, the primary aim is to verify the occurrence of chemical reactions even for a relatively low Mach number (equal to 10), since thermo-chemical phenomena require higher speeds to be observed. After this assessment, the aim will be directed towards the presence of a electrically charged species in air whose sufficient amount may generate a substantial electric field, able to affect flow field properties. Finally, a benchmark analysis is carried out and the limits of the developed model are highlighted.

1.2 Thesis Outline

The present thesis is structured as follow:

- Chapter 2 gives an overview of the current hypersonic technologies, pointing out shapes, operational conditions of vehicles and weapons;
- Chapter 3 presents physical models which properly describe hypersonic flows. Governing equations, high temperature effects and diffusion mechanisms for viscous multi-species flows will be detailed;
- Chapter 4 discusses the adopted computational models and numerical procedures;
- Chapter 5 reviews the solution obtained from the simulations carried out via method described in Chapter 4 and the results of the benchmark analysis are discussed;
- Chapter 6 is intended to the conclusions.

Chapter 2

Hypersonic technologies

2.1 Intro

This chapter briefly describes the current hypersonic technologies. The main features of new vehicles are pointed out in the following sections, focusing the attention on missions, trajectories, operational conditions, quote and typical shapes of modern hypersonic technologies. However, it is firstly necessary to highlight under which conditions an hypersonic flow field develops.

2.2 About the Hypersonic

Anything that moves in a fluid (air) is subjected to fluid dynamics (aerodynamics) forces. Depending on the Mach number (speed and speed of sound ratio), several regimes can be identified with different features of the flow field. Flying vehicles and missiles indeed, can travel in three different Mach ranges:

- subsonic regime (M<1)
- supersonic regime (M>1)
- hypersonic regime (M>5)

Speed regime	Mach	Km/h	Application
Subsonic	<0.8	<980	Commercial aircraft, turbofan, turbojet planes
Transonic	0.8-1.2	980-1470	Jet aircraft, cruise missiles
Supersonic	1.2-<5	6150–12.300	Aircraft, cruise missiles, anti-missile systems
Hypersonic	5.0-10.0	12300–30740	Re-entry vehicle, short-range ballistic missile, hypersonic cruise missiles,hypersonic aircraft, intercontinental ballistic missile,boost-glide vehicles
High-Hypersonic	10.0-25.0	>30740	Re-entry vehicle, ICBM, advanced hypersonic vehicles, boost-glide vehicles

Table 2.1: "Categories" of speed

An object which moves slower than the speed of sound of its surrounding fluid (typically air) is said to be in the subsonic regime. Large modern airliners travel at the limit of the subsonic regime. A body, instead, travelling faster than the speed of sound is said to be in the supersonic regime. Anyway, there is not a tangible barrier above which the flow changes from being supersonic to hypersonic but there are new phenomena to be taken into account. In this case, the physics of the problem is dominated by aerodynamics heating due to the viscous dissipation. However,according to conventions[11], fluid dynamic or aerodynamics problems are considered as hypersonic when the Mach number exceeds five

(M>5), and so the characteristic speed is five times bigger than the speed of sound. In addition, the speed regime can be divided into two parts: the speeds in the range from Mach 5 to Mach 10 referred as the 'hypersonic speeds', and the ones in the range from Mach 10 to Mach 25 are known as 'high-hypersonic speeds'. Some useful details about "categories of speed" are presented in the table 2.1 [17].

2.3 Hypersonic weapons

Over the years, a significant progress has been made to guarantee that flying vehicles (manned or unmanned) move with higher speeds and, eventually, greater manoeuvrability. In the following discussion about the Hypersonic, the words vehicle/s and weapons are used interchangeably. In fact, the line between hypersonic vehicles and missiles is very thin: hypersonic vehicles, as it will be shown later, have so much kinetic energy that they can be assumed as effective weapons. The strategic utility on hypersonic technology is currently focused on the missiles development rather than vehicles occupied by humans. However, private industry is known to be working on space planes and manned vehicles in order to support space tourism. These hypersonic platforms can be propelled by different kind of engines: rocket-based or air-breathing systems. The latters involve high-speed propulsion (supersonic combustion) that is a scramjet, considered as an advanced air-breathing ramjet. These air-breathing propulsion systems offer several advantages than the formers, such as a rapid response at long range, a better manoeuvrability and an assured access to space[18]. Rocket boosters instead, have been used to propel hypersonic vehicles for different applications: space launch, long range ballistic flight and air defence interceptor missiles. Presently, there are two types of hypersonic weapons under development:

- Hypersonic Glide Vehicles (HGVs)
- Hypersonic Cruise Missiles (HCMs)

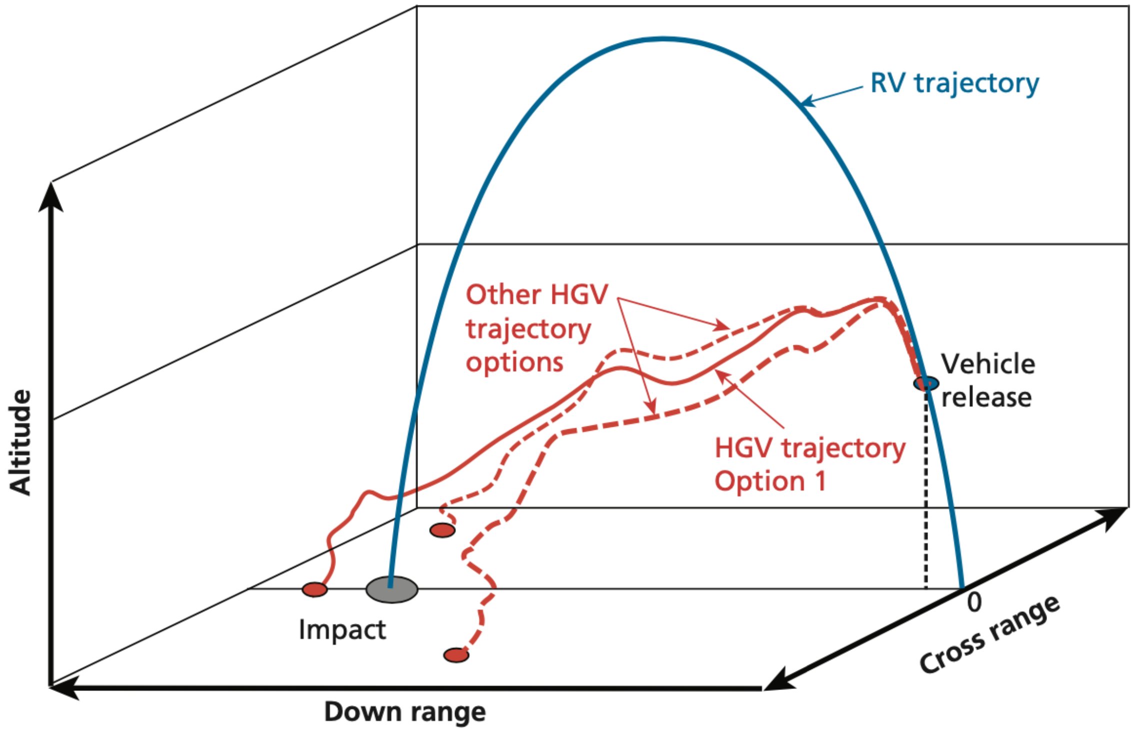

Figure 2.1: Ballistic Reentry Vehicle (RV) Versus HGV Trajectories [4]

The firsts are typically launched by rockets into the upper atmosphere and released at altitudes ranging from 40 Km to higher than 100 Km. These weapons glide to their targets by skipping along the upper atmosphere. The seconds instead, are powered all the way to their targets by rockets or high-speed jet engines. As it can be seen in the Fig 2.1, the HGVs can vary their impact point and associated trajectory during its flight time and they fly at lower altitudes compared with ballistic missiles. These features make the hypersonic much more threatening than the actual existing missiles.

2.3.1 Hypersonic glide vehicles

HGVs are unpowered vehicles that «glide» to their target at the «top» of the atmosphere, reaching between about 40km to 100 km in altitude [19]. Although the rarefied atmosphere, they are designed to produce lift that is equal to their weight to keep them aloft at hypersonic speed. These weapons are typically launched on a ballistic missile and released at the appropriate altitude, velocity and flight path angle in order to glide to their target [4]. The HGV trajectories are very different from maneuvering reentry vehicles (MaRVs) developed in the past. The MaRV trajectory, in fact, is mostly in ballistic mode, in contrast, an HGV spends a negligible portion (if any) of its flight in this state.

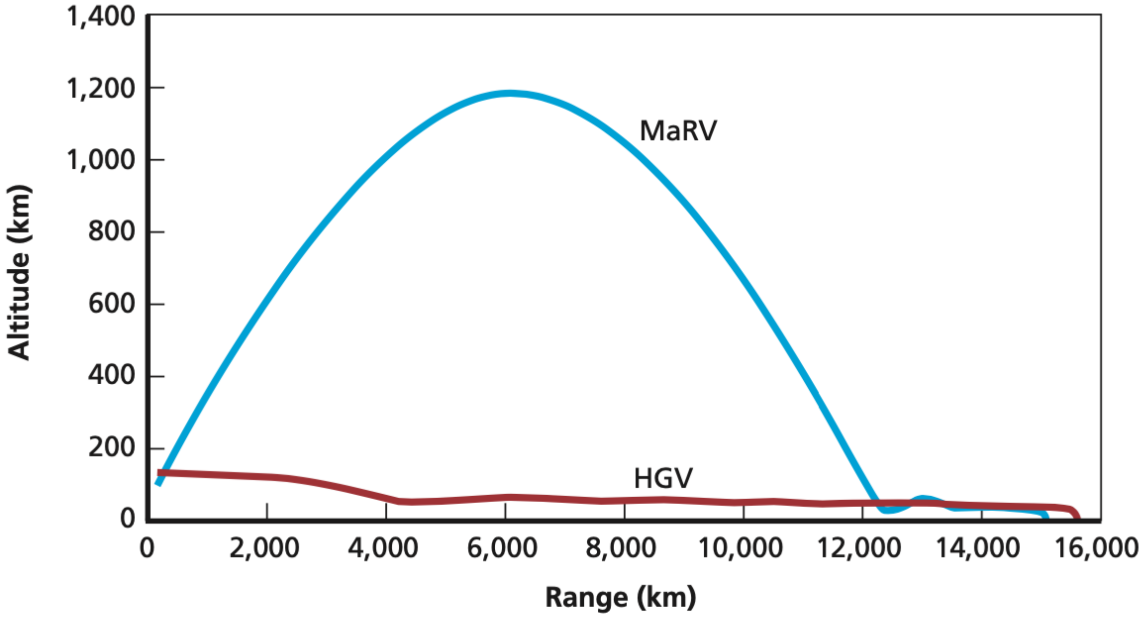

Figure 2.2: Typical HGV and MaRV Trajectories [4]

From an offensive perspective, maneuverability can potentially provide HGVs the ability to use in-flight updates to attack different target than originally planned. Thanks to the ability to fly at unpredictable trajectories, these missiles will hold extremely large areas at risk throughout much of their flight. Even though HGVs are usually not powered, a small propulsion system providing additional velocity or some attitude or directional control could also be integrated into the vehicle. However, the value of such an engine would need to be traded against the costs associated with additional weight and added complexity. So, HGVs have the reach and speed of ballistic missiles, but, unlike these ones, they fly at lower altitudes and have relatively unpredictable trajectories that can include significant cross-range and terminal maneuvers. These characteristics make HGVs challenging to defend against since they tend to fly outside the altitude and speed envelopes of modern air and missile defense systems. They can overwhelm current ballistic missile defense systems because of their unpredictable long-range trajectories, maneuverability and flight altitudes. Thus, nations with no space-based sensor system to detect ballistic missile launches and that have only ground-based sensors, such as radars, could see a further compression of their decision/response timelines. The reason is that typical ballistic missiles generally fly at higher altitudes than HGVs and should therefore be detectable earlier. Radars or other line-of-site sensors are not able to detect an HGV as early as they would a ballistic missile because of the Earth's curvature and the HGV low altitude [19].

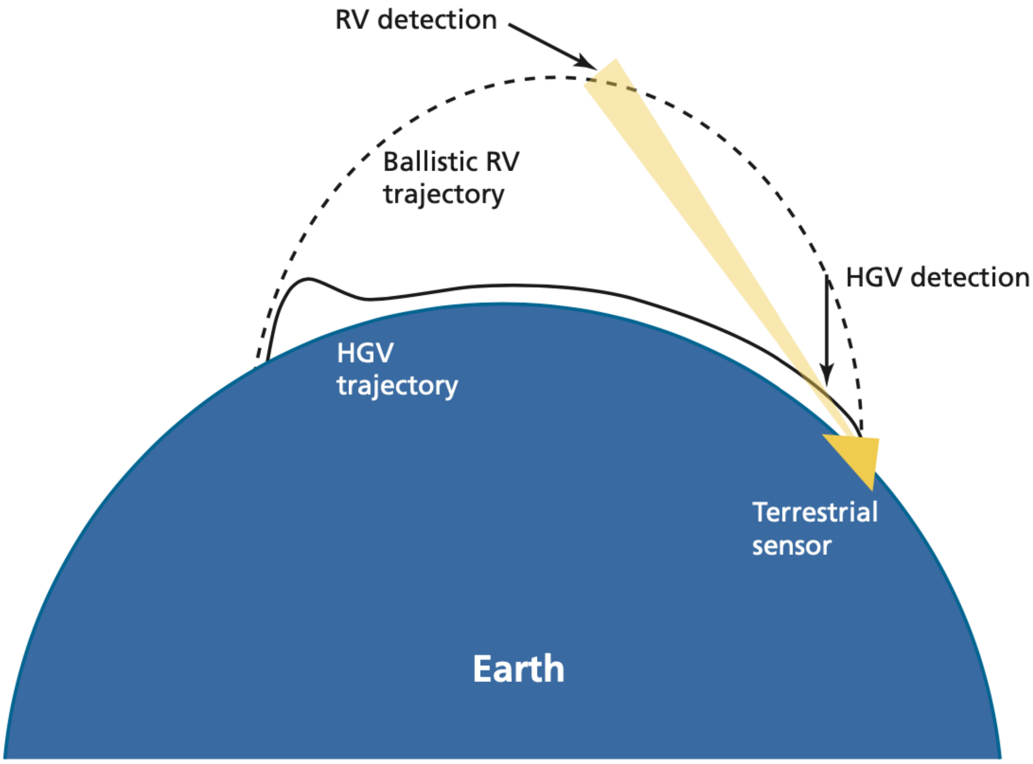

Figure 2.3: HGV Versus RV Terrestrial-Based Detection [4]

2.3.2 Hypersonic cruise missile

An HCM is a cruise missile that travels at hypersonic speeds. As such, it reduces the defense response timeline and hinders many of the modern defense systems because of its high speed and maneuverability. Hypersonic missiles could be launched from the ground, from aircrafts or from ships. An HCM is propelled in order to achieve a Mach 4 or 5 and then, in general, an air breathing engine (scramjet generally) capable of producing thrust at hypersonic speeds, accelerates it and then maintains the missile's speed. There are several options for propelling an HCM up to Mach 4 or 5. Because of their simplicity and affordability, rocket boosters are the most used option especially for the early generation HCMs, even though they may be the largest and the heaviest option since they have to carry both their propellant and oxidizer. Any option to accelerate the missile needs to be feasible and affordable, because it is a one-time-use propulsion system. Moreover, it needs to reach appropriate pressures for combustion in the scramjet engine, that's why an HCM will cruise at an altitude of 20-30 km. The principal advantages of an HCM, as above, are its speed and maneuverability. These two together, provide a very rapid and flexible offensive weapon that could, for example, point targets within a 1000 Km radius of the launch aircraft and could strike these targets within few minutes. The high maneuverability also makes cruise missiles difficult to defend against because their trajectories become unpredictable. The high speed provided by an HCM, complicates defense system timelines, furthermore they fly at altitudes higher than the ones reached by the most of current surface-to-air missile systems. Even though interceptors could be designed to fly higher,they still would need to confront the HCM speed and maneuverability. As it will be pointed out shortly, an HGV high kinetic energy has significant destructive power, even without an explosive warhead [17].

2.3.3 Destructive power

Hypersonic weapons can carry nuclear or conventional warheads. However, HCMs and HGVs are able to take advantage of the solely kinetic energy to destroy or damage targets. This is made possible thanks to the combined high speed and accuracy. In fact, their high impact speed could also be used to destroy underground facilities. Fig 2.4 provides a rough estimate of the effective explosive TNT equivalence of a high-speed mass, such as a conventional strike vehicle with no on-board explosives. It is assumed that energy is directed and focused along projectile direction and frontal area [4].

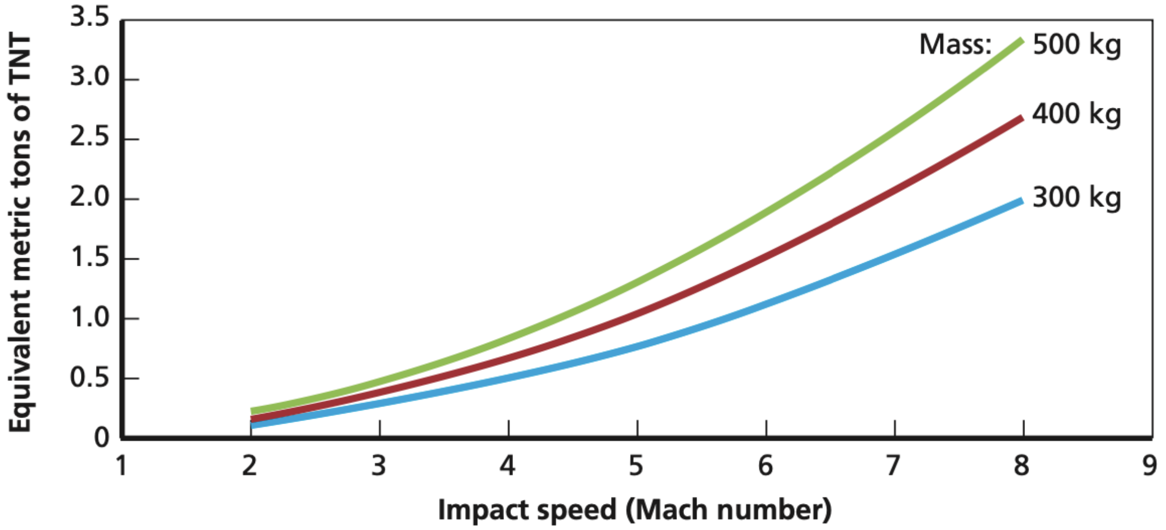

Figure 2.4: Destructive Power of a High-Speed Mass as a Function of Speed [4]

2.4 State of the art

Several countries are developing hypersonic weapons, but none of them has been introduced in their military forces yet. Among the countries which are focused on the hypersonic technologies, Usa, Russia and China are (almost) the only ones which have reached successful results.

2.4.1 United States

Presently, the Department of Defense is developing hypersonic weapons under the Navy's Conventional Prompt Strike program, which is focused on providing the U.S military with an ability to strike hardened or time-sensitive targets using conventional warheads, DARPA programs and army [20]. U.S hypersonic weapons will require much more accuracy and will be much more technically challenging to develop, due to the fact that the project does not involve nuclear warhead. In fact, according to experts "a nuclear-armed glider would be effective if it was 10 or 100 times less accurate than a conventionally-armed glider" due to the nuclear blast effects [21]. According to open-source reporting, United States has different offensive hypersonic weapons and hypersonic technology developing programs [22]:

- U.S Navy-Conventional Prompt Strike (CPS);
- U.S. Army—Long-Range Hypersonic Weapon (LRHW);
- U.S. Air Force—AGM-183 Air-Launched Rapid Response Weapon (ARRW, pronounced “arrow”);
- DARPA—Tactical Boost Glide (TBG);
- DARPA—Operational Fires (OpFires);

- DARPA—Hypersonic Air-breathing Weapon Concept (HAWC, pronounced “hawk”).

The CPS program is expected to design a missile comprised of a Common Hypersonic Glide Body (C-HBG) launched by a submarine booster system [23], meanwhile the Army’s LRHW introduces a new long-range missiles launched from mobile ground platforms. More precisely, the program is intended to pair the Common glide vehicle with the Navy’s booster [24]. The ARRW instead, is intended to leverage DARPA’s tactical boost glide technology to develop an air launched hypersonic glide vehicle prototype capable of travelling at speeds up to Mach 20 at a range of approximately 575 miles [25]. DARPA, in partnership with the Air Force, aims to develop a Tactical Boost Glide, a wedge-shaped hypersonic glide vehicle able to operate a Mach 7 flight. In a boost glide system, a rocket accelerates its payload to high speeds and then, the payload then separates and glides unpowered to its target.the TBG program focuses on three primary objectives which are: vehicle feasibility, effectiveness and affordability [26, 27] DARPA’s Operational Fires program is focused on the exploitation of the TBG technologies to create a ground-launched system which will enable «advanced tactical weapons to penetrate modern enemy air defenses and rapidly and precisely engage critical time sensitive targets»,from [28]. In the longer term, DARPA, with Air Force support, is keeping on working on the Hypersonic Air- breathing Weapon Concept, which «seeks to develop and demonstrate critical technologies to enable an effective and affordable air-launched hypersonic cruise missile» [29]. DARPA Falcon Project provides for the development of an experimental hypersonic glide vehicle capable of flying at Mach number up to 20. The Falcon HTV-1 flight test was cancelled in 2006 due to difficulties manufacturing with the curved leading edges of carbon-carbon aeroshell. The design efforts shifted to the HTV-2 which features a multi-piece aeroshell with thinner leading edges. [30] Flight tests were stopped by DARPA since the data collected was substantial and, after the crash during the second flight, a third test to collect additional information was to be considered too expensive. The first flight test provided indeed, data in aerodynamic and flight performance, while the second provided information about structures and high temperatures.[31] Presently, the project which has returned the most promising results is the Boeing X-51A, a vehicle propelled by a scramjet engine to travel at hypersonic speeds. The WaveRider project has been developed thanks to a collaboration among Boeing, NASA, DARPA, USAF and PW Rocketdyne [32] . During tests, the X-51A was carried at height of 15 Km by a SRBM (short range ballistic missile) with a Mach number of 4.5, then it was propelled by the scramjet engine up to a Mach number of 5.1. In the following table there are some details about the X-51 [33].

Figure 2.5: X-51 under a B-52
Source:U.S. Air Force photo/Chad Bellay

Figure 2.6: X-51 Render
Source: United States Air Force Research Laboratory

Boeing-X51	WaveRider
Length	7,9 m
Empty weight	1814 Kg
Mach reached during the test	5,1
Expected Mach	7
Propulsion	Hydrocarbon-scramjet
Deploying altitude	15-18 Km
Carried by	MGM-140 ATACMS, B-52

Table 2.2: X-51 main features

2.4.2 Russia

Russia is currently pursuing several hypersonic weapons programs:

- Avanguard
- 3M22 Tsirkon (Zirkon)
- Kinzhal

Avangard

Avangard is an hypersonic glide vehicle launched from an intercontinental ballistic missile. The HGV is deployed on the SS-10 IBCM but Russia is planning to launch the vehicle from the Sarmat ICBM [34].

Avangard	HGV
Length	5,4
Speed	33400 Km/h
Warhead	Nuclear, hardened materials (kinetic weapons), conventional.
Propulsion	scramjet
Range	10000 Km
Carried by	ICBM(RS-28 Sarmat,R-36M2,UR-100UTTKh)

Table 2.3: Avangard main features

3M22 Zirkon

Zirkon is a ship-launched hypersonic cruise missile equipped with a solid rocket booster which propels it up to supersonic speed, and with a scramjet engine which makes the missile able to reach hypersonic speeds. During flight, the missile is completely covered by a plasma cloud that absorbs any rays of radio frequencies and makes the missile invisible to radars [35].

3M22 Zirkon	HCM
Length	8-10 m
Maximum Mach	8-9
Warhead	Unknown
Stages/propellant	2, solid, liquid propellant scramjet
Operational Range	1000-2000 Km (depend on type target)
Launch platform	Submarine, surface ship

Table 2.4: Zirkon main features[1]

Kinzhal

Kinzhal is a maneuvering air launched ballistic missile capable of reaching a Mach number of 10. Presently, the only Kinzhal's vector is the supersonic interceptor MiG-31BP. This missile is powered by a rocket solid booster and it's capable of maneuverable flight, as well as of striking both ground and naval targets and it could eventually be fitted with a nuclear warhead. [36]

Kh-47M2 Kinzhal	HCM
Length	8 m
Flight ceiling	20 Km
Maximum Mach	10-12
Warhead	Nuclear, conventional
Warhead weight	500 Kg
Stages/propellant	1, solid
Accuracy	1m
Operational Range	2000-3000 Km
Launch platform	MiG-31K,Tu-22M3M

Table 2.5: Kinzhal main features [2]

Figure 2.7: Kinzhal carried by a MiG-31K interceptor [5]

Figure 2.8: Rendering of Zirkon in flight
Source: Missile Defense Advocacy Alliance

2.4.3 China

China is known to be developing various advanced weapons for several years and its major investment has been made in hypersonic gliders[37]. The Chinese hypersonic vehicles is known as the WU-14 or DF-ZF. The glider is mounted on the medium range ballistic missile(MBRM) DF-17 and it is not known to be using a scramjet technology. The conduction of seven tests within a span of less than two years indicates China's commitment to the development of this technology [38]. The DF-ZF HGV could also have the capability of being launched a top an anti-ship ballistic missile to target naval assets. For example, a DF-21 armed with a DF- ZF HGV may extend the missile's range from 2000 to over 3000 km [39]. According to U.S. defense officials, China also successfully tested Starry Sky-2 , a WaveRider that uses powered flight after launch and derives lift from its own shockwaves [40]. No technical details are currently available for these two weapons.

2.4.4 Hypersonic technological development and cooperation among other countries

India and France

There are other two governments which are currently focusing on the research and development of hypersonic technology: France and India. They rely intensely on cooperation with Russia to achieve an higher level of technological development. France is putting its effort to achieve an hypersonic missile technologies, testing the ASN4G, capable of carrying a nuclear warhead. The missile is being developed by ArianeGroup and it is thought to be operational by 2021 [41]. France's cooperation with Russia, instead, expects flight tests of the LEA (Russian acronym for flight test vehicle) vehicle launched from a Russian bomber. ti's still not clear if these tests actually occurred. The program still lists as active and it results as actually carried on by MBDA and ONERA. India's cooperation with Russia gave birth to BrahMos II, an hypersonic cruise missile to be used in a antiship role, which is said to be an adaption of Russia's Tsirkon hypersonic missile [42]. Furthermore,as indigenous hypersonic research and development, India succeeded in test-firing the missile Shaurya, an hypersonic tactical missile, on 3 October 2020 for the third time. Some technical details in the Table 2.6:

Shaurya	Hypersonic surface-to-surface tactical missile
Length	10 m
Mass	6,2
Diameter	0,74 m
Warhead	Nuclear, conventional
Warhead weight	200-1000 Kg
Stages/propellant	2,solid rocket motor
Accuracy	20-30 m
Operational Range	700-1900 Km
Flight altitude	50 Km
Launch platform	canisterised transporter erector launcher, underground silo
Maximum Mach	7,5

Table 2.6: Shaurya technical details[3]

Figure 2.9: BrahMos II model
Source:Shiv Aroor via Wikimedia Commons

Figure 2.10: Shaurya missile [6]

Australia

Thanks to the researchers of hypersonic at the University of Queensland, Australia presently participates in a series of collaboration on scramjet technology with the United States and Europe. In particular, the

Hypersonic International Flight Research Experimentation (HIFiRE) is a long standing collaborations on scramjet technology with the U.S Air Force [43]. Affordable testes of scramjet prototypes at speed of up to Mach 7,5-8 were launched in 2016. However, Australia's indigenous hypersonic researches have encountered several problems and have seen a reduction in funding over the years [44, 45].

Figure 2.11: Australian-U.S HIFiRE Scramjet
Source:Australian Hypersonics Initiative at the University of Queensland, Australian Defence Science and Technology Group, and U.S. Air Force Research Laboratory.

Japan

JAXA (Japan Aerospace Exploration Agency) pursued creation of an hypersonic commercial aircraft capable of travel at Mach 5. More over, Japan is partner in the Hikari program (High Speed Key Technologies for Future Air Transport Research and Innovation) with the European Commission. This program was expected to be return experimentation for a hypersonic vehicle by 2020 [46]. Instead, Japan's indigenous hypersonic research on a experimental aricraft (HyTEx program), a commercial vehicle capable of flying at speeds of up to Mach 5, is still long way from achieving tangible results [47].

European Union

The European Union has put its efforts in three research and development programs:

- LAPCAT II, Long-Term Advanced propulsion Concepts and Technologies;
- IXV, Intermediate eXperimnetal Vehicle;
- ATLLAS II, Aero-Thermodynamic Loads on Lightwight Advanced Structures.

LAPCAT II is focused on the development of a civilian transport airplane which can travel at speeds up to Mach 5 using an hybrid turbo-scramjet engine. IXV is a program funded by ESA (European Space Agency) and it is based on testing atmospheric reentry conditions from hypersonic orbital speed and trajectories. ATLLAS II supports these efforts: it is indeed a program aimed at the project, development and design of lightweight, high-temperature materials [48].

Figure 2.12: Japanese HyTex
Source: promotional photo from JAXA

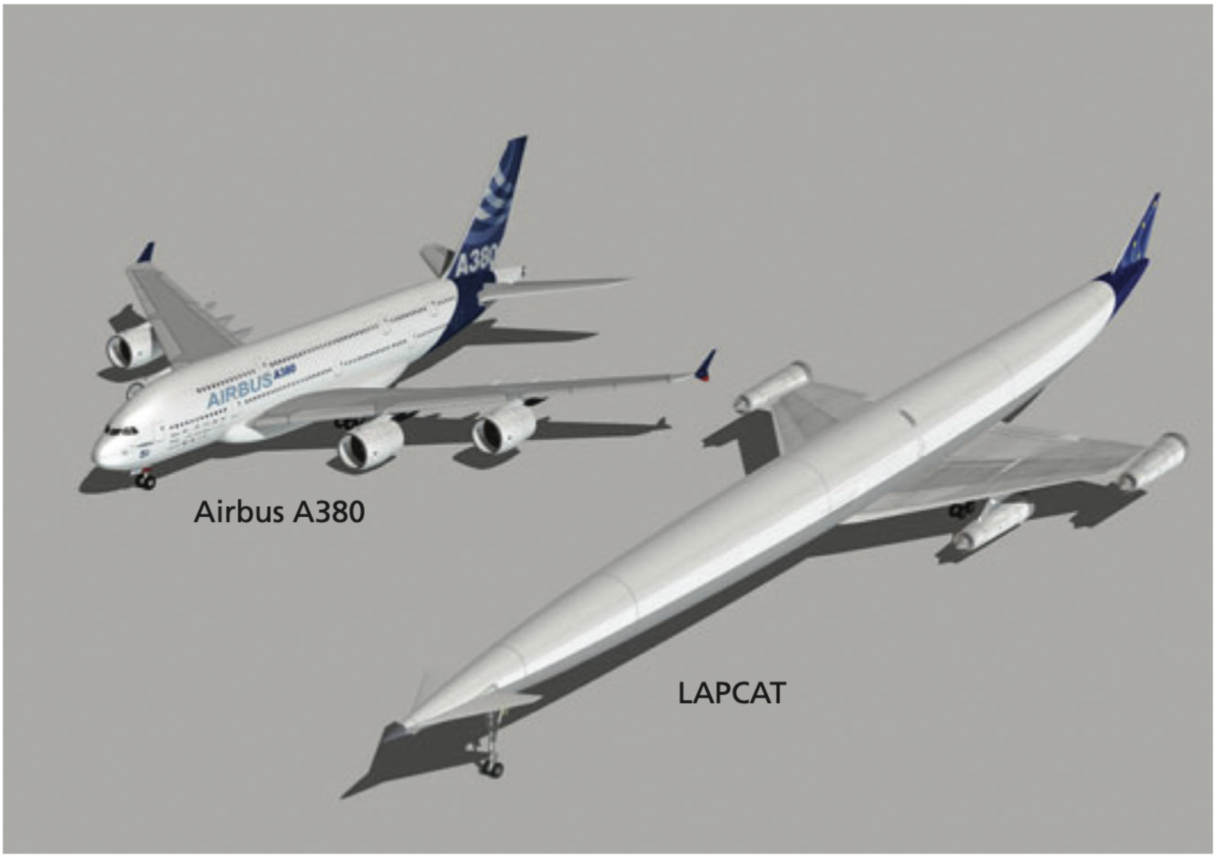

Figure 2.13: European LAPCAT II
Source: Promotional photo from Reaction Engines.

2.5 Flight Conditions and Typical Aerodynamics Shapes.

In the following section, general features of an hypersonic weapon will be described, pointing out the typical mission designs, trajectories and typical shapes. A very general discussion will be presented, not distinguishing between hypersonic vehicle, Common Aero Vehicle and hypersonic glider since the differences among these are very inconspicuous under the following areas of analysis.

2.5.1 Mission Design

Assuming an HGV as a striking weapon, the mission profile can be generally divided into several stages[49]:

- Launch phase - the vector lifts the weapon to a suborbital altitude (about 100 Kms);
- Reentry phase - the vehicle arrives at the upper atmosphere;
- Pull-up manoeuvre - the HGV has to reach the speed and altitude of glide phase;
- Glide manoeuvre - the glider flies along trajectory;
- Speed depletion - the glider achieves the required terminal speed for striking
- Impact - the weapon strikes the target.

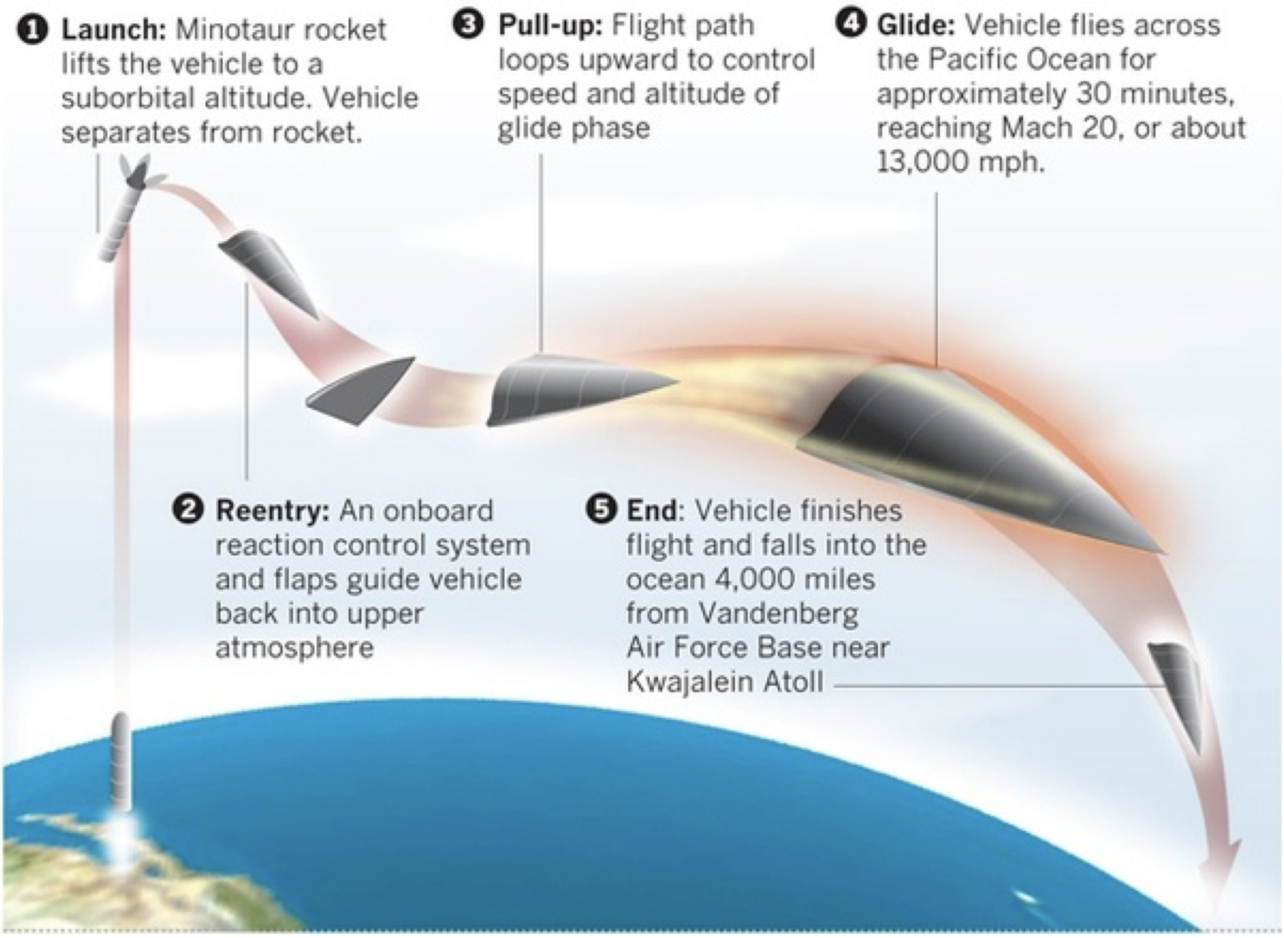

Figure 2.14: HTV-2 Mission design Source: Defense Advanced Research Project Agency, Times reporting

However, if the considered glider has one-sided angle of attack control, during the speed depletion, the vehicle will have to rotate and fly upside-down in order to generate negative lift and strike the target. These is considered to be an additional phase where lift rotation is achieved[50].

2.5.2 Trajectories

The Hypersonic vehicles are characterized by an high maneuverability since they must respect all the constraints in their complex trajectories. The trajectories indeed, are generally subjected to significant multiple constraints[51]:

1. Terminal Conditions - the terminal position coordinates, the specified final altitude, and speed;
2. Control Boundary - Bank angle σ and angle of attack α are two control variables and in order to ensure the glider stability, their magnitudes use to be respectively between ±50 deg and 5 deg and 25 deg (normally the angle of attack is around 10-15 deg since the L/D ratio is maximum[52]);
3. Heating rate - the heating rate at a specified point on the glider surface (normally stagnation point is chosen) must be limited along the whole trajectory;
$$\dot{Q} \leq \dot{Q}_{max} \tag{2.1}$$
4. Aerodynamic Load - the aerodynamic load in the body-normal direction, must be limited and must not overcome the maximum allowed load;
$$|L\cos\alpha + D\sin\alpha| \leq n_{t_{max}} \tag{2.2}$$
5. Dynamic pressure - if actuators are present (in CAV-H, movable surfaces are used to achieve better aerodynamic performance), the dynamic pressure is limited so that the hinge moment is controlled in a reasonable range;
$$\frac{1}{2}\rho V^2 \leq q_{max} \tag{2.3}$$
6. Waypoints - Particular points which are specified as intermediate coordinates to fly over to satisfy particular mission requirements;
7. No-fly zones - Specified region with a boundary that the vehicle may contact but must not violate and they are specified for geopolitical restrictions or threat avoidance.
8. Quasi-Equilibrium Glide Condition - in a major portion of a lifting entry trajectory, the flight-path angle is small and varies relatively slow.

Subjected to these constraints, more than a trajectory is available. It is necessary to optimize the trajectory and find the values of the control variables such that the objective function is minimum (or maximum, depending on the mission). The problem of trajectories optimization is difficult or impossible to solve analytically for the most of the cases therefore numerical techniques are required to determine an approximation to the continuous solution. Methods are generally divided into indirect and direct methods. The formers involve approximating the solution to the continuous necessary conditions and they have high accuracy and assure the solution satisfies the optimal conditions. However, in indirect methods, the optimal conditions must be derived analytically and this derivation is not-trivial. Direct methods instead overcome some of these problems by transforming the continuous optimal control problem into a nonlinear programming problem which can be solved by algorithms. Some of these methods can have an high computational cost and law efficiency, such as the the direct shooting used to parameterize the control variables and implement numerical integration. Gauss pseudospectral method (GPM) instead is generally used to avoid these problems by parameterizing control and sates variables and approximating the differential equations at collocation points with piecewise or global polynomials. An evolution of this method is the multi-phase Gauss pseudospectral method (MGPM) which provides for dividing the trajectories into multiple phases by three kinds of specific points: waypoints, quasi-contact points (for no-fly zones), and turn points. Then, the state and control variables are discretized at nodes in each phase, separately and the continuity conditions on the time, state, and control are introduced to keep the trajectory smooth enough between each pair of phases. By combining all the phases, the objective function is determined to guarantee a global optimal trajectory [7].

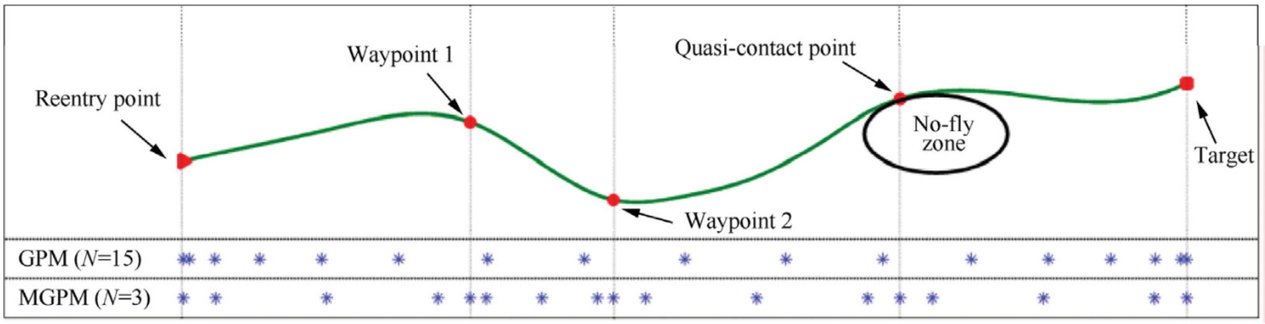

Figure 2.15: Example of segmented trajectories and distribution of nodes for a GPM and MGPM[7].

2.5.3 Aerodynamics Shapes

The HCVs work in an hypersonic speed range, thus the generation of strong shock waves is inevitable. Focusing the attention on gliders, the presence of a shock wave is exploited to reach high L/D ratios at high Mach number thanks to the particular Waverider shape. This particular aerodynamic form allows to create an attached shock-wave on the vehicle surface. The flow past through the shock wave is enclosed between the low surface of the aircraft and the shock surface. In this region underneath the lower surface of the vehicle, the flow increases its pressure, while the upper surface region is affected by a much smaller pressure since it is not conditioned by the shock. This pressure difference between the upper and lower surface generates lift [53–56]. In the following figure there is a typical Waverider shape: a strong oblique shock wave is attached to the leading edge and it is responsible for the high pressure region. Different design methods are available to obtain the particular Waverider shape. Commonly, this kind of geometry is obtained thanks to an inverse designed method.

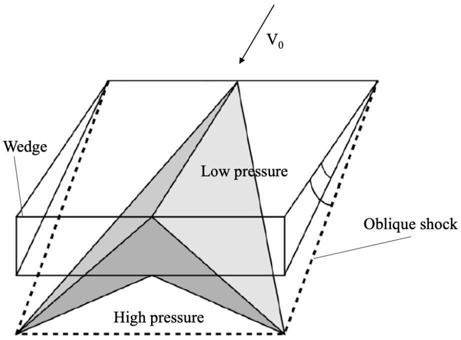

Figure 2.16: Caret Waverider with a oblique shock[8]

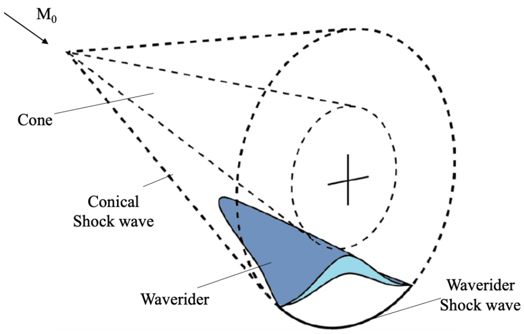

Figure 2.17: Cone generated Waverider

In fact, in order to ensure a proper functioning, Waveriders need to have an attached shock wave on the leading edge: thus aircraft geometry is, in a way, already set. Therefore, the problem of designing a Waverider is translated to the selection of the most appropriate shape/body which generates the most appropriate shock wave. The Caret Waveriders are generated from shock wave produced by a wedge, even though this is not the only possibility[57]. An important work by Rasmussen [58] proves how it is possible to create an aerodynamic surface which exploits a shock wave derived by a flow passing a cone. This alternative provides an higher L/D ratio and higher volumetric efficiency than the Caret's.

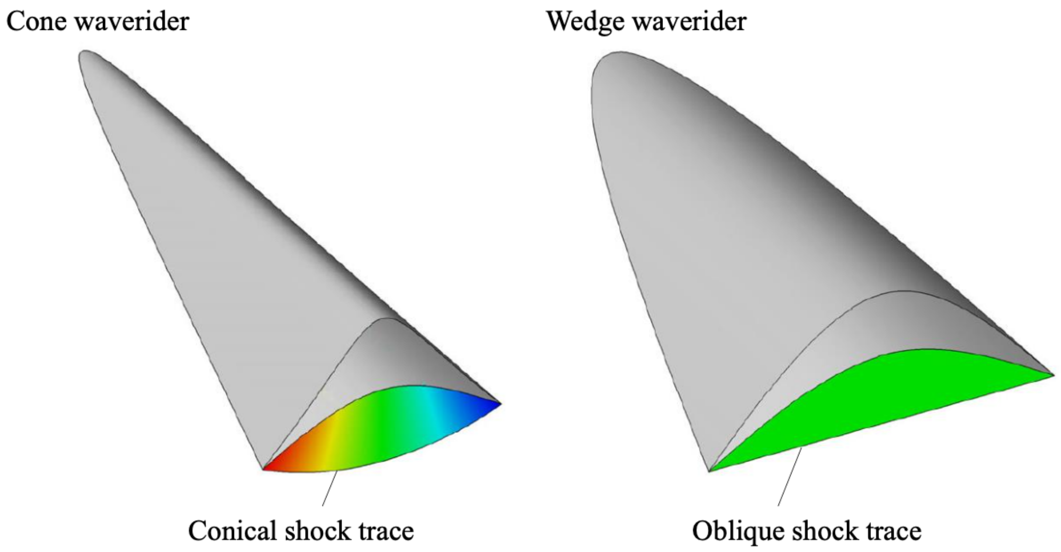

Figure 2.18: Different shock traces [8]

As it is shown in the Figure 2.18, there is a circular line for the conic shock wave, and a straight line for the wedge generated shock. There are many other studies which supply changes in these methods in order to improve some features in design, but they keep on using an inverse design approach. However, this approach means that, in order to design geometry, it's necessary to solve an aerodynamic problem and there will be different equations depending on the considered flow. Many design method have been developed, including wedge-derived method, cone-derived method, wedge-cone method and osculating cone method, but it is difficult to treat the compromise between high aerodynamic performances and volumetric efficiency[59]. Generally, the idea is to obtain a well-balanced design among the conflicted objectives. In particular, the L/D ratio is fundamental since most of flight performances such as range and maneuverability are related to it. On the other side, the aircraft internal subsystems require proper space for their positioning, so volumetric efficiency is essential. These are the main two parameters in conflicts in design of hypersonic vehicles, so they are chosen as optimal objectives in the design optimization process. The optimization is essentially based on parametric methods, divided into CAD or analytic ones. The most popular CAD-based methods are the ones which use B-spline, widely used for hypersonic aerodynamic optimization. Others are the mesh points methods used by Kinney to represents configurations of hypersonic vehicles. However, the CAD-based methods present a very high cost under a computational point of view since they exploit control points as design variables. Analytic methods instead, are widely used in order to overcome these problems through the use of class and shape transformation functions (CST). This analytic method is based on the simple use of functions for geometric representations and form functions to control the key parameters of the design (leading edge radius, specified thickness)[60–63]. The Figures below show how different can be the shapes depending on the applied method.

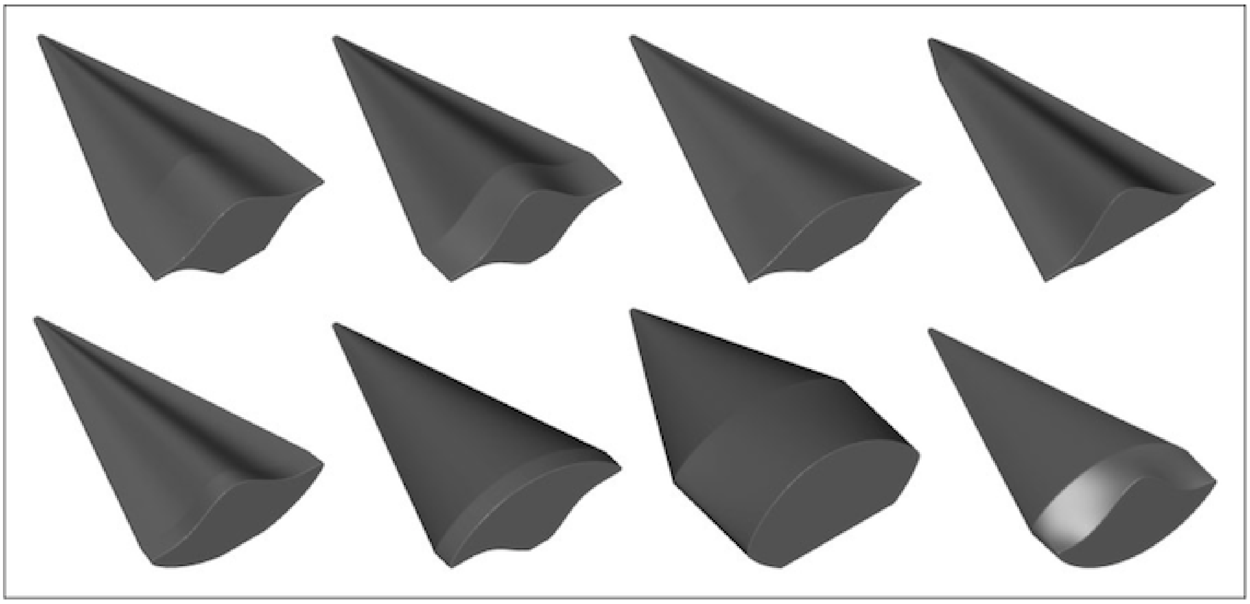

Figure 2.19: Examples of lifting body obtained with parametrization method[9].

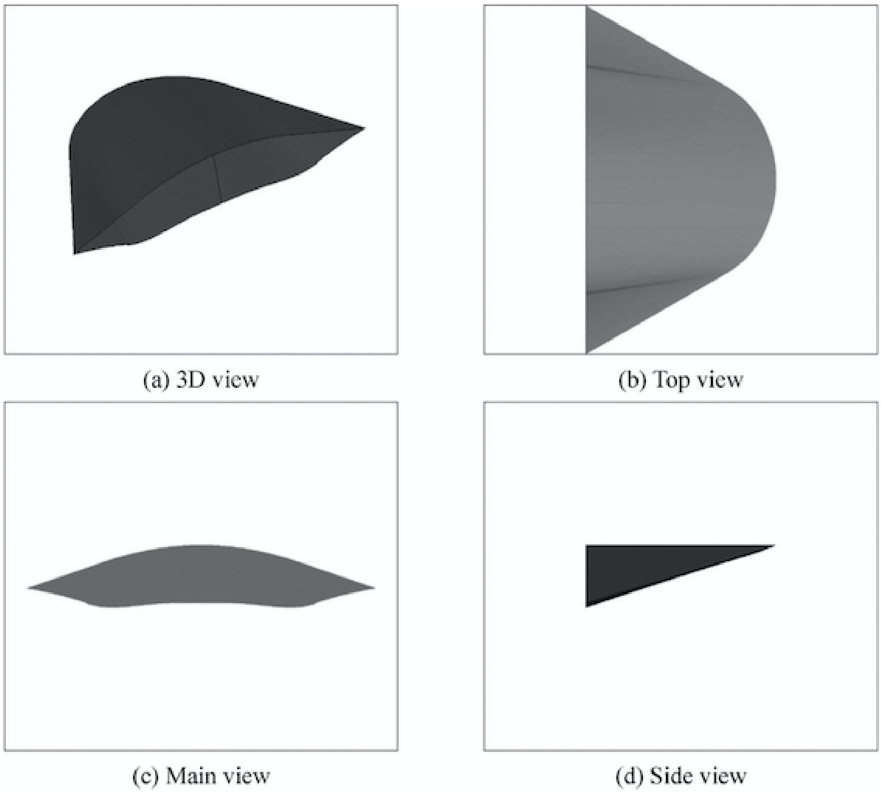

(a) 3D view

(b) Top view

(c) Main view

(d) Side view

Figure 2.20: Examples of lifting body obtained with Delta-winged design methodology [10]

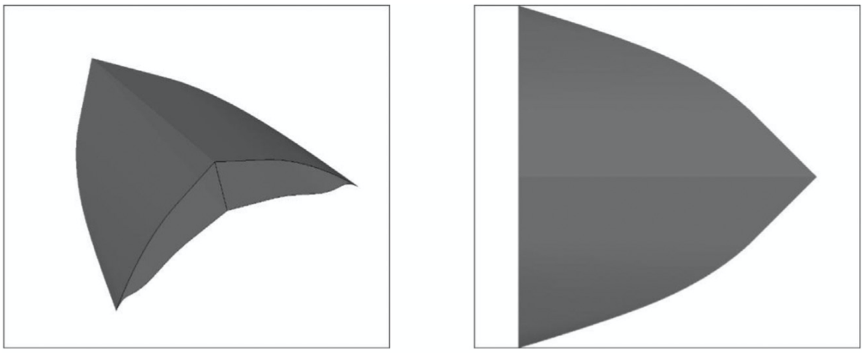

(a) 3D view (b) Top view

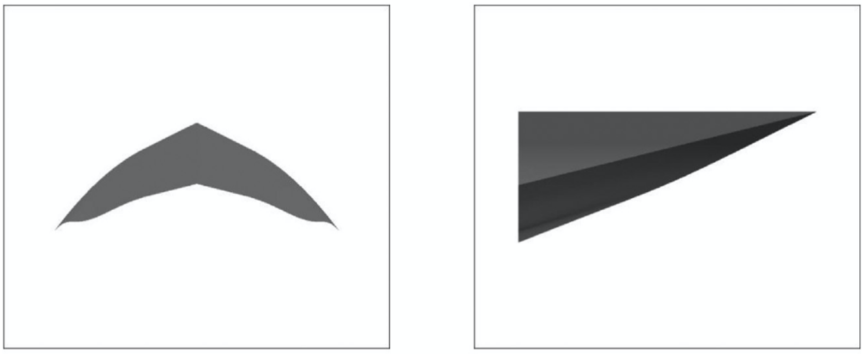

(c) Main view (d) Side view

Figure 2.21: Examples of lifting body obtained with cuspidal design methodology [10]

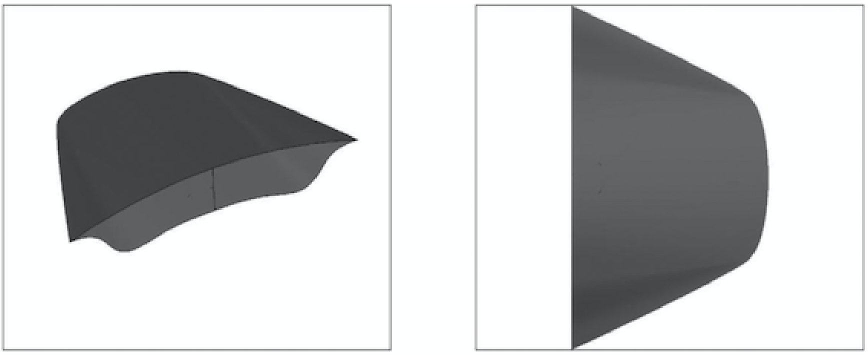

(a) 3D view (b) Top view

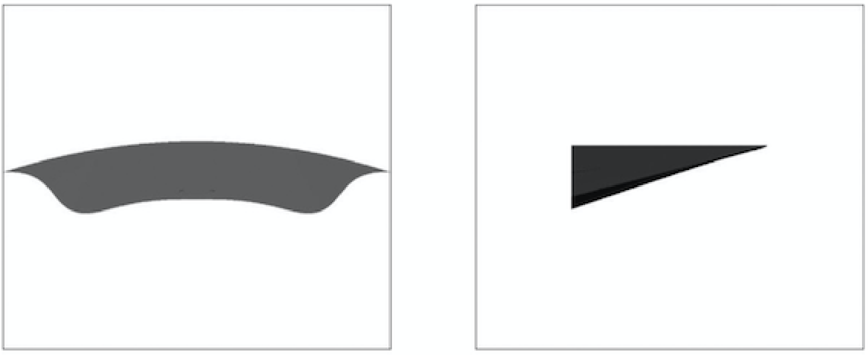

(c) Main view (d) Side view

Figure 2.22: Examples of lifting body obtained with oscultaing cone method [10]

However, even though the shapes showed above are quite different each other, they all will present an attached shock wave on the leading edge which will ensure the generation of lift.

Chapter 3

Phisycal problem and models

3.1 Intro

In the present chapter, the emphasis will be projected on the importance of hypersonic viscous and chemically reacting flows, focusing on more purely fluid-dynamic and thermochemical aspects. The portions of the flight trajectories of HCMs experience combined conditions of high Mach number and low Reynolds number, conditions that accentuate the effect of hypersonic viscous flow and aerodynamic heating. The air flow will be analyzed as a gas mixture where some of its components will be specified neglecting others. Moreover, basic aspects of viscous and thermo-chemically reacting flows will be discussed, including the full governing equations (the Navier-Stokes equations) and how they are affected by hypersonic and high temperature conditions. The analysis begins from equations for a chemically non reacting fluid and how these will change if high temperature conditions are taken into account. Finally the Volume Finite Method is introduced as solver of the equations.

3.2 Governing equations for chemically non-Reacting viscous flow

The governing equations of mass, momentum and energy properly described the physics of an air flow surrounding a body. The basic assumptions for the current study are the following[64]:

- Continuum fluid:

$$Kn = \frac{l}{L} << 1 \tag{3.1}$$

  where l is the molecular mean free path and L is a representative physical length scale;

- Mass and energy are separately conserved (no relativistic motions);

- Body forces are neglected;

- Stokes's hypothesis (it relates the first, μ, and the second λ, coefficient of viscosity)

$$\lambda = -\frac{2}{3}\mu \tag{3.2}$$

- Newtonian fluid (this implies a linear relation between the stress tensor and the symmetric part of the deformation tensor):

$$\tau_{ij} = \delta_{ij}\lambda\nabla\cdot\mathbf{v} + \mu(\frac{\partial u_i}{\partial x_j} + \frac{\partial u_j}{\partial x_i}) \tag{3.3}$$

- Radiation is neglected (in chapter 4 it will be shown how radiative effects will be included in the equations);

- Fourier fluid (this implies the conduction part of the heat flux vector linearly related to the temperature gradient)

$$\dot{\mathbf{q}} = -k\nabla T \tag{3.4}$$

  k is the thermal conductivity coefficient.

The hypothesis of continuum implies that the derivative of all the dependent variables exists in some reasonable sense. Local properties, such as density and velocity, are defined as averages over elements large compared with the microscopic structure of the fluid but small enough in comparison with the scale of the macroscopic phenomena, to permit the use of differential calculus to describe them. The set of differential Governing equations of mass, momentum and energy are:

$$\frac{\partial \rho}{\partial t} + \nabla \cdot \rho \mathbf{v} = 0 \tag{3.5}$$

$$\frac{\partial \rho \mathbf{v}}{\partial t} + \nabla \cdot \rho \mathbf{v}\mathbf{v} = -\nabla p + \nabla \cdot \boldsymbol{\tau} \tag{3.6}$$

$$\frac{\partial \rho E}{\partial t} + \nabla \cdot \rho \mathbf{v} E = -\nabla \cdot p\mathbf{q} + \nabla \cdot \boldsymbol{\tau} \cdot \mathbf{v} + \nabla \cdot \dot{\mathbf{q}} \tag{3.7}$$

The above equations are written for an unsteady, compressible, viscous, three dimensional, chemically non-reacting flow and there is no general analytic solution to the complete set of equations.

3.3 High Temperature Effects

This section lay the physical fundamentals to understand the high temperature flows. The first step is to understand how effectively, chemical reactions take place. Many chemical reactions do not occur spontaneously but they require an initial input of energy (activation energy) to get started. During chemical reactions, certain chemical bonds are broken and new ones are formed. However, molecules must be deformed in order to get them into a state that allows the bonds to break and a small energy input is required to achieve this transition state. It is a high-energy, unstable condition where reactant molecules don't last long in this state, but very quickly proceed to the next steps of the chemical reaction by forming new species. The source of the activation energy needed to push reactions forward is typically heat energy from the surroundings. This source speeds up the motion of molecules, increasing the frequency and force with which they collide. Hence, heating up a system will cause chemical reactants to react more frequently. Increasing the pressure on a system has the same effect. Once reactants have absorbed enough heat energy from their surroundings to reach the transition state, the reaction will proceed[65].

3.3.1 Heat of reaction

During chemical reactions, some heat can be absorbed or released depending on the kind of process. After a reaction has occurred, the system might be at a temperature T_2 different from the initial one T_1. The heat of reaction is the amount of heat that must be added or subtracted from or to the system after the reaction in order to bring it to the initial temperature T_1. It is defined at a given reference temperature T_{ref} (T_1). Depending on the values assumed by heat of reaction, two types of reaction can be distinguished[66]:

- endothermic reaction: $\Delta H_{Tref} > 0$;
- exothermic reaction: $\Delta H_{Tref} < 0$;

Therefore temperature field will be strongly affected by chemical processes since reactions involve heat exchanges.

3.3.2 Gas mixture

In the present analysis, a mixture of reacting gases will be considered and each constituents satisfy the perfect gas law. The following equations are equivalent[67]:

$$p_i = N_i RT \tag{3.8}$$

$$p_i = c_i Rt \tag{3.9}$$

$$p_i = \rho_i \frac{R}{M_i} T \tag{3.10}$$

$$p_i = \rho q_i RT \tag{3.11}$$

with:

- p_i partial pressure of the i-th species;
- N_i number of moles of the i-th species;
- c_i concentration of the i-th species (number of moles per unit volume);
- ρ_i partial density of the i-th species;
- q_i is the mole-mass ratio of the i-th species;

Other possible variables used to define the composition of the gas mixture are the mass concentration y_i and the mole concentration x_i defined as:

$$y_i = \frac{M_i}{M} \tag{3.12}$$

$$x_i = \frac{N_i}{N} \tag{3.13}$$

3.3.3 Five and Eleven Species Mixture

The reacting flow field downstream the bow shock provides for the presence of new species to be considered. Mixture will be considered as composed by eleven different species:

$$N_2, O_2, NO, N, O, N^+, N_2^+, O^+, O_2^+, NO^+, e^-$$

Ar, H_2O and CO_2 have been neglected since they are present in air at room temperature in small fractions. The generic reaction can be expressed as:

$$\sum_i^{N_{spe}} v_i A_i = 0 \tag{3.14}$$

Where N_{spe} is the total number of chemical species in the reaction, v_i is the stoichiometric mole number associated with species A_i. It is assumed positive for the products and negative for the reactants. However, since the following thread is independent of number of constituents of mixture, for sake of simplicity the treatment to obtain species concentration in this chapter will proceed considering an air mixture of five species. The considered species are:

$$N_2, O_2, NO, N, O \tag{3.15}$$

Five dissociation reactions for molecular oxygen will be considered:

$$O_2 + O \rightarrow 2O + O \tag{3.16}$$

$$O_2 + N \rightarrow 2O + N \tag{3.17}$$

$$O_2 + NO \rightarrow 2O + NO \tag{3.18}$$

$$O_2 + O_2 \rightarrow 2O + O_2 \tag{3.19}$$

$$O_2 + N_2 \rightarrow 2O + N_2 \tag{3.20}$$

Five dissociation reactions for molecular nitrogen:

$$N_2 + O \rightarrow 2N + O \tag{3.21}$$

$$N_2 + N \rightarrow 2N + N \tag{3.22}$$

$$N_2 + NO \rightarrow 2N + NO \tag{3.23}$$

$$N_2 + O_2 \rightarrow 2N + O_2 \tag{3.24}$$

$$N_2 + N_2 \rightarrow 2N + N_2 \tag{3.25}$$

Five dissociation reactions for nitric oxyde:

$$NO + O \rightarrow N + O + O \tag{3.26}$$

$$NO + N \rightarrow N + O + N \tag{3.27}$$

$$NO + NO \rightarrow N + O + NO \tag{3.28}$$

$$NO + N_2 \rightarrow N + O + N_2 \tag{3.29}$$

$$NO + O_2 \rightarrow N + O + O_2 \tag{3.30}$$

Two exchange reactions:

$$NO + O \rightarrow N + O_2 \tag{3.31}$$

$$N_2 + O \rightarrow N + NO \tag{3.32}$$

The possible reactions which may occur in the eleven species mixture are shown in the Chemkin file[16] in the appendix A.

3.3.4 Frozen, non-equilibrium and equilibrium flows

Generally, a flow field can be in an equilibrium, non-equilibrium or even a frozen state. Defining τ_f as the characteristic time for a fluid element to traverse the flow field of interest (typically $\tau_f = \frac{L}{V}$) and τ_c as the characteristic time for the chemical composition or internal energy to reach the equilibrium, the different flow states can be distinguished as follow:

- if $\tau_f >> \tau_c$ local equilibrium conditions may be assumed;
- if $\tau_f << \tau_c$ frozen flow conditions may be assumed;
- if $\tau_f \sim \tau_c$ non equilibrium conditions may be assumed;

In the following sections, the effects and meaning of these states will be detailed.

Frozen flow

This condition implies no chemical change take place and since reactions do not occur, the composition of the mixture remains unaffected by high temperatures. However, the specific heats of the various molecules do change with temperature therefore mixture properties do not remain unchanged.

Chemical equilibrium flow

The chemical equilibrium condition occurs when species concentrations are time-independent and the mixture composition is a function of temperature and pressure only. This state happens when number of collision per unit time is high enough such that the time required by a reaction to occur is infinitesimal.

$$y_i = y_i(T, p) \tag{3.33}$$

It has already been underlined that the concentration of the species will set out the thermodynamic properties of the fluid. For a single species, specific enthalpy and specific energy are functions of temperature only, so each species behaves as thermally perfect gas. For a gas mixture, the thermodynamics properties depend on the concentrations of the single species[64].

$$h = (T, y_1, y_2 ... y_{Ns}) \tag{3.34}$$

$$e = (T, y_1, y_2 ... y_{Ns}) \tag{3.35}$$

$$c_p = (T, y_1, y_2 ... y_{Ns}) \tag{3.36}$$

$$c_v = (T, y_1, y_2 ... y_{Ns}) \tag{3.37}$$

In particular, the enthalpy of a gas mixture is:

$$h = \sum_{i=1}^{N_s} q_i (H - \epsilon_o)_i + \sum_{i=1}^{N_s} q_i (\Delta H_f)_i^0 = \sum_{i=1}^{N_s} y_i (h - e_0)_i + \sum_{i=1}^{N_s} y_i (\Delta h_f)_i^0 \tag{3.38}$$

Where the first term is the sensible enthalpy of the mixture, meanwhile the second one is the heat of formation at absolute zero of the mixture[68]. The sensible enthalpy of the single species can be evaluated using statistical mechanics[69] and it is function of temperature only. The heat of formation is the heat of reaction for a reaction representing the formation of a chemical species from its elements. However, the physics problem required to couple additional relations to Navier-Stokes equations, in order to evaluate properly the flow field thermo-fluid dynamic state. Firsts relations are obtained by defining, for any chemical reaction, a pressure equilibrium constant:

$$K_p = \prod_{i=1}^{N_s} p_i^{v_i} \tag{3.39}$$

K_p is function of temperature and it can be obtained experimentally or by statistical thermo-dyanmics calculus[70]. Considering the previous 17 reactions:

$$\frac{p_O^2}{p_{O_2}} = K_{p_1} = K_{p_2} = K_{p_3} = K_{p_4} = K_{p_5} = K_{p_{O_2,diss}} \tag{3.40}$$

$$\frac{p_N^2}{p_{N_2}} = K_{p_6} = K_{p_7} = K_{p_8} = K_{p_9} = K_{p_{10}} = K_{p_{N_2,diss}} \tag{3.41}$$

$$\frac{p_N^2 p_O}{p_{NO}} = K_{p_{11}} = K_{p_{12}} = K_{p_{13}} = K_{p_{14}} = K_{p_{15}} = K_{p_{NO,diss}} \tag{3.42}$$

$$\frac{p_N p_{O_2}}{p_{NO} p_O} = K_{p_{16}} \tag{3.43}$$

$$\frac{p_N p_{NO}}{p_{N_2} p_O} = K_{p_{17}} \tag{3.44}$$

Since the equations (3.43) and (3.44) can be obtained directly from the (3.40),(3.41) and (3.42) only three of them are independent. Two more relations are needed to obtain mixture composition and they can be found considering that, in absence of nuclear reactions, the mass of the chemical elements in the mixture remains constant. Pointing out the table below: The elements of this table are defined as $a_{ie,is}$

El\Sp	O	N	NO	O_2	N_2
O	1	0	1	2	0
N	O	1	1	O	2

where "ie" is the element index and "is" is the species index. The number of particles of each element per total mass must be conserved, therefore the following expression is achieved:

$$\frac{N_{ie}}{m} = const = \sum_{is} \frac{a_{ie,is} N_{is} N_A}{m} = N_a \sum_{is} a_{ie,is} q_{is} \tag{3.45}$$

where N_{ie} is the number of particles of the i-th element N_{is} is the number of mole of the i-th species and N_A is the Avogadro's number. Basically, the equilibrium composition of a gas mixture is defined by $N_{spe} - N_{ele}$ equilibrium constant equations and N_{ele} mass conservation equations. Furthermore, a concentrations equilibrium constant is interchangeable with the pressure one. Since the composition of the mixture is constant, the net chemical reaction rate $\frac{d[X_i]}{dt}$, defined below[11], is equal to zero.

$$\frac{d[X_i]}{dt} = (\frac{d[X_i]}{dt})_f + (\frac{d[X_i]}{dt})_b = 0 \tag{3.46}$$

where:

$$(\frac{d[X_i]}{dt})_f = (v_i^{''} - v_i^{'}) k_f \prod_{j=1}^{N_s} [X_j]^{v_j^{'}} \tag{3.47}$$

$$(\frac{d[X_i]}{dt})_b = -(v_i^{''} - v_i^{'}) k_b \prod_{j=1}^{N_s} [X_j]^{v_j^{''}} \tag{3.48}$$

Therefore the net reaction rate is expressed as:

$$\frac{d[X_i]}{dt} = (v_i^{''} - v_i^{'}) \{ \; k_f \prod_{j=1}^{N_s} [X_j]^{v_j^{'}} - k_b \prod_{j=1}^{N_s} [X_j]^{v_j^{''}} \} \tag{3.49}$$

K_f and K_b are respectively the forward and backward reaction rate and they are functions of temperature only. The equation 2.49 is also called law of mass action. The chemical equilibrium state expects that:

$$k_f \prod_{j=1}^{N_s} [X_j]_{eq}^{v_j^{'}} = k_b \prod_{j=1}^{N_s} [X_j]_{eq}^{v_j^{''}} \tag{3.50}$$

the equilibrium constant based on concentration is:

$$K_c = \frac{k_f}{k_b} = \frac{\prod_{j=1}^{N_s} [X_j]_{eq}^{v_j^{''}}}{\prod_{j=1}^{N_s} [X_j]_{eq}^{v_j^{'}}} \tag{3.51}$$

Exploiting the relationship between molar concentration and partial pressure it follows:

$$p_i = [X_i] RT \tag{3.52}$$

$$K_c = \frac{k_f}{k_b} = \frac{\prod_{j=1}^{N_s} [p_j]_{eq}^{v_j^{''}}}{\prod_{j=1}^{N_s} [p_j]_{eq}^{v_j^{'}}} (\frac{1}{RT})^{\sum_{j=1}^{N_s} (v_j^{''} - v_j^{'})} = K_p (\frac{1}{RT})^{\sum_{j=1}^{N_s} (v_j^{''} - v_j^{'})} \tag{3.53}$$

The chemical rates constants can be measured experimentally but in some cases they can be calculated. In this analysis the *Arrhenius* equation will be used:

$$k_f = c_1 T^{\alpha} e^{\frac{-\epsilon_a}{kT}} \tag{3.54}$$

where c_1, α are constants which comes from experimental data meanwhile ϵ_a is the energy activation.

3.3.5 Chemical Non equilibrium

Before reaching the equilibrium conditions, the gas mixture will always experience for a certain amount of time, a relaxation phase, where its composition will be changing with time. During this phase, the gas is in chemical non-equilibrium condition. Therefore, the state of chemical non-equilibrium expects concentrations to be functions of time, pressure and temperature.

$$y_i = y_i(t, T, p) \tag{3.55}$$

By reference to the previous sections, each reaction contributes to the rate of change of $[X_i]$:

$$\frac{d[X_i]}{dt} = \sum_{r=1}^{N_r} (\frac{d[X_i]}{dt})_r = \sum_{r=1}^{N_r} (v_i^{''} - v_i^{'})_r \{ \ k_{fr} \prod_{j=1}^{N_s} [X_j]^{v_{jr}^{'}} - k_{br} \prod_{j=1}^{N_s} [X_j]^{v_{jr}^{''}} \} \tag{3.56}$$

Where N_r is the number of reactions where the i-th species effectively reacts.

3.3.6 Internal energy and vibrational non-equilibrium

It has been frequently pointed out how thermodynamics properties are effected by species concentration. However, energetic processes caused by high temperature effects may occur and modify the internal energy of molecules[11]. According to the Born-Oppenheimer approximation the internal energy is composed of four part:

$$\varepsilon^{'} = \varepsilon_{trans}^{'} + \varepsilon_{rot}^{'} + \varepsilon_{vibr}^{'} + \varepsilon_{el}^{'} \tag{3.57}$$

where:

- $\varepsilon_{trans}^{'}$ is the translational energy owned by every atom or molecule. For pluri-atomic molecules, this is the translational kinetic energy of the center of mass and it involves three degrees of freedom;

- $\varepsilon_{rot}^{'}$ is the rotational energy and it exists for molecules only. It involves two degrees of freedom for linear polyatomic and diatomic molecules, three for non linear polyatomic molecules;

- $\varepsilon_{vibr}^{'}$ is the vibrational energy owned by molecules only. If an harmonic oscillator model with an infinite number of vibrational energy levels is considered, the vibrational energy of a molecular species per unit mass in equilibrium conditions is:

  $$e_i^v = \frac{\frac{hv_i}{k_B}}{e^{\frac{hv_i}{k_B T}} - 1} R_i \tag{3.58}$$

  where k_B and h are respectively the Bolztmann and Planck constant. v_i is the fundamental vibration frequency of the molecule, it refers to the i-th vibrational energy level and it is different for different molecules. As it can be observed in the previous formula, the vibrational energy is function of temperature only;

- $\varepsilon_{el}^{'}$ is the electronic energy. Sources of electronic energy are the translational motion electrons along their orbit and the potential energy related to the electrons location in the electromagnetic field created by the nucleus and the electrons. Since the motion is very complex, it is usually not convenient to describe in terms of degrees of freedom;

Quantum mechanics states that each of four contributions to the internal energy is quantized, that is a molecule owns only discrete values of energy.

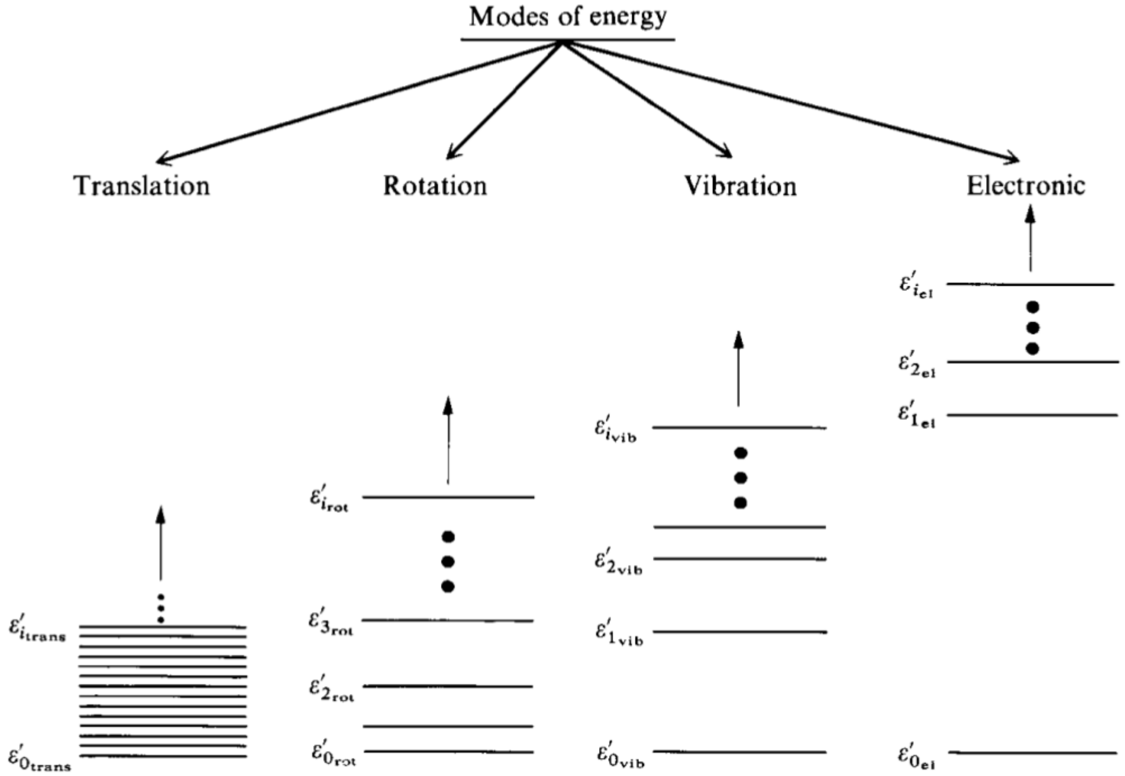

Figure 3.1: Schematic of energy levels for the different molecular energy modes[11].

High temperatures increase number of collision of molecules and can induce reaction but also a switch from a quantized vibrational energy level to another one (the most probable is the transition of a single quantum energy level to the adjacent level). The energy gained or lost by the molecules may result in a decrease or increase in the translational kinetic energy of the molecules. As it will be shown, this is not the only possibility of energy exchange.

$$X_i(v) + X_i(v^{'}) \leftrightarrow X_i(v-1) + X_i(v^{'}) + kinetic\,energy \tag{3.59}$$

X_i is the generic species, v and v' are respectevely the v-th and v'-th vibrational energy level. Since the vibrational energy level are no more the same, a non-equilibrium condition occurs and the vibrational rate equation is given by:

$$\left(\frac{de_i^v}{dt}\right)_{V-T} = \frac{e_i^{v,eq} - e_i^v}{t_i} \tag{3.60}$$

The time rate is of change of e_i^v is proportional to the difference between the equilibrium state of vibrational energy and the new state of non-equilibrium, and it is inversely proportional to the vibrational relaxation time t_i^{V-T}. The non-equilibrium state will result in a transitional phase where the vibrational energy changes till, a new equilibrium state is reached (for large times). The previous expression takes into account only reactions where vibrational energy is converted to translational energy. However this is not the only possible mechanism of vibrational energy exchange, indeed, a vibrational-vibrational energy exchange may also occur (V-V transfer). For example if an anharmonic oscillator model is used, there is an effective energy excess:

$$X_i(v) + X_i(v^{'}) \leftrightarrow X_i(v-1) + X_i(v^{'}+1) + kinetic\,energy \tag{3.61}$$

as well as for different reacting species, since different species involve different spacing among energy levels:

$$X_i(v) + X_j(v^{'}) \leftrightarrow X_i(v-1) + X_j(v^{'}+1) + kinetic\,energy \tag{3.62}$$

Meanwhile, in case of harmonic oscillator model, since the spacing between two adjacent vibrational energy levels is constant, there is no energy excess.

$$X_i(v) + X_i(v^{'}) \leftrightarrow X_i(v-1) + X_i(v^{'}+1) \tag{3.63}$$

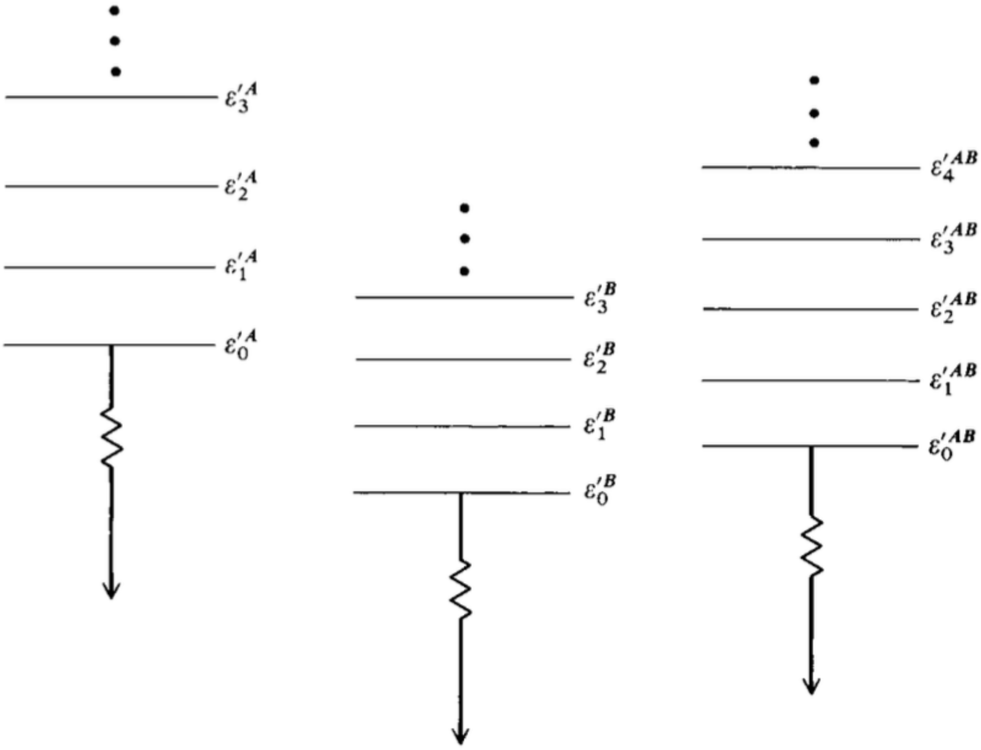

Figure 3.2: schematic of energy levels for three different chemical species[11].

The contribution of V-V transfer is added to that of the V-T transfer in the global vibrational rate equation of the species i:

$$\left(\frac{de_i^v}{dt}\right) = \frac{e_i^{v,eq} - e_i^v}{dt} + \left(\frac{de_i^v}{dt}\right)_{V-V} \tag{3.64}$$

3.3.7 Chemical effects in air

In conclusion, high temperature are needed to observe important thermo-chemical effects in a mixture. The figure 5.23 illustrates the temperature ranges of dissociation and ionization in air at a pressure of $1\,atm$. When temperature reaches values of 800 K the vibrational energy of a molecule become significant. After 2000 K the dissociation of O_2 starts, while N_2 starts at 4000 K. Above 9000 K, ionization of N_2 and O_2 occurs and plasma is present, consisting mainly of O, O^+, N, N^+ and electrons. Between 4000 and 6000 K a small amount of NO is formed, some of which is ionized giving origin to NO^+ and free electron. However, the small number density of electrons generated by the ionization of NO may be sufficient to cause communications blackout[11]. The figure 3.4 denotes the region where these effects are important, showing the flight path of a lifting entry body in function of speed, altitude and the lift parameter $\frac{m}{C_L S}$.

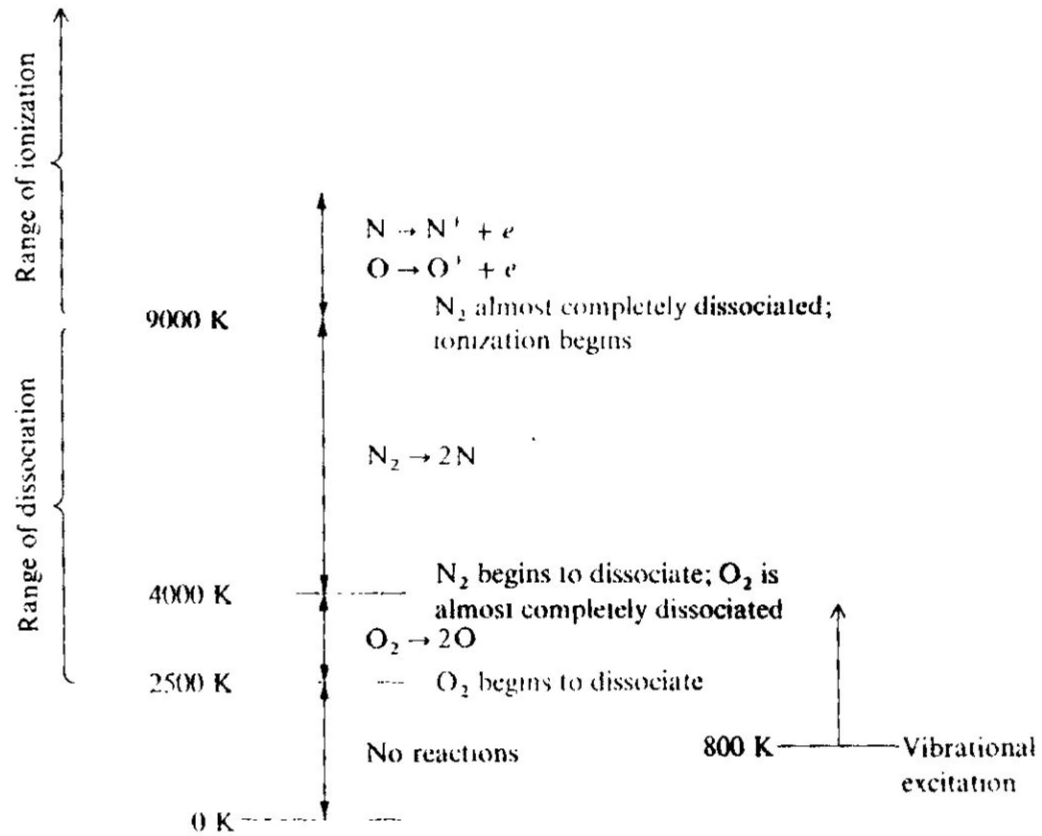

Figure 3.3: Range of vibrational excitation, dissociation and ioniziation for air at 1 atm pressure [11]

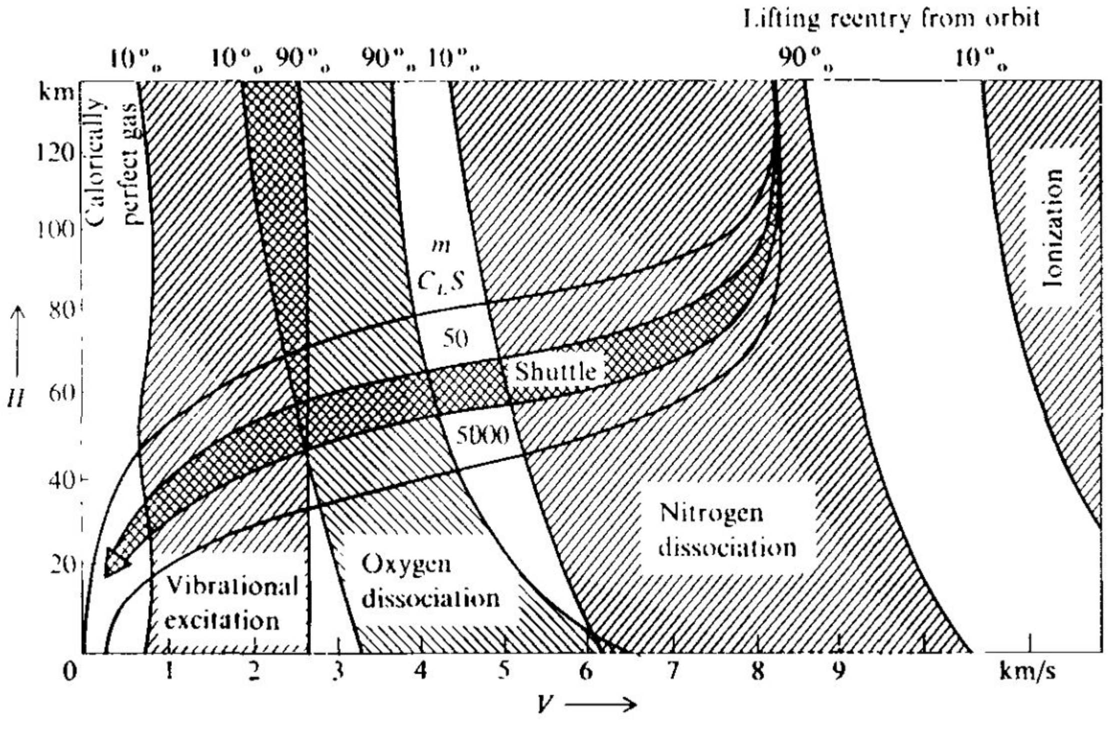

Figure 3.4: Velocity-altitude map with regions of vibrational excitation, dissociation and ionization[12]

The entry flight path crosses major sections of the velocity-altitude map meeting important chemical reactions and vibrational excitation phenomena. This is just an example of how significant high temperature effects are for body travelling at hypersonic speed.

3.4 Governing equations for chemically reacting viscous flow

In the present section, all the consequences of chemical and vibrational non-equilibrium will be highlighted for a chemically reacting viscous flow[11].

3.4.1 Momentum and continuity equations

The momentum and continuity equations are apparently, purely mechanical in nature and they seem to be not affected by chemical reactions. However, this is not totally true for momentum equations. Precisely, in a chemical reacting gas, the mechanism of diffusive transport of momentum involves a gas viscosity coefficient which depends upon the presence of the each single species in the mixture. A possibility to derive the viscosity coefficient is the approximate Wilke's rule:

$$\mu = \sum_i \frac{X_i \mu_i}{\sum_j X_i \Phi_{ij}} \tag{3.65}$$

with

$$\Phi_{ij} = \frac{1}{\sqrt{8}} \left(1 + \frac{M_i}{M_j}\right)^{-\frac{1}{2}} \left[1 + \left(\frac{\mu_i}{\mu_j}\right)^{\frac{1}{2}} \left(\frac{M_j}{M_i}\right)^{\frac{1}{4}}\right]^2 \tag{3.66}$$

However, as it will be described later, a different model will be applied in the commercial software to compute the viscosity coefficient.

3.4.2 Additional mass equations

For chemically reacting viscous flows, under the assumption of chemical non-equilibrium, balance equations for mass of single species must be taken in account. Considering a control volume fixed in space, the mass of the i-th species can change in time if:

- there is a net flux of the i-th species through the surface surrounding the control volume;
- there is a production or extinction of the i-th species inside the control volume due to the chemical reactions;
- there is a net diffusive flux of the i-th species through the surface surrounding the control volume;

Therefore the additional equations in integral form are:

$$\frac{\partial}{\partial t} \int_V \rho_i dV + \int_S \mathbf{J_{mi}} \cdot \mathbf{n} dS + \int_S \rho_i \mathbf{v} \cdot \mathbf{n} dS = \int_V \Omega_i^{ch} dV \tag{3.67}$$

Ω_i^{ch} is the local rate of change of rho_i due to chemical reactions and it is linked to the rate of change of concentration, since:

$$[X_i]\, M_i = \rho_i \tag{3.68}$$

and

$$\Omega_i^{ch} = \frac{d\rho_i}{dt} = M_i \frac{d\,[X_i]}{dt} = M_i \sum_{r=1}^{N_r} \left(\frac{d[X_i]}{dt}\right)_r = \sum_{r=1}^{N_r} (v_i^{''} - v_i^{'})_r \{\, k_{fr} \prod_{j=1}^{N_s} [X_j]^{v_{jr}^{'}} - k_{br} \prod_{j=1}^{N_s} [X_j]^{v_{jr}^{''}} \} \tag{3.69}$$

$\mathbf{J_{mi}}$ are the species-mass diffusive fluxes and they are related to the corresponding diffusion velocities w_i

$$\mathbf{J}_{mi} = \rho_i \mathbf{w_i} \tag{3.70}$$

Since the total mass cannot diffuse:

$$\sum_{i=1}^{Ns} \mathbf{J}_{mi} = \sum_{i=1}^{Ns} \rho_i \mathbf{w_i} = 0 \tag{3.71}$$

This implies that only N_s-1 balance equations are independent and can be added to the set, while the N_s-th mass species is obtained by differencing. Furthermore, the species-mass diffusive fluxes can be expressed as combination of temperature, pressure, and concentration gradients:

$$\mathbf{J}_{mi} = -\rho D_i \nabla y_i + \frac{1}{T} D_i^T \nabla T + \frac{1}{p} D_i^p \nabla p \tag{3.72}$$

D_i is the multi-component diffusion coefficient and it is related to the binary diffusion coefficients D_{ij}. The former expresses the capacity of the i-th species for diffusing in the mixture, while the latter is index of the capacity for diffusion of the i-th species in the j-th one.

$$D_i = \frac{1 - X_i}{\sum_j \frac{X_j}{D_{ij}}} \tag{3.73}$$

It is assumed that the effects of pressure diffusion mechanisms are not very strong, hence they are neglected. The governing equation for the i-th species in conservative differential form is:

$$\frac{\partial \rho_i}{\partial t} + \nabla \cdot (\rho_i \mathbf{v}) + \nabla \cdot \mathbf{J_{mi}} = \Omega_i^{ch} \tag{3.74}$$

3.4.3 Additional energy equations

If the flow is in a vibrational non-equilibrium state, it is necessary to add equations to consider this effect. In particular, defining e_i^v as the vibrational energy of the i-th species per unit mass of the i-th species, an additional equation can be derived:

$$\frac{De_i^v}{Dt} = \frac{\partial e_i^v}{\partial t} + \mathbf{v} \cdot \nabla e_i^v = \frac{e_i^{v,eq} - e_i^v}{\tau_i^{V-T}} \tag{3.75}$$

The equation has been obtained by following an element of fixed mass along its trajectory. To obtain a conservative form is sufficient multiply the previous equation for ρ_i and to add the continuity equation multiplied for e_i^v:

$$\rho \frac{De_i^v}{Dt} + e_i^v \left[\frac{\partial \rho}{\partial t} + \nabla \cdot (\rho \mathbf{v}) \right] = \frac{\partial \rho e_i^v}{\partial t} + \nabla \cdot (\rho e_i^v \mathbf{v}) = \rho \frac{e_i^{v,eq} - e_i^v}{\tau_i^{V-T}} \tag{3.76}$$

In this case the conservative variable is ρe_i^v. This choice is due to the numerical problem which may derived by using $\rho_i e_i^v$ when the i-th species is completely or almost completely dissociated. Precisely, when this variable is chosen, to obtain the internal vibrational energy e_i^v it is necessary to divide the conservative variable $\rho_i e_i^v$ by ρ_i and such a ratio is a 0/0 form.

3.4.4 Energy transport governing equation

For a chemically reacting gas, there is an energy transport due to diffusion and not only convection and conduction. The i-th species transports with itself enthalpy of the i-th species so that the diffusive flux of energy is:

$$(\mathbf{q_D})_i = -h_i \rho D_{im} \nabla y_i \tag{3.77}$$

Since there are several species in the mixture, the net flux of energy due to the diffusion is the sum of all the species contributions:

$$\mathbf{q_D} = -\sum_{i=1}^{N_s} h_i \rho D_{im} \nabla y_i \tag{3.78}$$

Therefore the final form of the energy equation is:

$$\frac{\partial E}{\partial t} + \nabla \cdot [(E+p)\mathbf{v}] - \nabla \cdot (\boldsymbol{\tau} \cdot \mathbf{v}) - \nabla \cdot \left(k \nabla T + \sum_{i=1}^{N_s} h_i \rho D_{im} \nabla y_i \right) = 0 \tag{3.79}$$

3.4.5 Final equations

In conclusion, the set of equations which characterized a chemically reacting viscous flow in vibrational and chemical non-equilibrum are:

$$\begin{cases} \frac{\partial \rho}{\partial t} + \nabla \cdot \rho \mathbf{v} = 0 \\ \frac{\partial \rho \mathbf{v}}{\partial t} + \nabla \cdot \rho \mathbf{v}\mathbf{v} = -\nabla p + \nabla \cdot \boldsymbol{\tau} \\ \frac{\partial E}{\partial t} + \nabla \cdot [(E+p)\mathbf{v}] - \nabla \cdot (\boldsymbol{\tau} \cdot \mathbf{v}) - \nabla \cdot \left(k \nabla T + \sum_{i=1}^{N_s} h_i \rho D_{im} \nabla y_i \right) = 0 \\ \frac{\partial \rho_i}{\partial t} + \nabla \cdot (\rho_i \mathbf{v} + \mathbf{J_{mi}}) = \Omega_i^{ch} \\ \frac{\partial \rho e_i^v}{\partial t} + \nabla \cdot (\rho e_i^v \mathbf{v}) = \rho \frac{e_i^{v,eq} - e_i^v}{\tau_i^{V-T}} \end{cases} \tag{3.80}$$

where:

$$E = \rho \left\{ \sum_{i=1}^{N_s} \left[y_i \left(e_i^{tr} + e_i^{rot} + e_i^{vibr} + e_i^{el} + (\Delta h_f)_i^0 \right) \right] \right\} + \rho \frac{1}{2} \left(u^2 + v^2 + w^2 \right) \tag{3.81}$$

$$h = \rho \left\{ \sum_{i=1}^{N_s} \left[y_i \left(e_i^{tr} + e_i^{rot} + e_i^{vibr} + e_i^{el} + R_i T + (\Delta h_f)_i^0 \right) \right] \right\} \tag{3.82}$$

3.5 Numerical Solution: Finite Volume Method

3.5.1 Introduction

Since the problem cannot be solved analytically, a numerical, but sufficiently accurate solution is required. The Finite Volume Method allows to obtain a numerical approximate solution by transforming the set of partial differential equations over differential volumes into discrete algebraic equations over finite volumes (or cells). The algebraic system is then solved to compute the values of the fluid dynamic variable for each of the elements. This method is preferred for several reasons[71]:

- some of the terms in the conservation equation are turned into face fluxes and evaluated at the finite volume faces. Since the flux entering a given volume is identical to that leaving the adjacent volume, the method is strictly conservative;
- the method can be formulated in the physical space on unstructured polygonal meshes. These characteristics have made the FVM quit suitable for the numerical simulation of a variety of applications involving fluid flow and heat and mass transfer.

Nevertheless, the used discretization procedure involves two basic steps. The first step provides for an integration of the partial differential equations into a system of linear algebraic equations and then they are transformed into balance equations over an element. The surface and volume integrals changes into discrete algebric relations over elements by using an integration quadrature of a specified order of accuracy. The result is a set of semi-discretized equations. The second step provides for an approximation of the variables within the element by means of interpolation profiles and supply a relationship among the surface values of the variables to their cell values. In both steps, the applied approximations affect the accuracy and robustness of the numeric results.

3.5.2 Time-dependent technique, Hyperbolic problem

Since the current study is focused on a HCM in en-route condition, a steady state analysis will be carried on. However the difficulty in solving the flow field surrounding the missile resides in the nature of governing equation for this kind of flow. The shock layer of a blunt body is a particular flow where the subsonic and supersonic regions are divided by a sonic line. The assumptions for a steady flow make the governing equations mathematically elliptic for subsonic regions and hyperbolic/parabolic for supersonic ones. Numerical methods suitable for the subsonic flow region are inadequate for the supersonic one (and vice versa) and this make the solution very though to obtain. A different approach is currently used to solve the unsteady equations regardless whether the flow is locally subsonic or supersonic [71]. The "*time − dependent*" approach starts from an arbitrary initial conditions and it calculates the steady flow solution as the asymptotic limit at large times.

3.5.3 Equations

The finite volumes method uses the integral form of the governing equations as a starting point. In this section only the mass, momentum and energy equations are considered, in order to provide an introduction to the Finite Volume Method while the full solution method will be detailed in the following chapter. The set of differential partial equations are:

$$\frac{\partial}{\partial t}\begin{bmatrix}\rho\\ \rho\mathbf{v}\\ \rho E\end{bmatrix}+\nabla\cdot\begin{bmatrix}\rho\mathbf{v}\\ \rho\mathbf{v}\mathbf{v}+p\mathbf{I}-\boldsymbol{\tau}\\ (\rho E+p)\mathbf{v}-\boldsymbol{\tau}\cdot\mathbf{v}-k\nabla T-\sum_{i=1}^{N_s}h_i\rho D_{im}\nabla y_i\end{bmatrix}=\begin{bmatrix}0\\0\\0\end{bmatrix} \tag{3.83}$$

The set of previous equations will be expressed,for the sake of simplicity, with one vectorial equations:

$$\frac{\partial\mathbf{U}}{\partial t}+\nabla\cdot(\mathbf{F}-\mathbf{G})=0 \tag{3.84}$$

where:

$$\mathbf{U}=\begin{bmatrix}\rho\\ \rho\mathbf{v}\\ \rho E\end{bmatrix} \tag{3.85}$$

$$\mathbf{F}=\begin{bmatrix}\rho\mathbf{v}\\ \rho\mathbf{v}\mathbf{v}+p\mathbf{I}\\ (\rho E+p)\mathbf{v}\end{bmatrix} \tag{3.86}$$

$$\mathbf{G}=\begin{bmatrix}0\\ \boldsymbol{\tau}\\ \boldsymbol{\tau}\cdot\mathbf{v}+k\nabla T+\sum_{i=1}^{N_s}h_i\rho D_{im}\nabla y_i\end{bmatrix} \tag{3.87}$$

U is the conservative variables vector, F and G are respectively the inviscid and diffusive fluxes vector. The FVM involves to apply the integral form of the governing equations to each cells/volume. Therefore, for the i-th volume the equation becomes[72]:

$$\frac{\partial}{\partial t}\int_{V_i}\mathbf{U}dV+\int_{S_i}(\mathbf{F}-\mathbf{G})\cdot\mathbf{n}dS=0 \tag{3.88}$$

Considering the mean value of the conservative variables over the i-th volume, and splitting the integral over the cell surface in a sum of integrals over the surfaces which compose the cell contour, it follows:

$$\mathbf{U_i}=\frac{1}{V_i}\int_{V_i}\mathbf{U}dv \tag{3.89}$$

$$\frac{\partial\mathbf{U_i}V_i}{\partial t}+\sum_{surf}\int_{surf}(\mathbf{F}-\mathbf{G})\cdot\mathbf{n}ds=0 \tag{3.90}$$

if the volume is sufficiently small, the surrounding surface can be thought as composed by plane elements. The flux terms can be approximated as uniform over these planes:

$$\frac{\partial\mathbf{U_i}V_i}{\partial t}+\sum_{surf}(\mathbf{F}-\mathbf{G})\cdot\mathbf{n}\Delta S=0 \tag{3.91}$$

This equation (set of equations) (3.91) is the general starting point for applying the finite volume method. Details about the adopted numerical schemes for fluxes and time discretization are specified in the following chapter.

Chapter 4

Computational modeling and procedures

4.1 Intro

The present chapter gives an overview of the computational model and the numerical procedures adopted to obtain a solution of the flow field surrounding an hypersonic cruise missile in en-route condition. The research is carried out in the area close to the nose for different reasons:

- it is the region where thermo-chemical effects take origin due to the critical temperature and pressure downstream the shockwave;
- an investigation on the flow field surrounding the whole missile would have been computationally expensive;
- to avoid low accuracy of the solution since different length scales in the grid entail the spread of numerical errors.

The missile blunt nose defines the flow field properties (shape of the shockwave, heat fluxes) therefore a detailed knowledge of the fluid dynamic variables is essential for an accurate prediction of the heat transfers in that region.

4.2 Software

The analysis will be accomplished using a commercial CFD code. The software used in this work is STAR-CCM+ v14.06.013 , a commercial Computational Fluid Dynamics based simulation software developed by Siemens Digital Industries. It offers the capabilities to model and analyse a wide range of engineering problems involving fluid flow, heat transfer, stress, particulate flow, electromagnetics and related phenomena. The software will be used to model an hypersonic chemically reacting flow.

4.3 Geometry

Geometry strongly affects the hypersonic flow field and in particular the features of the shockwave. The subsonic pocket is the most critical area where the highest temperature and pressure are reached. Hypersonic missiles are cruise and acceleration vehicles, therefore they are slender and they fly at small angles of attack to reduce the wave drag. Consequently, the subsonic pocket in front of the nose is small sized. Furthermore,the nose missile requires to be blunted due to the maximum heat flux at wall at the stagnation region. The flux in that point varies inversely with the square root of the nose radius and to decrease the stagnation point heating, the nose radius must be sufficiently high[73].

$$q_w \propto \frac{1}{\sqrt{R}} \tag{4.1}$$

Since the missile geometry needs to meet these requirements it is characterized by:

- A nose radius of 0.02 m;

- A ramp tangent to the nose which extends over 0.65 m up to a height of 0.16 m.

The dimensions of ramp and nose have been obtained by considering pictures and lengths of Kinzhal, previously shown in Chapter2.

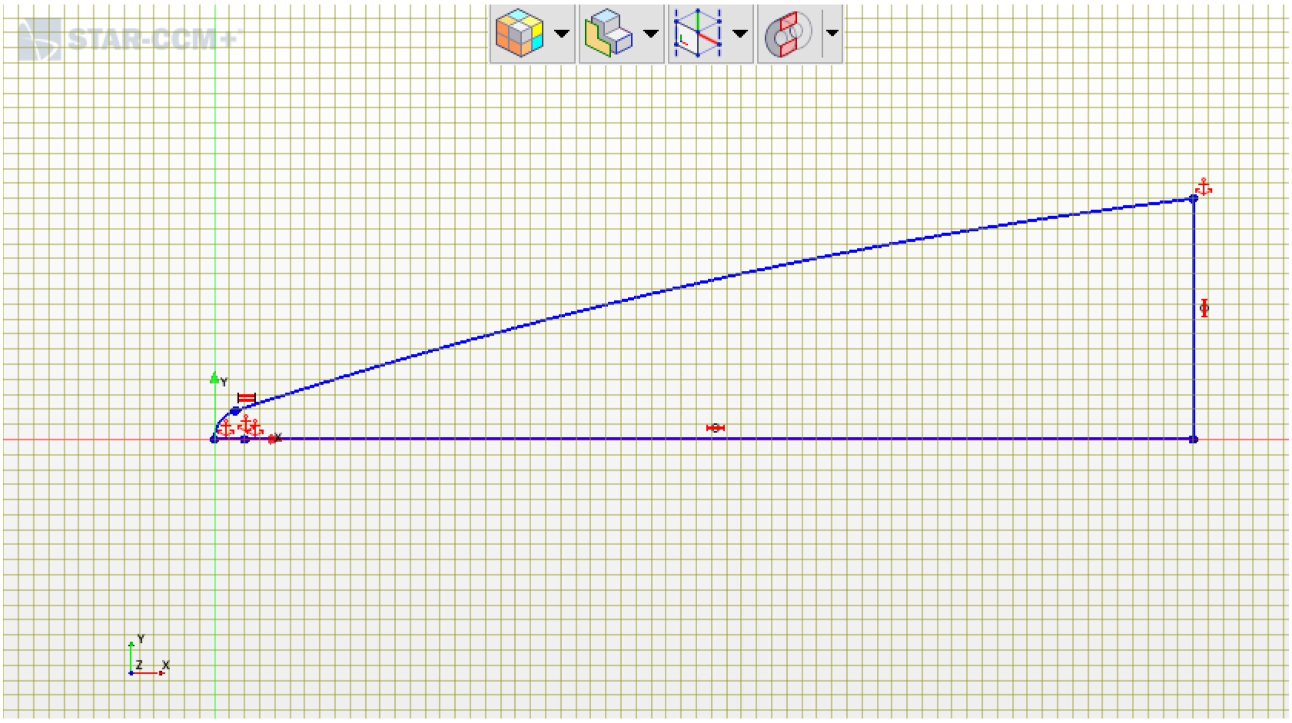

Figure 4.1: Missile profile sketch

Starting from the sketch of the nose profile, a revolving feature has been executed. The result is shown below.

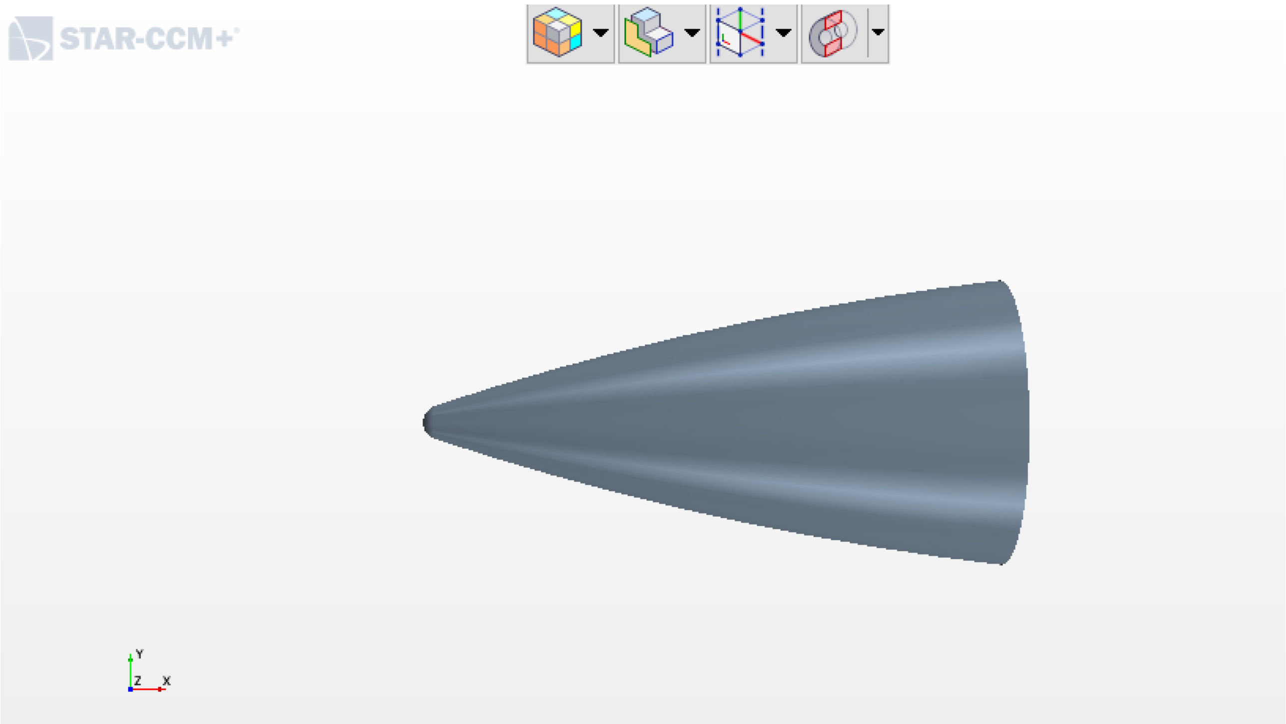

Figure 4.2: Missile frontal part

4.3.1 Computational Domain

Flow field is axisymmetric, therefore the CFD analysis will be carried out in a two-dimensional domain obtained by a section containing the missile axis. Considering that the physical problem involves the presence of a shock wave, an opportune domain must be employed to evaluate properly the fluid dynamics field. Concerning the inflow boundary, two different philosophies can be adopted[74]. The first one is the "shock capturing" where the outer boundary is outside the bow shock wave which comes out automatically from the flow field solution as a rapid change of the flow properties within a certain number of grid points. The other one is the "Shock fitting" approach where the shock is treated explicitly as a discontinuity and it constitutes the outer boundaries. Only the region of the flow field between the shock and body is computed using the discretized equations, while the bow shock defines the moving outer boundary. This technique is very helpful to compute supersonic and hypersonic flows and it produces "clean" results that are unaffected by the numerical problems of capturing the discontinuity in a finite number of points as it occurs using the first approach. However, the shock fitting philosophy is rather complicated to apply owing to the set up to detect and track down discontinuities. In addition, it is potentially not very robust in practical applications therefore it won't be used in this analysis [75] .

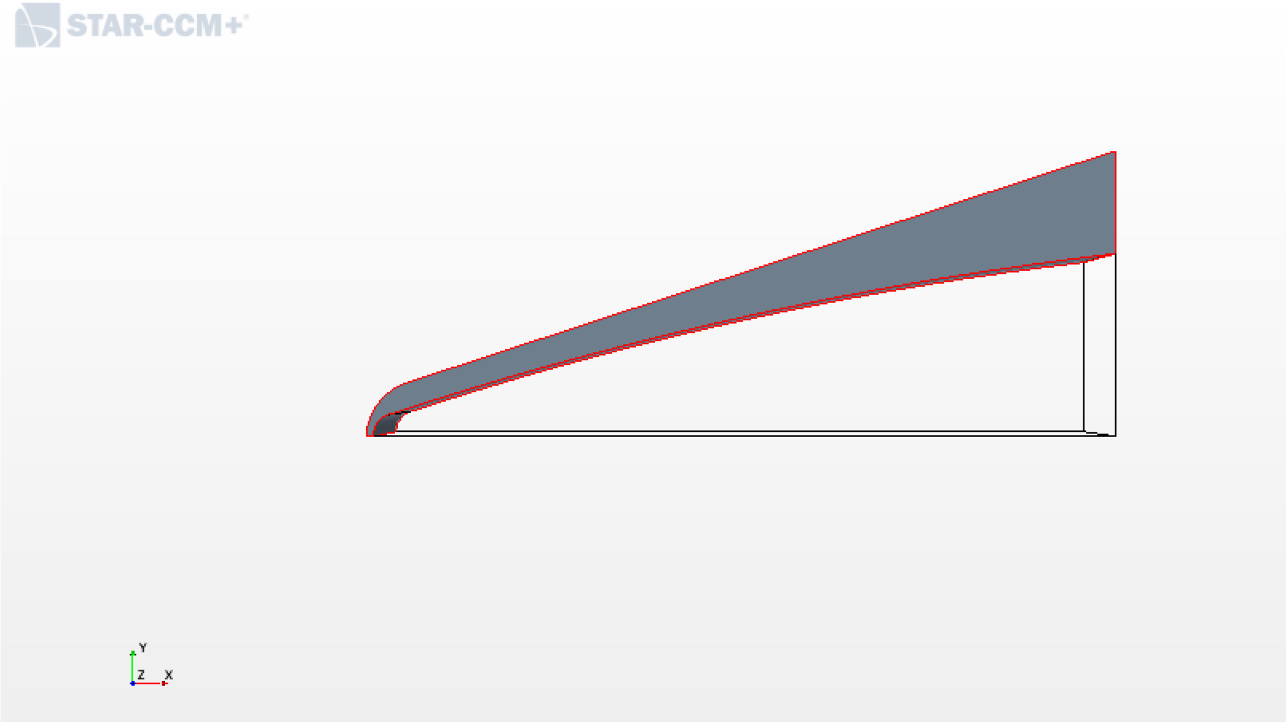

Figure 4.3: Computing Domain

Hence, according the shock capturing approach, the computing domain needs to enclose the shock wave and therefore it has the following geometric characteristics:

- it extends along the axis direction from -0.006 m the nose to 0.65 m over;
- an arc with a radius of 0.0522 m from the point in x=-0.006 on the missile axis up to the point of coordinates $x = 0.0299$ m $y = 0.047$ m;
- a linear ramp tangent to the arc which extends up to the point of coordinates $x = 0.65$ m and $y = 0.25$ m

4.3.2 Mesh

The mesh is a discretized representation of the geometric domain. The domain can include real-world geometry (missile body), its content, and its surrounding environment. In the present case, the mesh includes only the surrounding environment defined by the computing domain described in the previous section. Computational mesh is not totally arbitrary, but it requires to be differently generated depending on the problem. The numeric grid must be sufficiently fine to describe accurately the shock wave shape and to compute the main features of the flow field. In addition, very variable dimensions among cells and skewed shape may introduce numerical errors and reduce the accuracy of the solution[71]. Several simulations has been executed with different meshes to find the most suitable grid which guarantee a proper shock wave shape and reliable results. Among the several possibilities offered by the solver for two-dimensional problems, polygonal and quadrilateral grid with adaptive refinements have been initially used to test the quality of the results. The gradient of Mach number was the parameter chosen to refine the grid. Nevertheless the solution showed a skewed shape of the shock wave and Carbuncle instabilities in the proximity to the axis.

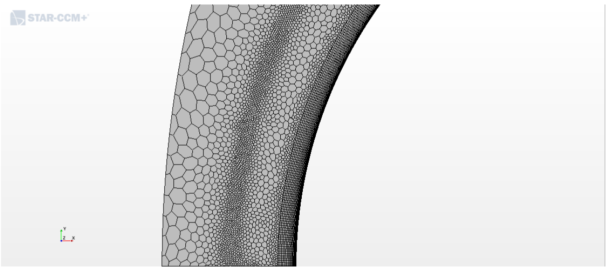

Figure 4.4: Polygonal grid in missile nose area

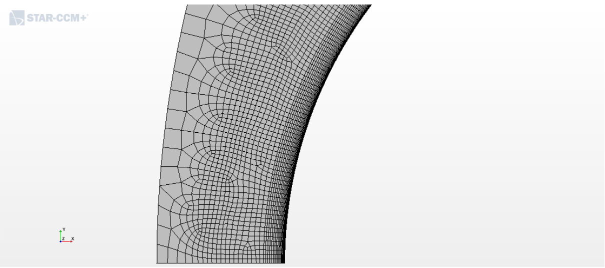

Figure 4.5: quadrilateral grid in missile nose area

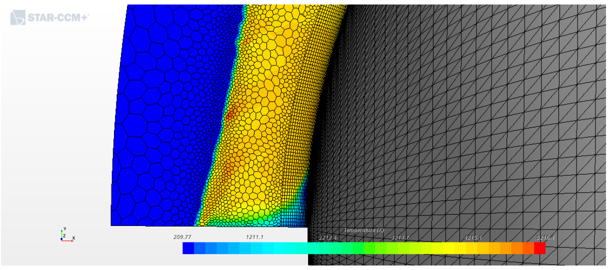

Figure 4.6: Carbuncle instability in temperature field for polygonal grid

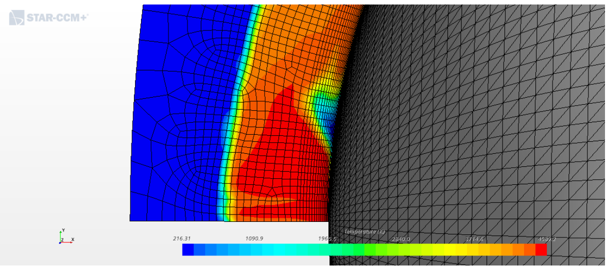

Figure 4.7: Carbuncle instability in temperature field for quadrilateral grid

After several attempts, in order to achieve a detailed and accurate solution and damping instabilities, a directed grid has been employed with the following features:

- one sided geometric spacing distribution along the axial direction with a spacing at start (at wall) equal to 5.0E-5 m;
- 200 divisions along the axial direction;
- one sided geometric spacing distribution along the tangent direction at wall with a spacing at start (axis) of 2.0E-4 m;
- 250 divisions along the tangent direction at wall;

these values of spacing distributions and divisions have been chosen not only to guarantee a proper bow shock shape but to dampen the Carbuncle instability[76].

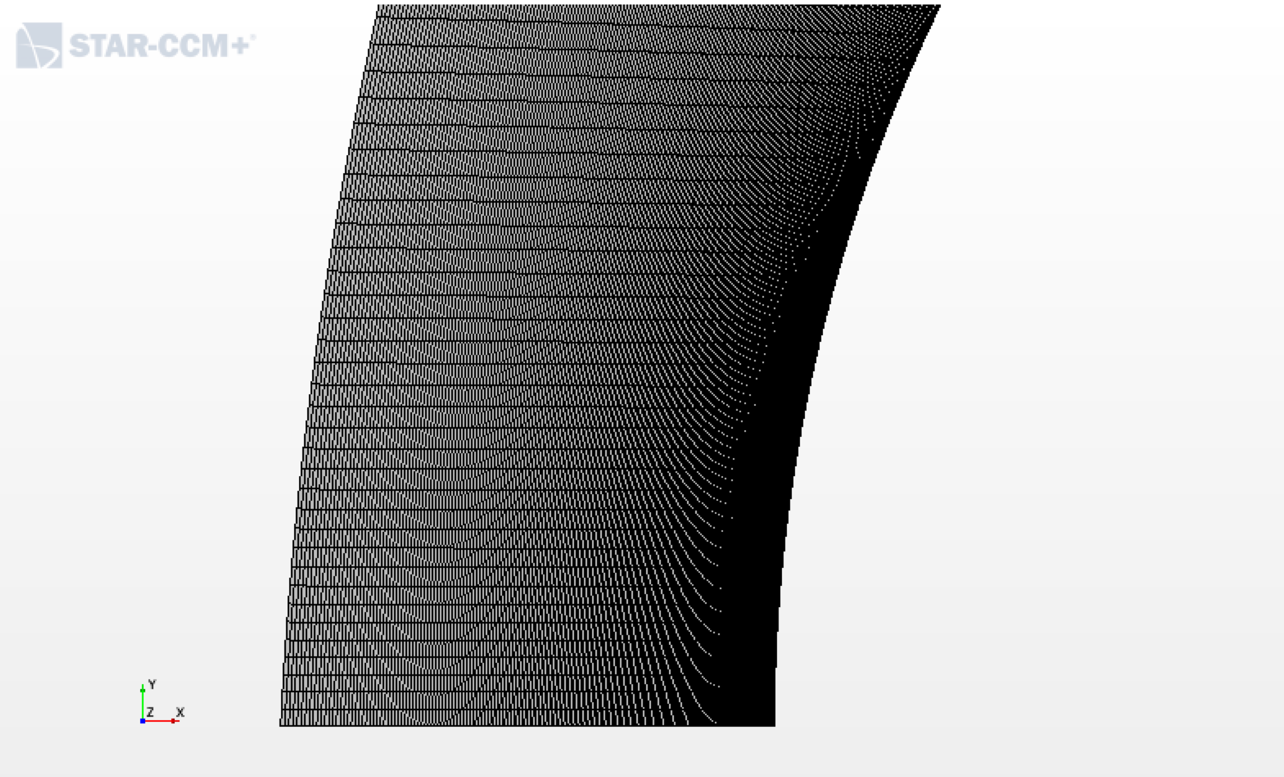

Figure 4.8: Directed grid in missile nose region

4.3.3 Final domain and mesh

However, once the shockwave position had been known after the firsts simulations, a spline has been imported to enclose the shock layer and reduce the computational effort by decreasing the domain size.

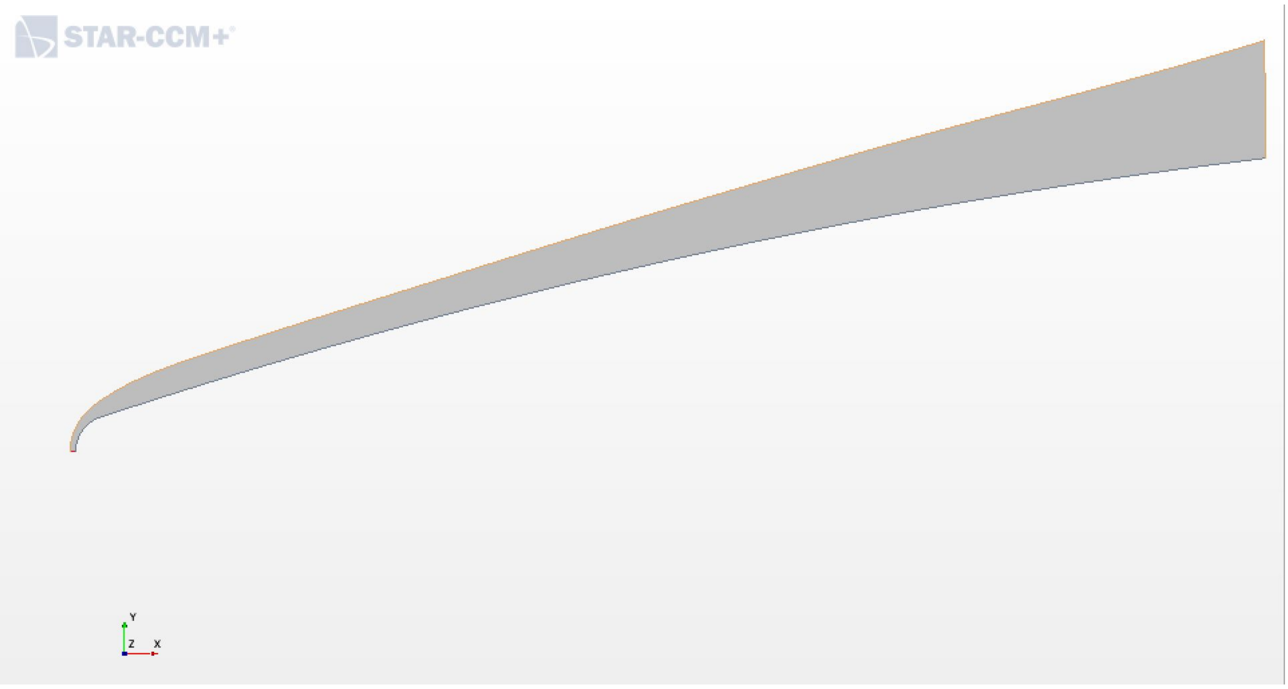

Figure 4.9: Reduced Domain

Furthermore, to achieve a better accuracy of the solution, a new mesh has been created. The mesh has been structured as follow:

- one sided hyperbolic spacing distribution along the axis direction with a spacing at start equal to 5.0E-5 m;
- 100 divisions along the axial direction;
- one sided geometric spacing distribution along the tangent direction at wall with a spacing at start (axis) of 2.0 E-4 m;
- 250 divisions along the tangent direction at wall.

The main difference from the previous mesh is the one sided hyperbolic distribution which has been chosen to avoid negative volume at wall, distorted cells and overflows in the computation of the solution.

4.4 Physics model set up

STAR-CCM+ provides a large variety of physics models to choose from. The following section covers the physics models chosen for the purposes of this investigation:

- Axisymmetric;
- Complex chemistry;
- Coupled Energy;
- Coupled flow;
- Coupled species;
- Gradients;
- Ideal gas;
- Laminar;
- Radiation;
- Participating media Radiation;
- Gray Thermal Radiation;
- Multi-component gas;
- Reacting ;
- Reacting species transport;
- Solution interpolation;
- Steady.

Each of them will be detailed in the following subsections.

4.5 Axisymmetric and steady

Since the analysis is focused on a HCM in en-route phase, with an angle of attack equal to zero, the solver will be set to develop a steady and axisymmetric simulation. Time models in Simcenter STAR-CCM+ provide solvers that control the iteration and/or unsteady time-stepping. The steady model is used for the steady-state calculations and when it is activated, the concept of a physical time-step is meaningless. Space models instead, provide methods for computing and accessing mesh metrics. Example of mesh metrics include cell volume and centroid, face area and centroid, cell and face indexes, and skewness angle. The adopted Axisymmetric model allows to work on two-dimensional axisymmetric meshes. When the model is used, the mesh requires to be oriented such that no part of the mesh can be below the axis of symmetry, and the boundary edge that lies along the axis must be of type *Axis*. For boundary conditions and reporting purposes, the mesh is assumed to be swept through an angle of 1 radian and volumetric or area quantities reported for the Axisymmetric model are assumed to be for a 1-radian sector. Therefore to obtain the value of a quantity for the full revolution, it is necessary to multiply the reported quantities by 2π radians[77].

4.6 Laminar model

Viscous regime models allow to characterize the particular Reynolds dependent flow field. In fluid dynamics, laminar flow is characterized by fluid particles moving along smooth paths in layers, with each layer moving smoothly past the adjacent layers with little or no mixing. It is an high viscosity and low velocities regime, where diffusive phenomena damp out turbulent tendencies. The analysis expects that the nose of the HCM is a stagnation area from which boundary layer develops. This consideration, combined with the conditions downstream the shockwave, make the region of interest in the investigation characterized by a laminar regime.

4.7 Ideal gas and Multi-component gas

Material models are responsible for managing the material, that is, substance or substances being simulated in the domain. The multi-component mixture material model is the one used in the current analysis to describe the eleven species mixture. Multi-component material models are single-phase models for simulating fully miscible mixtures of two or more pure substances in the same phase. In particular, the Multi-Component Gas model manages a Gas Mixture material (that is, a miscible mixture of two or more pure substances in the gaseous phase). In addition, the ideal gas model expects for each mixture component that density is a function of pressure and temperature only:

$$\rho_i = \frac{p_i}{R_i T} \tag{4.2}$$

where

$$R_i = \frac{R}{M_i} \tag{4.3}$$

R is the universal gas constant $[8314{,}4\frac{J}{kmolK}]$ and M_I is the molecular weight of the i-th species. The transport and thermo-dynamical properties of the mixture will be obtained through different approaches and models described in the following subsections. Data required to compute the transport species properties have been taken by the STAR-CMM+ database [77].

4.7.1 Molecular Weight

Molecular weight mixture M_m is computed through the Mixture Method. The mixing law is:

$$M_m = \frac{1}{\sum_i \frac{Y_i}{M_i}} \tag{4.4}$$

M_i and Y_i are respectively the molecular weight and the mass fraction of species i.

4.7.2 Dynamic Viscosity

The dynamic viscosity of the mixture μ is computed starting from the viscosity of the single species by using the Mathur-Saxena average[78]:

$$\mu = \frac{1}{2}\left(\sum_{1}^{N} X_i\mu_i + \left(\sum_{1}^{N}\frac{X_i}{\mu_i}\right)^{-1}\right) \tag{4.5}$$

while the dynamic viscosity of the species i μ_i is calculated by the Chapman-Enskog method:

$$\mu_i = 2.6693x10^{-6}\frac{\sqrt{M_i T}}{\sigma_i^2\Omega(T^*)} \tag{4.6}$$

where:

- $T^* = \frac{kT}{\varepsilon_i}$ is the reduced temperature;
- k is the Boltzmann constant
- ε_i is the potential energy of attraction of component i;
- $\Omega(T^*)$ is collision integral
- μ_i is the viscosity of the i-th species
- M_i is the molecular weight of the i-th species
- T is temperature
- σ_i is the collision diameter of the i-th species

4.7.3 Diffusive effects

The diffusive fluxes have been modeled for each species considering not only species concentration gradients but also temperature gradients (Soret Effect) [79].

$$J_i = \rho D_i \nabla Y_i + \rho\frac{D_{i,t}}{T}\nabla T \tag{4.7}$$

4.7.4 Molecular Diffusivity

Molecular diffusivity of the i-th species is computed through the Kinetic Theory, taking into account mechanisms of multicomponent diffusion. The molecular diffusivity D_i is defined as:

$$D_i = \frac{1 - X_i}{\sum_{j=1,j\neq i}^{N}\frac{X_j}{D_{j,i}}} \tag{4.8}$$

X_i is the mole fraction, $D_{j,i}$ is the binary diffusivity of components i and j. Binary diffusivity coefficients are obtained through a relation based on Chapman-Enskog method [80]:

$$D_{j,i} = \frac{2.66\,x\,10^{-7}T^{\frac{3}{2}}}{pM_{j,i}^{\frac{1}{2}}\sigma_{j,i}^2\Omega(T^*)} \tag{4.9}$$

where:

$$M_{j,i} = \frac{2M_j M_i}{M_j + M_i} \tag{4.10}$$

p is the absolute static pressure. In this case the reduced temperature T^* is defined as:

$$T^* = \frac{kT}{\varepsilon_{j,i}} \tag{4.11}$$

and $\varepsilon_{j,i}$ is the characteristic Lennard-Jones energy for the pair j-i and it is a function of the potential energy ε_j specified for each species. The thermal diffusion coefficient $D_{i,t}$ of the i-th species is computed using the thermal diffusion ratio $K_{t,ij}$ defined as[81]:

$$K_{t,ij} = \frac{15}{2}\frac{(2A_{i,j}+5)(6C_{i,j}-5)}{A_{i,j}(16A_{i,j}-12B_{i,j}+55)}\frac{M_i - M_j}{M_i + M_J}X_iX_j \tag{4.12}$$

with[82]:

$$A_{i,j} = \frac{1}{2}\frac{\Omega_{i,j}^{(2,2)}}{\Omega_{i,j}^{(1,1)}} \tag{4.13}$$

$$B_{i,j} = \frac{1}{3}\frac{5\Omega_{i,j}^{(1,2)} - \Omega_{i,j}^{(1,3)}}{\Omega_{i,j}^{(1,1)}} \tag{4.14}$$

$$C_{i,j} = \frac{1}{3}\frac{\Omega_{i,j}^{(1,2)}}{\Omega_{i,j}^{(1,1)}} \tag{4.15}$$

$\Omega_{i,j}$ is the collision integrals between component i and j. M is the molecular weight. The thermal diffusion coefficient is given as:

$$D_{i,t} = D_i\frac{M_i}{M_m}\sum_{j=1}^{N} K_{t,ij} \tag{4.16}$$

M_m is the molecular weight of the mixture.

4.7.5 Thermal Conductivity

As well as dynamic viscosity, thermal conductivity λ has been computed using the Mathur-Saxena averaging method[83]:

$$\lambda = \frac{1}{2}\left(\sum_1^N X_i\lambda_i + \left(\sum_1^N \frac{X_i}{\lambda_i}\right)^{-1}\right) \tag{4.17}$$

and the thermal conductivity of the species i λ_i is calculated through kinetic theory method:

$$\lambda_i = \frac{\mu_i}{M_I}\left(f_{trans}c_{v,trans} + f_{rot}c_{v,rot} + f_{vib}c_{v,vib}\right) \tag{4.18}$$

where[81, 84]:

$$f_{trans} = \frac{5}{2}\left[1 - \frac{2}{\pi}\frac{c_{v,rot}}{c_{v,trans}}\frac{A}{B}\right] \tag{4.19}$$

$$f_{rot} = \frac{\rho D_i}{\mu_i}\left[1 + \frac{2}{\pi}\frac{A}{B}\right] \tag{4.20}$$

$$f_{vib} = \frac{\rho D_i}{\mu_i} \tag{4.21}$$

$$A = \frac{5}{2} - \frac{\rho D_i}{\mu_i} \tag{4.22}$$

$$B = z_{rot} + \frac{2}{\pi}\left(\frac{5}{3}\frac{C_{v,rot}}{R_u} + \frac{\rho D_i}{\mu_i}\right) \tag{4.23}$$

$$c_{v,trans} = \frac{3}{2}R_u \tag{4.24}$$

$$z_{rot} = z_{rot}(298)\frac{F(298)}{F(T)} \tag{4.25}$$

$$F(T) = 1 + \frac{\pi^{\frac{3}{2}}}{2}\left(\frac{\frac{\varepsilon}{k}}{T}\right)^{\frac{1}{2}} + \left(\frac{\pi^2}{4}+2\right)\frac{\frac{\varepsilon}{k}}{T} + \pi^{\frac{3}{2}}\left(\frac{\frac{\varepsilon}{k}}{T}\right)^{\frac{3}{2}} \tag{4.26}$$

if the molecule is linear:

$$c_{v,rot} = R \tag{4.27}$$

$$c_{v,vib} = c_v - \frac{5}{2}R \tag{4.28}$$

c_v is the specific heat at constant volume of the molecule. The rotational relaxation collision number Z_{rot} is a parameter available at 298K [85].

4.7.6 Specific Heat

Specific heat of the mixture is obtained through a mass-weighted method:

$$c_{pm} = \sum_{i=1}^{N} y_i c_{pi} \tag{4.29}$$

c_{pi} is the specific heat of the i-th species. The specific heat of each component is modeled through thermodynamic polynomial data[15] specified in appendix A. The polynomial adopted properly describes the dependence on temperature of the specific heat and the energetic phenomena which may occur at high temperatures, defined in the previous chapter.

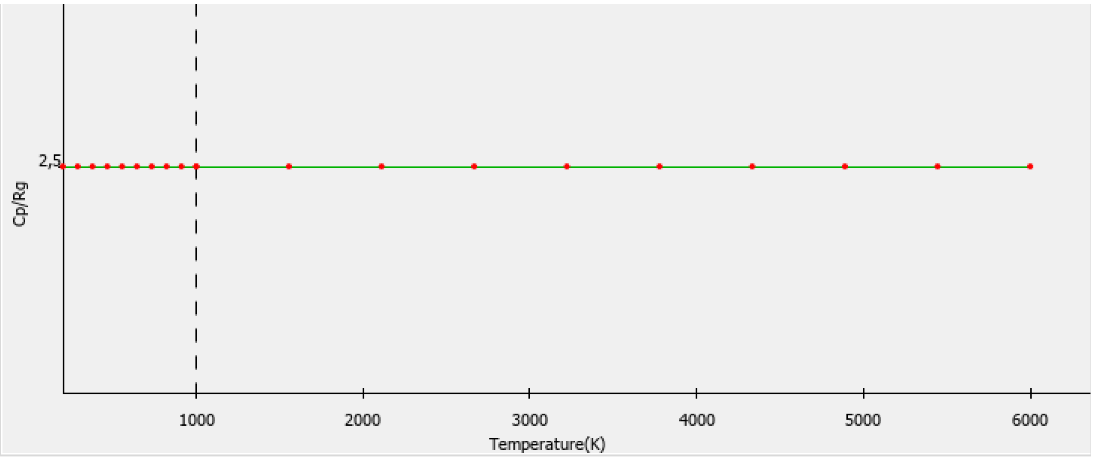

Figure 4.10: Dimensionless Specific Heat of $e-$

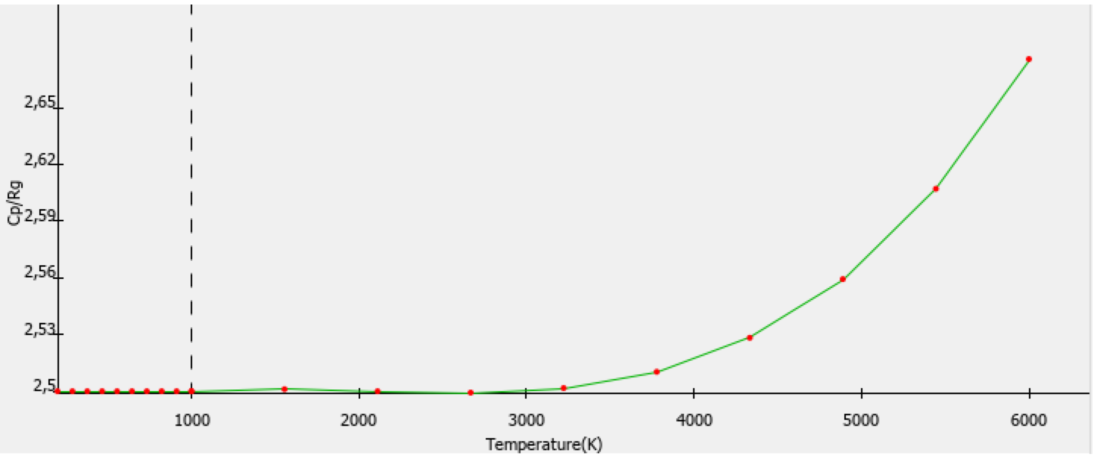

Figure 4.11: Dimensionless Specific Heat of O^+

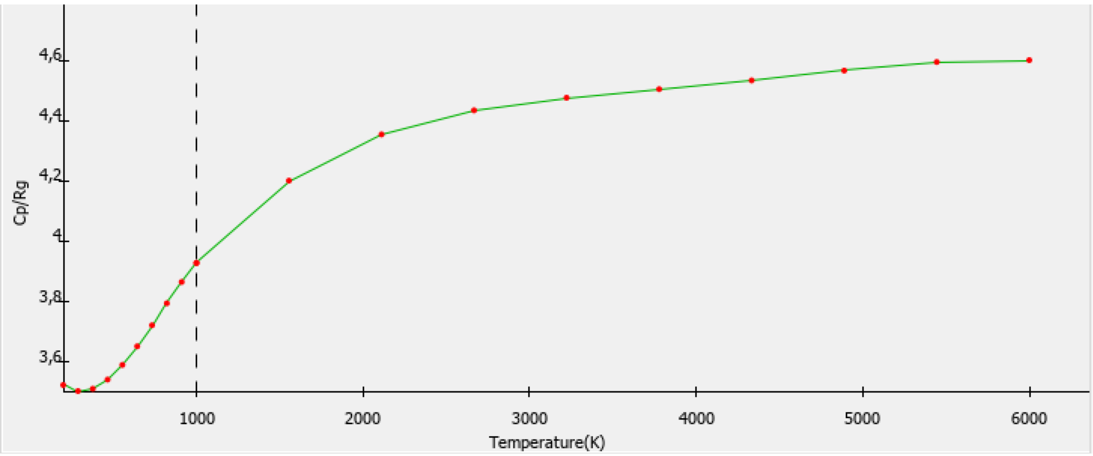

Figure 4.12: Dimensionless Specific Heat of NO^+

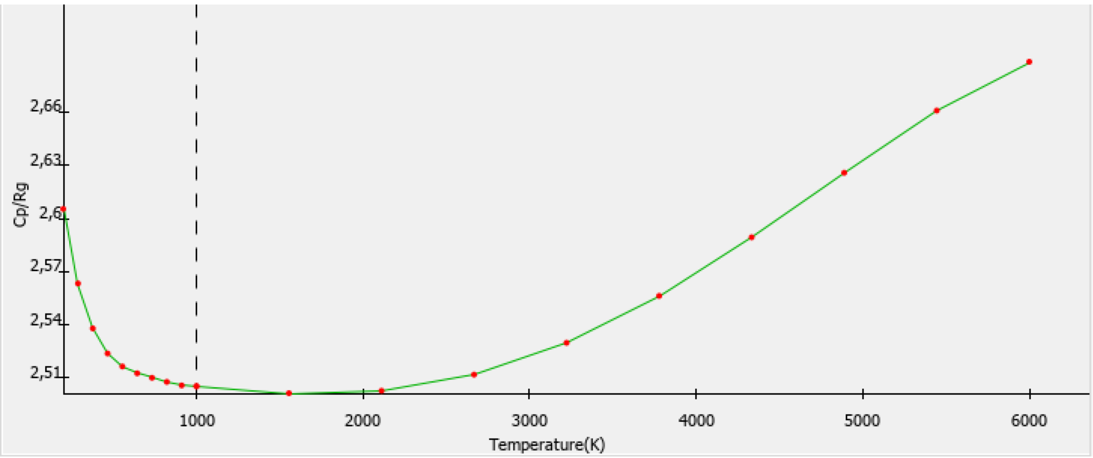

Figure 4.13: Dimensionless Specific Heat of N^+

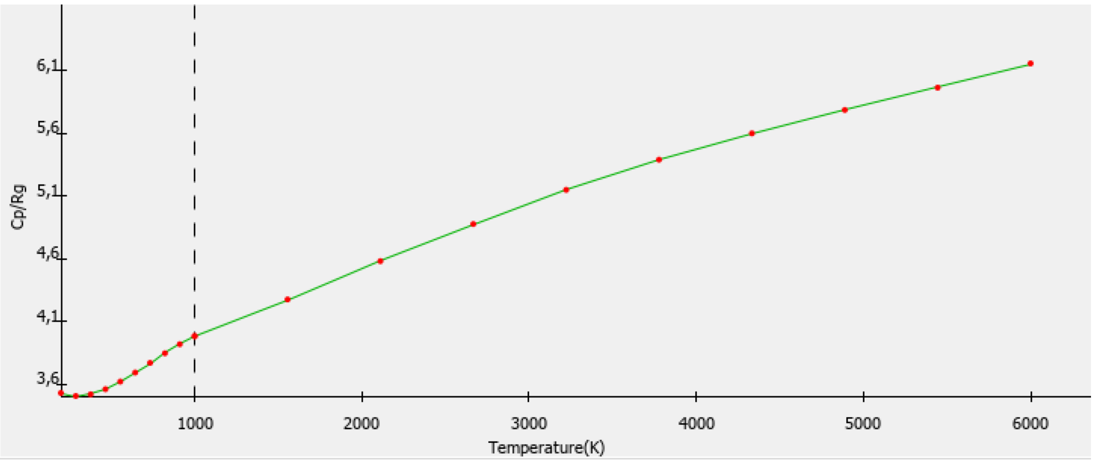

Figure 4.14: Dimensionless Specific Heat of N_2^+

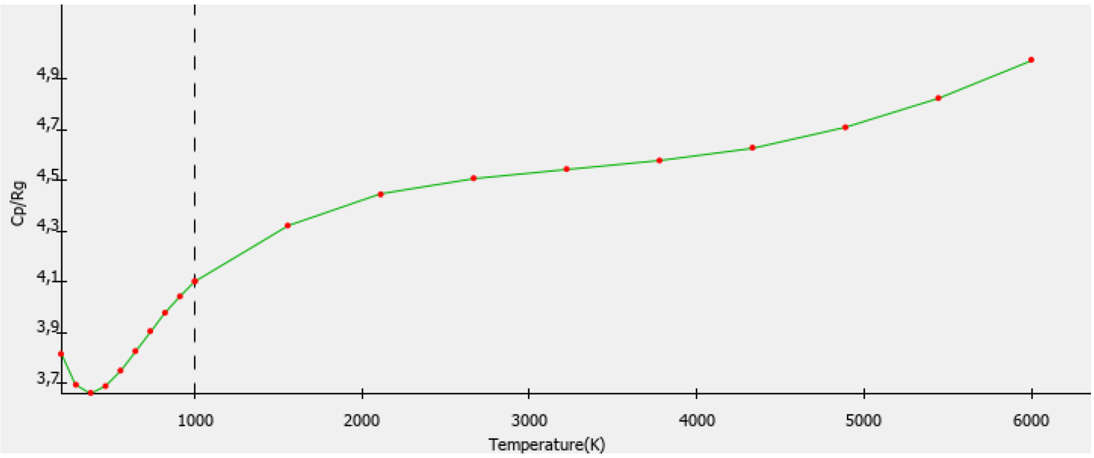

Figure 4.15: Dimensionless Specific Heat of O_2^+

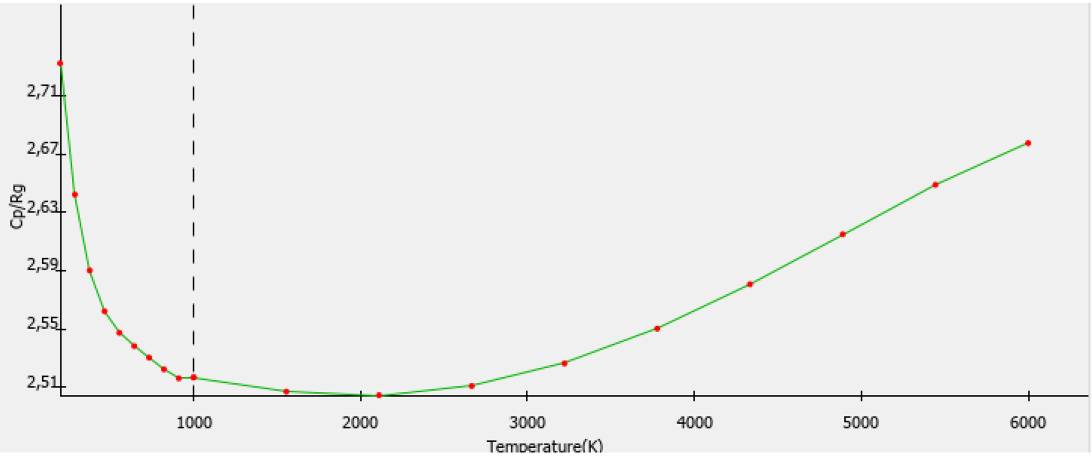

Figure 4.16: Dimensionless Specific Heat of O

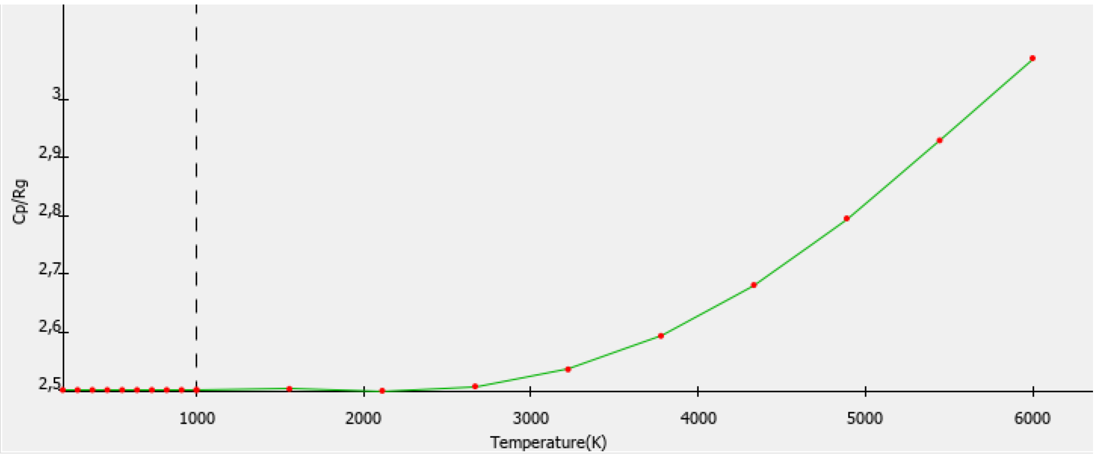

Figure 4.17: Dimensionless Specific Heat of N

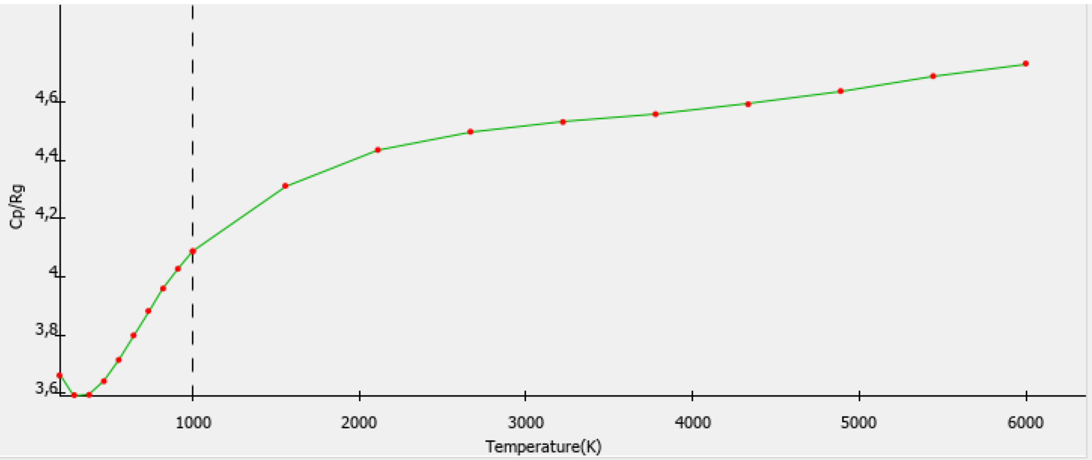

Figure 4.18: Dimensionless Specific Heat of NO

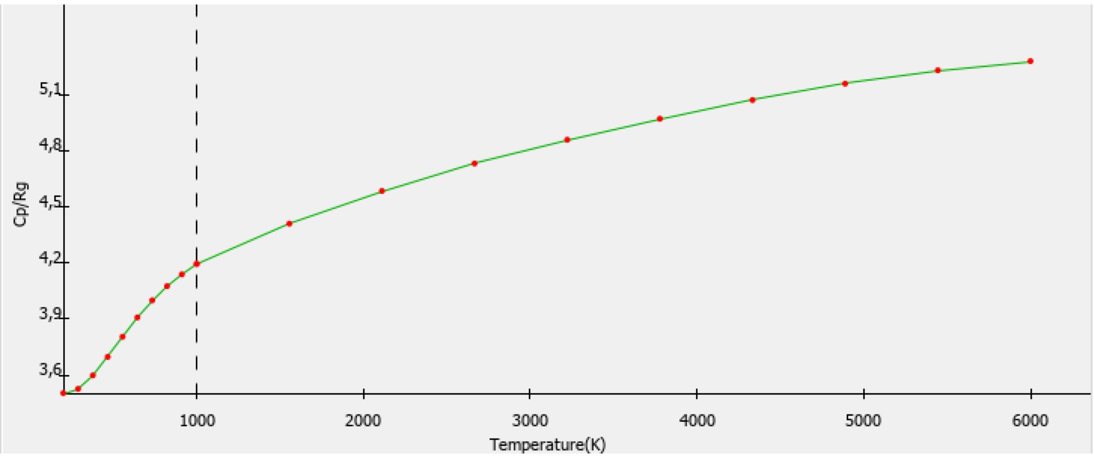

Figure 4.19: Dimensionless Specific Heat of O_2

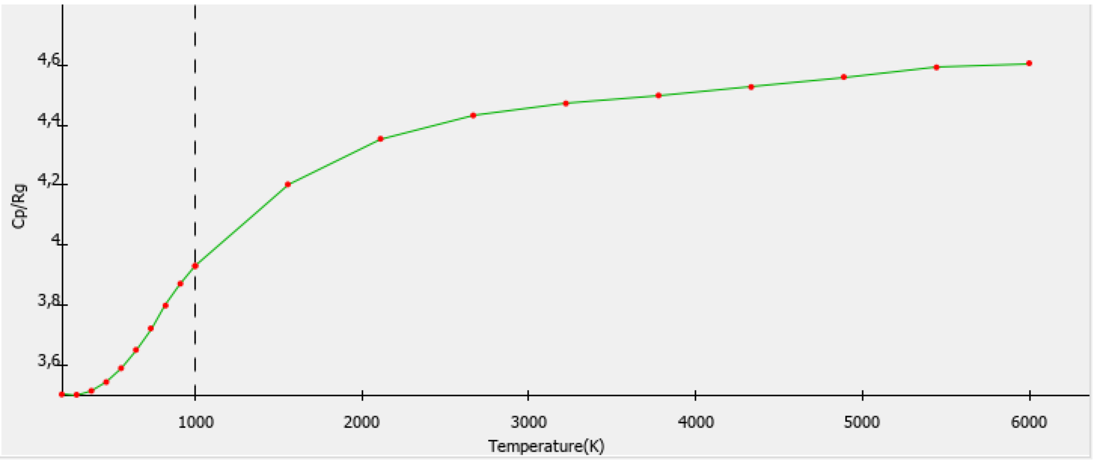

Figure 4.20: Dimensionless Specific Heat of N_2

4.8 Reacting and Reacting species transport

High temperatures trigger chemical processes and the genesis of new species in the flow field. Reacting model properly formulates mixing and reacting of chemical species when certain conditions occur. The reacting species transport model is adopted to couple the conservation equations for all species in a mechanism, including the chemical source term, with the fundamental equations of fluid dynamics. The general species transport equation is formulated as follow:

$$\frac{\partial}{\partial t}\rho Y_i + \frac{\partial}{\partial x_j}\left(\rho u_j Y_i + F_{k,j}\right) = \omega_i \tag{4.30}$$

where $F_{k,j}$ is the diffusion flux component and source term ω_i is the rate of production of species i. The transport equations will be solved for each species in the mixture less one, since the continuity equation must be respected. This implies that the mass fraction of the last species is calculated by difference. Therefore, the sequence with which species properties and reaction data have been inserted in the software has not been arbitrary but it had to take account of catastrophic cancellation. Incorporation of data has been carried out considering the amount of species particles in the mixture: molecular nitrogen data have been the lasts inserted for the analysis while the electrons data have been the firsts. The order of incorporation of data is shown below:

$$e^-, O^+, NO^+, N^+, N_2^+, O_2^+, O, N, NO, O_2, N_2$$

4.8.1 Complex Chemistry

STAR-CCM+, supplies a ODE (Ordinary Differential Equation) solver for integrating the mass fraction species and to obtain the source terms in transport equations. The Complex Chemistry model is suitable for introducing detailed chemistry information to the CFD simulation and it is able to handle hundreds of reactions among hundreds of species, hence the term Complex Chemistry. Given the nature of the solver (ODE solver) this particular model can manage stiff systems. Detailed reaction mechanisms information about species, reactions and thermodynamic properties are supplied to the model by complex chemistry definition files (see 6). In particular, the file contains information about:

- chemical elements;
- chemical species;
- chemical reactions;

- Arrhenius coefficients (Activation energy, temperature exponent, third body efficiency, pre-exponent coefficient.

The operator algorithm performs the time integration of the chemical state (species mass fractions Y_i and temperature T) in two steps, taking advantage of the different time scales involved for the chemical reactions and the flow field:

1. the chemical state is integrated, at the beginning of each time-step, in each CFD cell from state$(Y_i, T, P)^n$ to $(Y_i, T, P)^*$, where only chemical source terms have been taken into account:

$$Y_i^* = Y_i + \int_0^\tau r_i \left(\mathbf{Y}, T, p\right) dt \tag{4.31}$$

   Y_i^* is the mass fraction at the end of a time integration τ ,r_i is the reaction rate defined in the previous chapter, $\mathbf{Y}$ is the mass fraction vector, and T is temperature.

2. the species transport equations are solved with the explicit reaction source term ω_i:

$$\omega_i = \rho \left(\frac{Y_i^* - Y_i}{\tau} \right) \tag{4.32}$$

   ρ is the density;

The two equations (4.31) and (4.32) represent the average rate of change of the species in the cell over the time-step τ. When running with the Steady State model, an artificial chemistry time step is introduced which is based on time residence in the cell:

$$\tau = \frac{m}{\dot{m}} F_{CFL} \tag{4.33}$$

The residence time in a cell is defined as:

$$\tau_{res} = \frac{m}{\dot{m}} \tag{4.34}$$

It follows:

$$\tau = \tau_{res} F_{CFL} \tag{4.35}$$

τ is approximately the residence time in the cell multiplied by the CFL scaling factor F_{CFL} (in these investigations is set to 1). The introduction of the chemical time can be understood as the characteristic time of an average reaction. This method results very helpful to reduce the stiffness of the system. CVODE[86] is the solver used to integrate the stiff chemistry over a time-step τ . The equations that are integrated in the solver correspond to:

$$\frac{dY_i}{dt} = r_i \tag{4.36}$$

$$\frac{dT}{dt} = -\frac{\sum_{k=1}^{n} \dot{r}_i h_i}{c_p} \tag{4.37}$$

where t is time, T is temperature, n is the number of species, ρ is the density, h_i is the enthalpy, c_p is the specific heat. Since the chemical source term, ω, is calculated repeatedly as the ODE solver iterates for each cell, the cost of solving the ODE is expensive and the Clustering computational acceleration method is used[87]. Clustering reduces the computational expense of complex chemistry calculations by averaging together cells with similar chemical compositions, integrating the reduced ODE set, and then interpolating the clusters back to the cells.

4.9 Thermal radiation

4.9.1 Radiative Transfer Equation

All matter that has a temperature greater than absolute zero emits radiation, thus, the Radiation model has been applied to taking into account the radiative effects of high temperature gas mixture in the investigation. It allows to implement in the analysis, radiative transfer and radiation spectrum models. Participating media radiation is the radiative transfer model adopted and it describes the ability of media and particles to absorb, emit or scatter thermal radiation. Grey thermal radiation is the spectral model chosen for the investigations and it defines the radiation properties as wavelength-independent, therefore they will result the same over the entire thermal spectrum. This means that only a single radiative transfer solution is necessary for the full thermal spectrum. The radiative transfer equation models all the mentioned phenomena[88]:

$$\frac{dI}{ds} = -\beta I + k_a I_b + \frac{k_s}{4\pi}\int_{4\pi} I\Omega d\Omega \tag{4.38}$$

where:

- I is the radiative intensity;
- I_b is the black body intensity;
- s is the distance in the Ω direction;
- β is the estinction coefficient defined as:

$$\beta = k_a + k_s \tag{4.39}$$

- k_a is the absorption coefficient ;
- k_s is the scattering coefficient;
- Ω is the solid angle;

The black body intensity is obtained by using the following formula[89]:

$$I_b = \frac{2C_1}{\lambda^5(e^{\frac{C2}{\lambda T}-1})} \tag{4.40}$$

$$C_1 = 0.595522\,x\,10^{-16} \quad \frac{Wm^2}{s} \tag{4.41}$$

and

$$C_2 = 0.01439mK \tag{4.42}$$

Since the mixture has several components, the absorption coefficient k_a is:

$$k_a = \sum_{i}^{N} k_{ai} \tag{4.43}$$

The equation is valid for a fixed wavelength , however the Grey thermal model presumed the properties wavelength-independent. The previous equation is subjected to the boundary condition:

$$I = \varepsilon_w I_b + \frac{\rho_w}{\pi}\int_{\mathbf{n}\cdot\mathbf{s}'<\mathbf{0}} I(\mathbf{s}')|\mathbf{n}\cdot\mathbf{s}'|d\Omega \tag{4.44}$$

with:

- ε_w is the emissivity coefficient

- ρ_w is the reflectivity coefficient
- $\mathbf{s}'$ is the incoming ray direction;
- $\mathbf{n}$ is the outgoing surface normal;
- $\mathbf{n} \cdot \mathbf{s}'$ is the cosine of any incoming director and the surface normal.

The radiant heat flux in a particular direction q_r is calculated using the integration of the radiant intensity over all solid angles and over the wavelength spectrum:

$$q_r(r) = \int_0^{\infty} \int_{4\pi} I(\mathbf{s})\mathbf{s} d\Omega d\lambda \tag{4.45}$$

4.9.2 Discrete Ordinate Method

The Discrete Ordinate Method (DOM) is the tool used to transform the RTE for a grey medium into a set of simultaneous partial differential equations. DOM provides for the discretization of the radiative intensity over a directional variation, therefore the solution to the transport problem is obtained by solving the RTE for a set of directions, spanning the total solid angle range of 4π. The method results in a simply differencing of the directional dependence of the equation of transfer. Integrals over solid angle are approximated by numerical quadrature. The discrete ordinates may be carried out to any arbitrary order and accuracy, although the mathematical formulation of high-order is considerably less involved. In the DOM, the radiative transfer equation is solved for a set of n different directions $\mathbf{s_i'}$ with $i = 1, 2....n$ and the integrals over direction are replaced by numerical quadratures, that is:

$$\int_{4\pi} f(\mathbf{s}') d\Omega \simeq \sum_{i=1}^{n} \omega_i f(\mathbf{s}') \tag{4.46}$$

ω_i are the quadrature weights associated with the directions s_i. Thus, RTE is approximated by a set of n equations (one for each discretized direction),

$$\frac{\partial I}{\partial \mathbf{s}'} = k_a I_b - \beta I + \frac{k_s}{4\pi} \sum_{j=1}^{n} \omega_j I(\mathbf{s}') \Phi(\mathbf{r}, \mathbf{s_j'}, \mathbf{s_i'}) \tag{4.47}$$

subject to the boundary conditions:

$$I = \varepsilon_w I_b + \frac{\rho_w^d}{\pi} \sum_{\mathbf{n \cdot s_j' < 0}} \omega_j I(\mathbf{s}') |\mathbf{n} \cdot \mathbf{s_j'}| \tag{4.48}$$

The scattering is present, therefore an iterative procedure is required to obtain a solution. Once the intensities have been determined the radiative heat flux is readily calculated inside the medium or at a boundaries:

$$\mathbf{q}(\mathbf{r}) = \int_{4\pi} I \mathbf{s}' d\Omega \simeq \sum_{i=1}^{n} \omega_i I_i \mathbf{s_i'} \tag{4.49}$$

One the radiation solution is obtained, it will be coupled to the fluid dynamic solution through the divergence of the radiative heat flux:

$$\nabla \cdot \mathbf{q_r} = \int_{4\pi} I d\Omega \simeq \sum_{i=1}^{n} \omega_i I_i \tag{4.50}$$

The choice of quadrature scheme is not arbitrary: restrictions on the directions $\mathbf{s}'$ and quadrature weights ω_i may arise from the desire to preserve symmetry(invariant after any roation of 90°) and to satisfy certain conditions:

$$\int_{4\pi} d\Omega = 4\pi = \sum_{i=1}^{n} \omega_i \tag{4.51}$$

$$\int_{4\pi} \mathbf{s}' d\Omega = 0 = \sum_{i=1}^{n} \omega_i \mathbf{s}'_\mathbf{i} \tag{4.52}$$

$$\int_{4\pi} \mathbf{s}'\mathbf{s}' d\Omega = \frac{4\pi}{3}\boldsymbol{\delta} = \sum_{i=1}^{n} \omega_i \mathbf{s}'_\mathbf{i}\mathbf{s}' \tag{4.53}$$

$$\int_{\mathbf{n}\cdot\mathbf{s}'_\mathbf{j}<0} |\mathbf{n}\cdot\mathbf{s}'_\mathbf{j}| d\Omega = \int_{\mathbf{n}\cdot\mathbf{s}'_\mathbf{j}>0} |\mathbf{n}\cdot\mathbf{s}'_\mathbf{j}| d\Omega = \pi = \sum_{\mathbf{n}\cdot\mathbf{s}'_\mathbf{j}>0} \mathbf{n}\cdot\mathbf{s}'_\mathbf{j}\omega_i \tag{4.54}$$

$\boldsymbol{\delta}$ is the unit tensor. The set of ordinates and weights that satisfy the all previous requirements have been given by [90].

4.9.3 Electromagnetism

Given the aim at evaluating the effect of the presence of electrically charged particles in the flow field, the Elctromagnetism model had been applied to describe their interactions in terms of electric and magnetic field. The fundamental equations which properly model electromagnetic phenomena in a continuum field are the Maxwell's equation[91]:

$$\frac{\partial \mathbf{B}}{\partial t} + \nabla x \mathbf{E} = 0 \tag{4.55}$$

$$\frac{\partial \mathbf{D}}{\partial t} - \nabla x \mathbf{H} = -\mathbf{J} \tag{4.56}$$

$$\nabla \cdot \mathbf{J} = \rho \tag{4.57}$$

$$\nabla \cdot \mathbf{B} = 0 \tag{4.58}$$

where:

- ρ is the electric charge density;
- **J** is the electric current density;
- **H** is the magnetic field;
- **E** is the electric field;
- **D** is the electric flux density;
- **B** is the magnetic flux density;

However, firsts investigations had be analysed with the electrostatic potential model since the steady state hypothesis of the flow field. In electrostatic application, Siemens STAR-CMM+ calculates the electric field induced by a distribution of electric charges from the electric potential. The electrostatic potential is computed from the following equation[92]:

$$-\oint_S \varepsilon \nabla \Phi \cdot \mathbf{dA} = \int_V \rho dV \tag{4.59}$$

S is the surface which bounds the cell domain V. The equation (4.59) states that the total electric flux through a closed surface is equal to the electric charge that is contained in the volume bounded by the surface . ρ is the electric charged density and the term on the righ-hand side represents the total charge contained in the volume V. The Finite Volume Method is applied to discretize and to solve the (4.59). Once the discretized electrostatic potential is obtained, it is possible to compute the electric field and the electric flux density as follow:

$$\mathbf{E} = -\nabla \Phi \tag{4.60}$$

$$\mathbf{D} = \varepsilon \mathbf{E} \tag{4.61}$$

The particular model allows the user to introduce the electric charge density. This parameters has been computed starting from the number density of the single species. The number density of each species is:

$$n_i = X_i n \tag{4.62}$$

where X_i is the molar fraction and n is the global number density defined as:

$$n = \frac{p}{Tk_b} \tag{4.63}$$

Finally the electric charge density is:

$$\rho = e \sum_{i=1}^{N} l_i n_i \tag{4.64}$$

with e electric charge of the electron[93]:

$$e = 1.602176634 \, x \, 10^{-19} C \tag{4.65}$$

l_i is equal to 1 for positive electrically charged species and equal to -1 for negative ones. Nevertheless, Siemens STAR-CCM+ doesn't allow to couple electromagnetic effects with the aero-thermochemical model set. It has been observed how the amount of charged particles, generated by high temperature effects, gives origin to an electric field but the effects of the latter doesn't affect reactions, species diffusive transport or other flow field properties. It has been decide, due to the limit of the commercial software, to exclude this model in the last simulation(whose results are in 5) .

4.10 Coupled Energy and Coupled flow, Numerical scheme

4.10.1 Equations

Coupled flow model solves continuity, momentum and energy equations simultaneously as a vector of equations. The system of equations in Cartesian, integral, vectorial form for an arbitrary control volume V with a differential surface area dS is:

$$\frac{\partial}{\partial t} \int_V \mathbf{U} dV + \int_S [\mathbf{F} - \mathbf{G}] \cdot d\mathbf{A} = \int_V \mathbf{S} dV \tag{4.66}$$

Where:

$$\mathbf{U} = \begin{bmatrix} \rho \\ \rho\mathbf{v} \\ \rho E \end{bmatrix} \tag{4.67}$$

$$\mathbf{F} = \begin{bmatrix} \rho\mathbf{v} \\ \rho\mathbf{v}\mathbf{v} + p\mathbf{I} \\ (\rho E + p)\mathbf{v} \end{bmatrix} \tag{4.68}$$

$$\mathbf{G} = \begin{bmatrix} 0 \\ \boldsymbol{\tau} \\ \boldsymbol{\tau} \cdot \mathbf{v} + k\nabla T + \sum_{i=1}^{N_s} h_i \rho D_{im} \nabla y_i \end{bmatrix} \tag{4.69}$$

4.10.2 Discretization

A pre-conditioning approach is required to avoid numerical errors on results and reducing system conditioning number, and to provide efficient solution of flows at all speed[94]. The commercial software incorporates a pre-conditioning matrix by multiplying by the transient term of primitive variables:

$$\Gamma \frac{\partial}{\partial t} \int_V \mathbf{Q} dV + \int_S [\mathbf{F} - \mathbf{G}] \cdot d\mathbf{A} = \int_V \mathbf{S} dV \tag{4.70}$$

with

$$\mathbf{Q} = \begin{bmatrix} \rho \\ \mathbf{v} \\ T \end{bmatrix}$$

and Γ is:

$$\Gamma = \begin{bmatrix} \vartheta & 0 & \rho_T \\ \vartheta \mathbf{v} & \rho \mathbf{I} & \rho_T \mathbf{v} \\ \vartheta H - \delta & \rho \mathbf{v} & \rho_T H + \rho c_p \end{bmatrix} \tag{4.71}$$

and:

$$\rho_T = \frac{\partial \rho}{\partial T}|_p \tag{4.72}$$

For ideal gases

$$\delta = 1; \quad \rho_T = -\frac{p}{RT} \tag{4.73}$$

ϑ is defined as:

$$\vartheta = \frac{1}{U_R^2} - \frac{\rho_T}{\rho c_p} \tag{4.74}$$

Reference velocity U_R has been chosen such that the system remains well-conditioned. This is accomplished by limiting the reference velocity such that it is equal or greater than local convection velocity or the diffusion velocity. An additional limitation is considering local pressure differences effects to increase numerical stability in stagnation regions by avoiding amplification of pressure perturbations there. Reference velocity is so defined as follow:

$$U_R = min \left[max \left(|\mathbf{v}|, \frac{\nu}{\Delta x}, \varepsilon \sqrt{\frac{\delta p}{\rho}}, U_{Rmin}, \right), U_{Rmax} \right] \tag{4.75}$$

where Δx is the cell length scale over which the diffusion occurs and δP is the pressure difference between adjacent cells. For compressible flows, the maximum reference velocity U_{Rmax} is limited to the local speed of sound, a. The scaling parameter ε is set to 2. Applying the volume finite method to the cell-centered control volume, the discretized system for the i-th cell is:

$$V_i \boldsymbol{\Gamma_i} \frac{\partial \mathbf{Q_i}}{\partial t} + \sum_{j}^{N_{faces}} (\mathbf{f_j} - \mathbf{g_i}) \Delta S_j = 0 \tag{4.76}$$

An Euler implicit scheme has been adopted to discretize the equation (4.70), since the steady nature of the problem:

$$\left(V_i \frac{\mathbf{\Gamma_i}}{\Delta t} + \sum_{j}^{N_{faces}} \mathbf{S_{j,w}} \Delta S \right) \boldsymbol{\Delta Q_i} = -\mathbf{R_i^k} \tag{4.77}$$

Where:

$$\boldsymbol{\Delta Q_i} = \mathbf{Q_i^{k+1}} - \mathbf{Q_i^k} \tag{4.78}$$

$$\mathbf{S_{j,w}} = \frac{\partial \mathbf{F_j}}{\partial \mathbf{Q_w}} - \frac{\partial \mathbf{G_j}}{\partial \mathbf{Q_w}} \tag{4.79}$$

and the residual vectors:

$$\mathbf{R_i^k} = \left(\sum_{j}^{N_{faces}} \mathbf{f_j} - \mathbf{g_j} \right)^k \tag{4.80}$$

The Courant number is set to 1.0 due to the instabilities which would arise otherwise while the time step is:

$$\Delta t = min(\frac{V_i CFL}{\lambda_{max,i}}) \tag{4.81}$$

. where V_i is the volume of the i-th cell and λ_{max} is the maximum eigen value of the system (4.66). Δt is the minimum in the whole domain.

4.10.3 Inviscid fluxes

Inviscid fluxes for the (4.70), are essentially calculated using Liou's AUSM+ Scheme, particular Upwind-differencing methods which take into account the effective direction of propagation of signals in the flow field. The scheme can capture contact discontinuity as well as stationary shock. Moreover, the use of this method results in improvement in accuracy, such as removing post-shock overshoot[95]. For sake of simplicity, the convective fluxes have been modeled below for a one-dimensional analysis on the cell face:

$$f_{j+\frac{1}{2}} = m_{j+\frac{1}{2}} a_{j+\frac{1}{2}} \Phi_{j+\frac{1}{2}} \tag{4.82}$$

where m is a function of Mach number only, a is the speed of sound and Φ is the generic transported variable. Mach number function m is split as follow:

$$m_{j+\frac{1}{2}} = m^{+}(M_j) + m^{-}(M_{j+1}) \tag{4.83}$$

Where Mach number split functions $m^{\pm}(M)$ are:

$$m^{\pm}(M) = \begin{cases} \frac{1}{2}\left(M \pm |M|\right) & if \quad |M| \geq 1 \\ m_{\beta}^{\pm} & otherwise \end{cases} \tag{4.84}$$

with

$$m_{\beta}^{\pm} = \pm\frac{1}{4}(M \pm 1)^2 \pm \beta(M^2-1)^2 \qquad -\frac{1}{16} \leqslant \beta \leqslant \frac{1}{2} \tag{4.85}$$

$a_{j+\frac{1}{2}}$ and $\Phi_{j+\frac{1}{2}}$ are expressed considering the direction of propagation of signals (in this case expressed by m):

$$a_{j+\frac{1}{2}} = \begin{cases} a_j & if \quad m_{j+\frac{1}{2}} \geq 0 \\ a_{j+1} & otherwise \end{cases} \tag{4.86}$$

$$\Phi_{j+\frac{1}{2}} = \begin{cases} \Phi_j & if \quad m_{j+\frac{1}{2}} \geq 0 \\ \Phi_{j+1} & otherwise \end{cases} \tag{4.87}$$

Pressure flux instead, is defined as:

$$P_{j+\frac{1}{2}} = P^{+}(M_j)pj + P^{-}(M_{j+1})p_{j+1} \tag{4.88}$$

Pressure split function is:

$$P^{\pm}(M) = \begin{cases} \frac{1}{2}(1 \pm sign(M)) & if \quad |M| \geq 1 \\ P_{\alpha}^{\pm} & otherwise \end{cases} \tag{4.89}$$

where

$$P_{\alpha}^{\pm}(M) = \frac{1}{4}(M \pm 1)^2(2 \mp M) \pm \alpha M(M^2-1)^2 \qquad -\frac{3}{4} \leqslant \alpha \leqslant \frac{3}{16} \tag{4.90}$$

It has been proved that the couple of values $(\alpha, \beta) = (\frac{3}{16}, \frac{1}{8})$ returns more accurate results owing to the presence of higher-degree terms in $(m_{\beta}^{\pm}, P_{\alpha}^{\pm}(M))$ [95].

4.10.4 Diffusive fluxes

The generic diffusive flux g on the face $j + \frac{1}{2}$ instead, is expressed as a diffusion coefficient multiplied by the gradients of the transported variable and by the surface area vector:

$$g_{j+\frac{1}{2}} = (\Gamma \nabla \Phi \mathbf{a})_{j+\frac{1}{2}} \tag{4.91}$$

STAR-CMM+ applies the following decomposition to obtain a second order accurate scheme[71]:

$$\nabla \Phi_{j+\frac{1}{2}} = (\Phi_{j+1} - \Phi_j)\boldsymbol{\alpha} + \overline{\nabla \Phi_{j+\frac{1}{2}}} - (\overline{\nabla \Phi_{j+\frac{1}{2}}} \cdot \mathbf{ds})\boldsymbol{\alpha} \tag{4.92}$$

where:

$$\boldsymbol{\alpha} = \frac{\mathbf{a_{j+\frac{1}{2}}}}{\mathbf{a_{j+\frac{1}{2}}} \cdot \mathbf{ds}}; \quad \mathbf{ds} = \mathbf{x_{j+1}} - \mathbf{x_j}; \quad \overline{\nabla\Phi}_{j+\frac{1}{2}} = \frac{\nabla\Phi_{j+1} + \nabla\Phi_j}{2} \tag{4.93}$$

$\mathbf{x_j}$ and $\mathbf{x_{j+1}}$ are the coordinates centroids of cell-j and that of the neighbor cell $j+1$, addressed through face $j+\frac{1}{2}$, while $\mathbf{a_{j+\frac{1}{2}}}$ is the face area-vector. Therefore, diffusive fluxes are:

$$D_{j+\frac{1}{2}} = \Gamma_{j+\frac{1}{2}} \nabla\Phi_{j+\frac{1}{2}} \cdot \mathbf{a_{j+\frac{1}{2}}} = \Gamma_{j+\frac{1}{2}} \left[(\Phi_{j+1} - \Phi_j)\boldsymbol{\alpha} \cdot \mathbf{a_{j+\frac{1}{2}}} + \overline{\nabla\Phi}_{j+\frac{1}{2}} \cdot \mathbf{a_{j+\frac{1}{2}}} - (\overline{\nabla\Phi}_{j+\frac{1}{2}} \cdot \mathbf{ds}) \cdot \boldsymbol{\alpha} \cdot \mathbf{a_{j+\frac{1}{2}}} \right] \tag{4.94}$$

$\Gamma_{j+\frac{1}{2}}$ is an harmonic average of cell values. Second and third term in equation (4.94) represent secondary gradients contributes (cross diffusion effects) and they are fundamental to maintain high accuracy for non-orthogonal meshes.

4.10.5 Gradients

In addition to cell variables, gradients variables are also required for computing secondary gradients in diffusive fluxes. Steps for computing gradients are the following:

1. computing the unlimited reconstruction gradients where unlimited means that the gradients do not prohibit the reconstructed field variable on the cell faces from exceeding the minimum and maximum values of the neighboring cells. Hybrid Gauss-Least Squares method will be applied for this step[96];
2. limiting the reconstruction gradients.

Hybrid Gauss-Least Squares Method allows to compute the unlimited reconstruction gradients for the cell-j $(\nabla\Phi)^u_{r,j}$ through the following hybrid formula:

$$(\nabla\Phi)^u_{r,j} = \sum_f (\Phi_{j+1} - \Phi_j)\boldsymbol{w_f} \tag{4.95}$$

with:

$$\boldsymbol{w_f} = \boldsymbol{\beta w_f^{LSQ} + (1 - \beta) w_f^{G}} \tag{4.96}$$

$$\boldsymbol{w_f^{LSQ}} = \left[\sum_f \frac{\mathbf{ds} \otimes \mathbf{ds}}{\mathbf{ds} \cdot \mathbf{ds}} \right]^{-1} \frac{\mathbf{ds}}{\mathbf{ds} \cdot \mathbf{ds}} \tag{4.97}$$

$$\mathbf{ds} = \mathbf{x_{j+1}} - \mathbf{x_j} \tag{4.98}$$

$$\boldsymbol{w_f^{G}} = \frac{\mathbf{a_f}}{V_j + V_n} \tag{4.99}$$

Φ_j and Φ_{j+1} are data values in cell-j and its neighbor $J+1$, $\mathbf{a_f}$ is the face area-vector, V_j and V_{j+1} are the respective cell volumes, and β is the geometric Gauss-LSQ gradient blending factor field function. The Gauss/LSQ gradient blending factor is used to determine how the two options of computing are used in calculating the gradient. The reconstruction of gradients is unlimited, therefore the reconstructed face values can fall outside the range of cell values found in neighboring cells (connected through faces). STAR-CMM+ finds the minimum and maximum bounds of the neighboring cell values and uses these to limit the reconstruction gradients. For each cell-j, a limited reconstruction gradient is required, such that the reconstructed face value does not exceed the maximum and minimum of the neighboring cell centroid values, including the value in cell-j. A scale factor $\alpha_{j+\frac{1}{2}}$ is defined that expresses the ratio of the limited and unlimited values (limiter), that is:

$$(\nabla\Phi)_{r,j} = \alpha_{j+\frac{1}{2}} (\nabla\Phi)^u_{r,j} \tag{4.100}$$

And for each cell-j the quantities:

$$\Phi_j^{max} = max(\Phi_j, \Phi_{neighbours}) \tag{4.101}$$

$$\Phi_j^{min} = min(\Phi_j, \Phi_{neighbours}) \tag{4.102}$$

$\Phi_{neighbours}$ represents cell value in each neighbor that has a common face with cell-j. Defining the following variables:

$$\Delta_{max} = \Phi_j^{max} - \Phi_j \tag{4.103}$$

$$\Delta_{min} = \Phi_j^{min} - \Phi_j \tag{4.104}$$

$$\Delta_{j+\frac{1}{2}} = \Phi_{j+\frac{1}{2},} - \Phi_j = \mathbf{S_j} \cdot (\nabla\Phi)^u_{r,j} \tag{4.105}$$

where:

$$\mathbf{ds_{j+\frac{1}{2}}} = \boldsymbol{x_{j+\frac{1}{2}}} - \boldsymbol{x_j} \tag{4.106}$$

Then

$$r_{j+\frac{1}{2}} = \begin{cases} \frac{\Delta_{j+\frac{1}{2}}}{\Delta_{max}} & for \quad \Delta_{j+\frac{1}{2}} > 0 \\ \frac{\Delta_{j+\frac{1}{2}}}{\Delta_{min}} & for \quad \Delta_{j+\frac{1}{2}} \leq 0 \end{cases} \tag{4.107}$$

Venkatakrishnan limiter is defined as follow[97]:

$$\alpha_{j+\frac{1}{2}} = \frac{2r_{j+\frac{1}{2}} + 1}{r_{j+\frac{1}{2}}(2r_{j+\frac{1}{2}} + 1) + 1} \tag{4.108}$$

Limiters are essentially used to prevent spurious oscillations in the flow field which would otherwise appear in the solution, close to the shock[98].

4.11 Numerical Solvers

4.11.1 Algebraic system

The result of the discretization is an algebraic system:

$$\mathbf{Ax} = b \tag{4.109}$$

The system represents the set of algebraic equations for each computational cell. A is the matrix representing the coefficients of the linear system, x is the vector of the unknowns in each cell and b is the vector of residuals from each cell. The solution will be reached by a double cycle of iteration:

- an internal cycle where the iterative process will be used to solve the algebraic system;
- an external cycle where the proceeding of iterations are equivalent to a time march. The iterations continue till a steady solution is obtained.

4.11.2 Gauss-Seidel method

The present section describes the method adopted to solve the algebraic system for each time-step. Iterative methods are principally based on the search of a better approximation $\mathbf{x^{k+1}}$ starting from an approximate solution $\mathbf{x^k}$. The process is repeated till an accurate solution is reached. The error at iteration k is defined as:

$$\mathbf{e^k} = \boldsymbol{x} - \boldsymbol{x}^k \tag{4.110}$$

where $\mathbf{x}$ represents the exact solution. The residual vector is:

$$\mathbf{r^k} = \mathbf{b} - \mathbf{A}\boldsymbol{x^k} \tag{4.111}$$

it follows that:

$$\mathbf{A}\mathbf{e}^{\mathbf{k}} = \mathbf{r}^{k} \tag{4.112}$$

Therefore, the iterations continue till the residuals are sufficiently small. Jacobi and Gauss-Seidel are the most basic iterative methods. The method adopted to solve the algebraic system is the Gauss-Seidel iterative approach. According to Gauss-Seidel method [99], matrix **A** is split as follow:

$$\mathbf{A} = \mathbf{E} + \mathbf{D} + \mathbf{F} \tag{4.113}$$

where:

- **E** is the strictly lower triangular part of the matrix A;
- **D** is the diagonal part of matrix A;
- **F** is the strictly upper triangular part of matrix A;

The iterative process to obtain $\boldsymbol{x}^{\boldsymbol{k}+\mathbf{1}}$ is:

$$(\mathbf{E} + \mathbf{D})\boldsymbol{x}^{\boldsymbol{k}+\mathbf{1}} = \mathbf{b} - \mathbf{F}\boldsymbol{x}^{\boldsymbol{k}} \tag{4.114}$$

it follows:

$$\boldsymbol{x}^{\boldsymbol{k}+\mathbf{1}} = \mathbf{D}^{-1}(\mathbf{b} - \mathbf{E}\boldsymbol{x}^{\boldsymbol{k}+\mathbf{1}} - \mathbf{E}\boldsymbol{x}^{\boldsymbol{k}}) \tag{4.115}$$

4.11.3 Algebraic Multigrid

Mesh size is a significant parameter that influences the speed through which conventional iterative solution algorithms (such as Jacobi or Gauss-Seidel method) converge. Therefore the increase of the mesh size brings to the increase of computational time. To reduce computational effort and accelerate solution convergence, the Algebric Multigrid (AGM) method is employed. This particular technique is based on the principle that an iterative solution algorithm (Jacobi or Gauss-Seidel method for example) reduces efficiently the numerical high frequency errors whose wave lengths is comparable to the cell size. Low frequency errors instead, are just reduced with the multigrid approach. This kind of errors are reduced through an iterative process on a hierarchy of coarser and coarser linear systems. The coarse grid are derived from arithmetic combination of the fine grid properties. After several iterations, the multigrid algorithm transfers the computation from the fine grid to a coarser one. These iterations have the effect of reducing high frequency errors and so they are called smoothing iterations. The passage to a coarser grid means an higher cell size and, therefore the old low frequency errors are now high frequency errors (for the corresponding coarse grid) and they can be efficiently mitigated. The Multigrid algorithms essentially apply three general steps[100, 101]:

1. Formation of a coarser grid level from agglomerating cells;
2. Restriction: the residual are transferred from a fine level to a coarser level;
3. Propagation: the corrected and reduced residual are newly transferred from the coarse level back to a finer level.

The type of cycling among the coarse meshes has a strong impact in the efficiency of algorithm and solution. There are two available types of cycle for accelerating the solving procedure:

- Flexible cycles;
- Fixed cycles.

The firsts are essentially used for linear systems that are not stiff. Multigrid levels are not used in a regular pattern and the residuals are monitored after every iteration on a given grid level. The flexible cycle checks the residual rate of reduction, when the given threshold is exceeded, the iteration process is transferred to a coarser level. If the residual on a given level, instead, are lower than a specified tolerance, the solution moves to a finer level. The seconds are the multigrid fixed cycles which consist in a recursive application of a single cycle with a regular pattern composed of different steps:

1. Pre-smooth by using few iterations of the Gauss-Seidel methods to the equations on the current fine level;

2. Residual computation where the existing residuals are transferred down to the coarsest level;

3. Cycle anew where a new cycle is applied;

4. Prolongation involves the resultant corrections to be transferred back up to the current fine level;

5. Post-smooth on the solution on the fine level;

The most used fixed cycles for two-dimensional flows are the V, W, and F Cycles. The V cycle is the simplest type of fixed cycle, and it only has two "legs". First, iterations on the finest level are performed and then the residuals are transferred to the next level. Finally, the operation is repeated on coarser levels until the coarsest one is reached. The procedure is illustrated below:

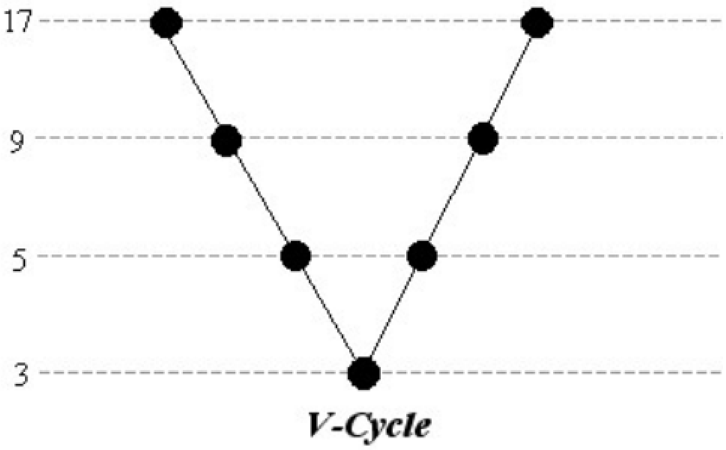

Figure 4.21: schedules of grid for V-cycle[13]

The V Cycle may be not sufficient for an accurate solution, therefore more coarse iterations are required. The W cycle increases the number of coarse iterations with the scheme illustrated in the following figure:

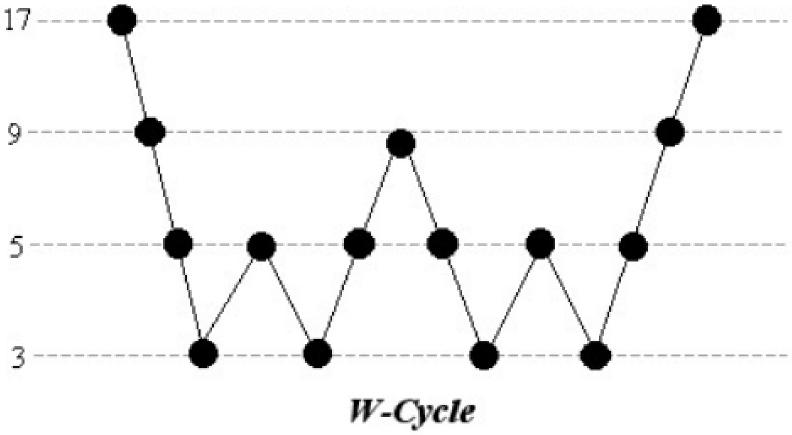

Figure 4.22: schedules of grid for W-cycle[13]

The F-cycle is a variant of W-cycle. This cycle involves fewer coarse-level sweeps than the W cycle, but still more than the V cycle:

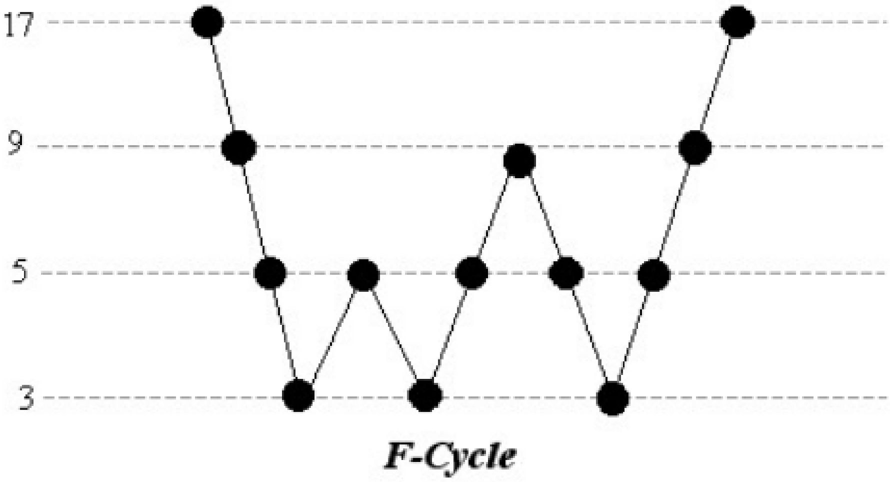

Figure 4.23: schedules of grid for F-cycle[13]

In the current investigations, F-cycle is set as cycling fixed procedure with the following properties:

- No pre-smooth iterations;
- 2 post-smooth iterations;
- the maximum number of levels of coarse grids is equal to 50;
- convergence tolerance set to 0.05;
- Max number of cycles set to 30 (in case the convergence tolerance is not met);

4.11.4 Preconditionated Biconjugated Gradient Stabilized Method

However, STAR-CMM+ implements an AMG-preconditioned Biconjugated Gradient Stabilized (BiCGStab) algorithm to improve the robustness and the speed of convergence to reach solution[102]. BiCGStab is a particular method of descent where the solution of the algebraic system is reached by moving after each iteration the $\mathbf{x^k}$ along a particular direction. Defining the solution $\bar{\mathbf{x}}$ as the only minimum of the function $J(\mathbf{x})$:

$$J(\boldsymbol{x}) = \frac{1}{2}\boldsymbol{x}^{\boldsymbol{T}} A\boldsymbol{x} - \boldsymbol{x}^{\boldsymbol{T}}\mathbf{b} \tag{4.116}$$

$$J(\bar{\boldsymbol{x}}) = min J(\boldsymbol{x}) \tag{4.117}$$

An acceptable direction $\mathbf{p}$ requires to respect the following condition:

$$\frac{\partial J}{\partial \mathbf{p^k}}(\boldsymbol{x^k}) = \nabla J(\boldsymbol{x^k})^T \mathbf{p^k} < 0 \tag{4.118}$$

That is, the iterative process is directed towards the minimum of the function $J(\mathbf{x})$. BiCGStab method adopted a particular direction detailed in the algorithm below:

Algorithm 1 Preconditioned Biconjugated Gradient Stabilized Method

```
$\mathbf{r_0} = \mathbf{b} - \mathbf{A}\boldsymbol{x}_\mathbf{0}$
$\tilde{\mathbf{r}} = \mathbf{r_0}$
$\rho_0 = \alpha = \omega_0 = 1$
$\mathbf{v_0} = \mathbf{p_0} = \mathbf{0}$
for i=1, 2... do
    $\rho_i = \tilde{\mathbf{r}}^\mathbf{T} \cdot \mathbf{r_{i-1}}$
    if $\rho_i = 0$ then
        Method fails
    else
        $\beta = \left(\frac{\rho_i}{\rho_{i-1}}\right)\left(\frac{\alpha}{\omega_{i-1}}\right)$
        $\mathbf{p_i} = \mathbf{r_{i-1}} + \beta(\mathbf{p_{i-1}} - \omega_{i-1}\mathbf{v_{i-1}})$
        $\tilde{\mathbf{p}} = AMG(\mathbf{A}, \mathbf{p_i})$
        $\mathbf{v_i} = \mathbf{A}\tilde{\mathbf{p}}$
        $\alpha = \frac{\rho_i}{\rho_{i-1}}$
        $\mathbf{s} = \boldsymbol{r_{i-1}} - \alpha\mathbf{v_i}$
        if $|\mathbf{s}| < \varepsilon_1$ then
            $\mathbf{x_i} = \mathbf{x_{i-1}} + \alpha\tilde{\mathbf{p}}$ and stop
        else
            $\tilde{\mathbf{S}} = AMG(\mathbf{A}, \mathbf{S})$
            $\mathbf{t} = A\tilde{\mathbf{S}}$
            $\omega_i = \frac{\mathbf{t^T \cdot S}}{\mathbf{t^T \cdot t}}$
            $\mathbf{x_i} = \mathbf{x_{i-1}} + \alpha\tilde{\mathbf{p}} + \omega_i\mathbf{s}$
            $\mathbf{r_i} = \mathbf{S} - \omega_i\mathbf{t}$
            if $|\mathbf{r_i}| < \varepsilon_2$ then
                Stop
            else if $\omega_i \neq 0$ then
                Continue
            end if
        end if
    end if
end for
end
```

The BiCGStab method guarantees a faster descent towards the minimum of the function $J(\boldsymbol{x})$. The pre-conditioning operations allow to reduce the number of iterations and to accelerate the convergence process.

4.12 Initialization

The simulations will be carried out considering a typical altitude of 20 kms, therefore the initial conditions in the whole flow field are[103]:

- a temperature $T = 216.65$ K;
- a pressure $p = 5456.55$ Pa;
- a density $\rho = 0.088\,\frac{kg}{m^3}$;
- a speed of sound $a = 295.07\,\frac{m}{s}$;
- a molecular oxygen mass fraction $Y_{O2} = 0.233$;
- a molecular nitrogen mass fraction $Y_{N2} = 0.767$;
- an air speed $v = 2950.7$ corresponding to a Mach number $M = 10$.

However, before the iterative process starts, a grid-sequencing initialization has been carried out since a faster and a more robust convergence of solution is obtained. This process performs a normal initialization followed by the computation of an inviscid solution of the flow field. The grid-sequencing performs the following steps:

1. it generates a series of coarse meshes;
2. a normal initialization of the flow field is performed on each coarse mesh;
3. starting from the coarsest mesh, a number of iterations is reached to obtain the inviscid solution. When the maximum number of iterations or convergence is reached, the previous steps are repeated on the next finer mesh till the finest is reached.

The Grid-Sequencing initialization in the analysis presents the following properties:

- 10 levels of coarse meshes;
- a maximum number of iterations for level equal to 50;
- a convergence tolerance for level set to 0.05.

Chapter 5

Results

This final chapter is committed to show the results obtained in this work. First, the boundary conditions defined in the numerical simulation are presented, and then, numerical results are discussed. Finally a benchmark analysis is presented.

5.1 Boundary Conditions

The boundary conditions define the numerical solution of the flow field. The contour of the computing domain has been split into 4 parts: inflow, outflow, nose and axis. For each of them, different boundary conditions have been set. The free-stream boundary condition is used for the inflow and outflow regions. The flow properties have been set as follow :

- angle of attack equal to 0;
- Mach number equal to 10;
- Temperature $T = 216.65K$;
- Pressure $p = 5456.55Pa$
- Molecular oxygen mass fraction $Y_{O2} = 0.233$;
- Molecular nitrogen mass fraction $Y_{N2} = 0.767$;

These conditions have been set considering the previously mentioned typical operational altitude of a hypersonic cruise missile, adopting a quote of 20 Kms. The Mach number has been chosen taking into account the typical speed of the kh-47M2 Kinzhal whose characteristics have been properly described in Chapter 2. The nose missile has been considered as a wall. The conditions are:

- no slip;
- adiabatic-radiative wall;
- non catalytic wall;
- Surface Emissivity equal to 0.8;
- Surface Reflectivity equal to 0.2;
- Surface Transmittivity equal to 0.

The no slip condition provides for a null velocity at wall due to the viscous flow and the impermeable body. The adiabatic-radiative wall condition expects the heat flux at wall to be null and, consequently, the temperature at wall is obtained as an output of the following equation:

$$q_{gw} + q_{rad} = 0 \tag{5.1}$$

where q_{gw} is the heat flux of the gas at the wall and q_{rad} is the heat radiated from the wall. A non-catalytic wall instead, implies that atoms and molecules strike the wall but no chemical reactions occur, even if temperature allows recombination or dissociation among the species. The radiative properties at wall have been set considering the typical values for metal alloys [104]. The axis condition is required since the axisymmetrical model adopted. This condition is used to specify the missile axis of symmetry.

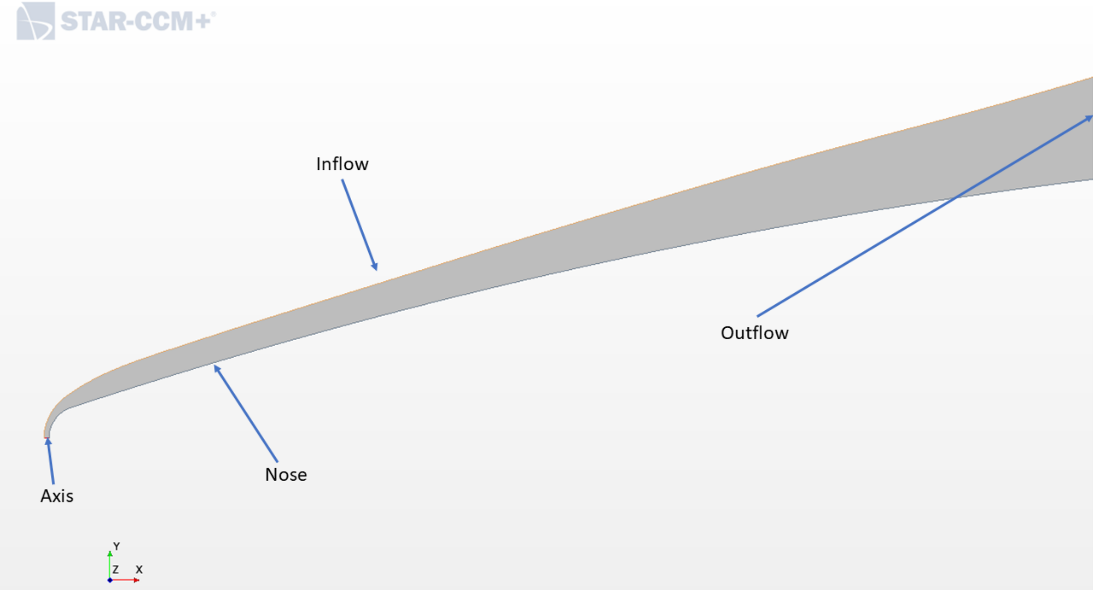

Figure 5.1: Regions of the domain

5.2 Numerical Results

In this section numerical results of the investigation are presented, pointing out the properties of the fluid-dynamic field and how these have been affected by high temperature effects. Fig 5.2 shows how the Mach number strongly decreases through the shock wave, reaching the null value at wall since the no-slip condition. The highest values of the Mach number can be observed in the region characterized by a certain inclination of the bow shock, where the effects of the discontinuity are less intense. The lowest values in the flow field instead, are reached in the nearby of the stagnation line (axis), where the shock is normal to the direction of the free stream and its effects are much more notable. The air flow in this region is almost stationary, and it increases its speed as it moves far from the normal shockwave. Fig5.3 points out the extension of the subsonic pocket. It has been possible to highlight this area by setting the maximum value in the Mach number range to 1, so that Mach numbers higher than this limit are not shown in the domain. The subsonic pocket covers a very small region of the computational domain, as expected from a HCM. This area, due to the intense shock, is interested by the highest rise of entropy and, therefore, maximum loss of total pressure. However, a small subsonic pocket means loss of total pressure and entropy rise strongly localized, equivalent to a reduced wave drag.

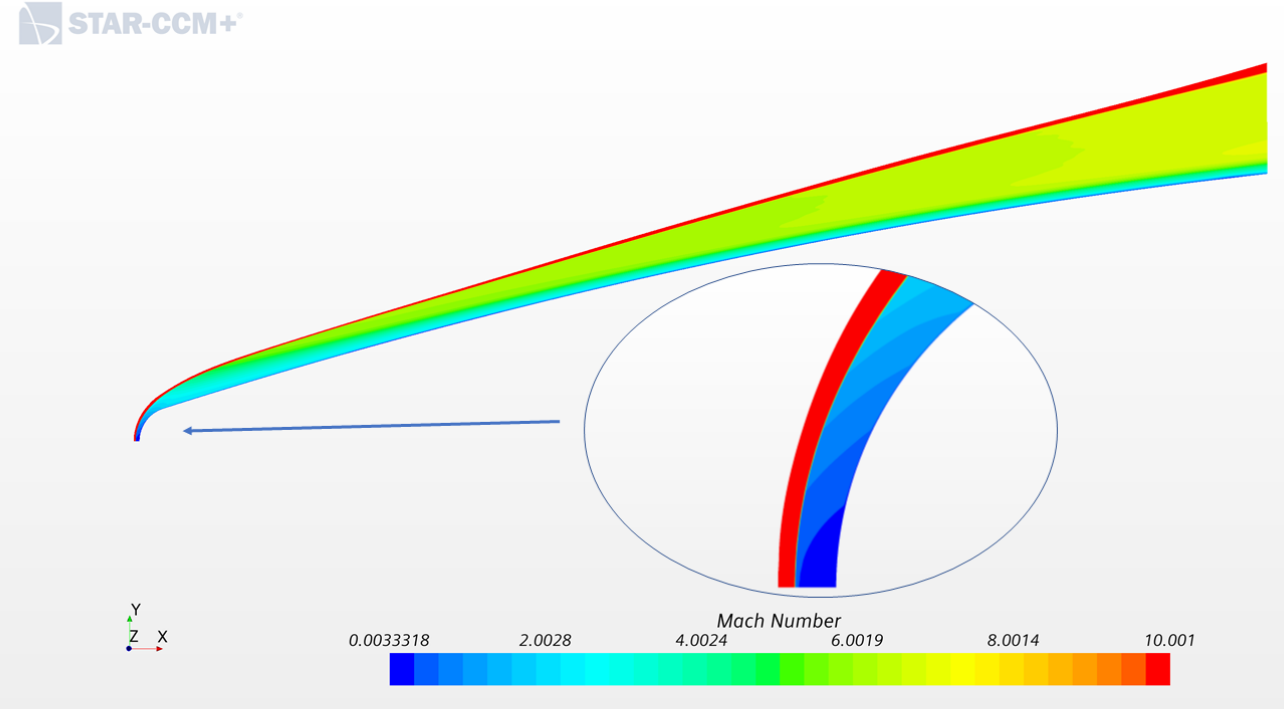

Figure 5.2: Mach Number Field

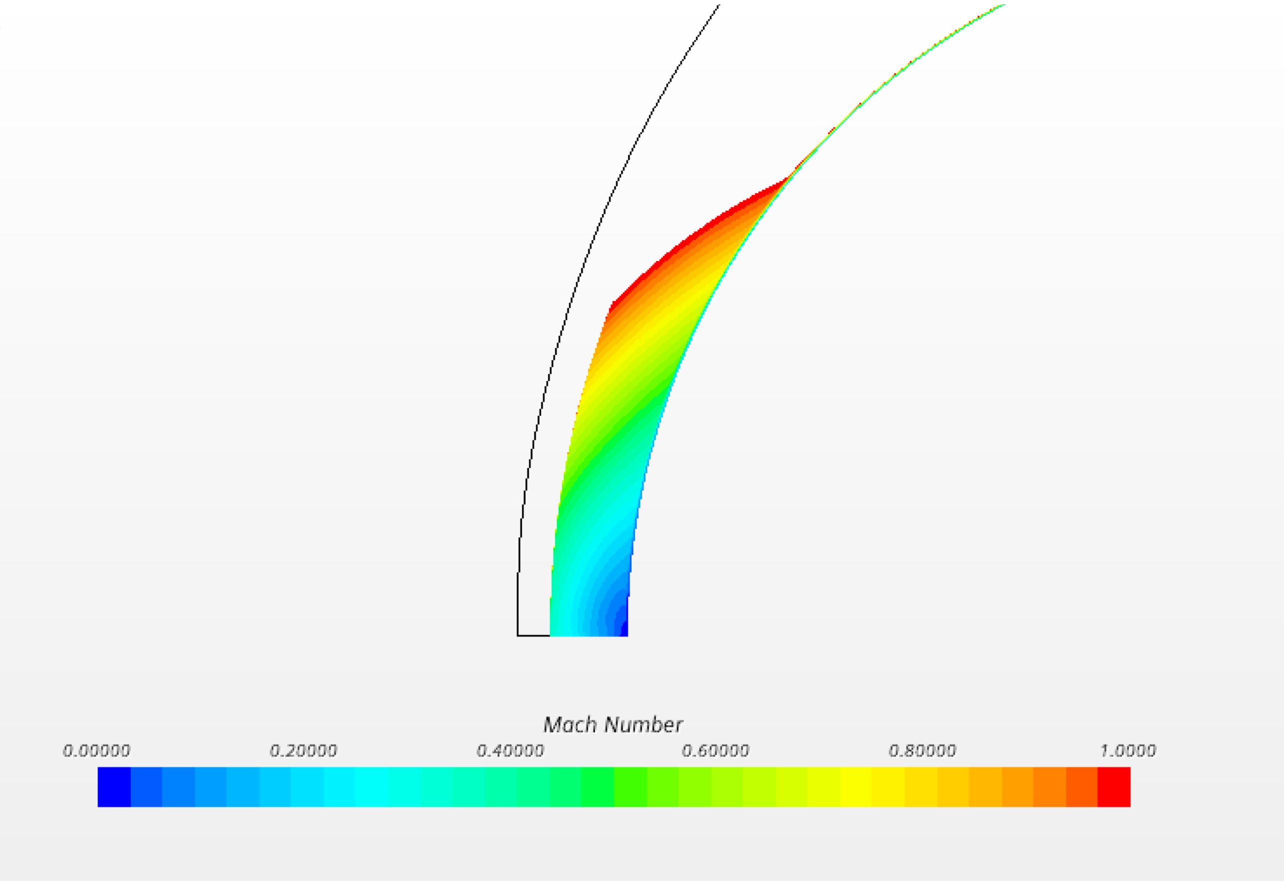

Figure 5.3: Subsonic pocket

The Fig 5.5 shows the pressure distribution along the axis. As expected, the air flow is strongly compressed through shock wave, until reaching about 144 times the free stream value in the subsonic pocket. As already underlined, the highest compression in the field occurs where the shock is normal to the free stream. As the shock-wave decrease its inclination, a mitigated compression is observed.

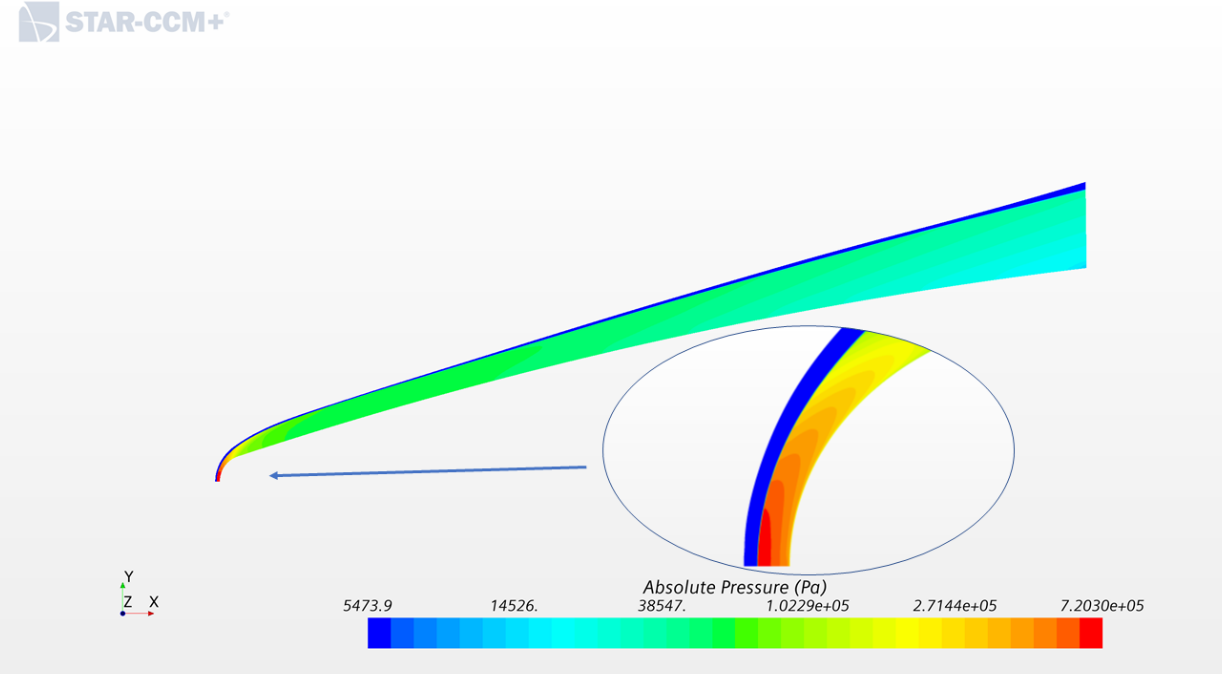

Figure 5.4: Pressure Field

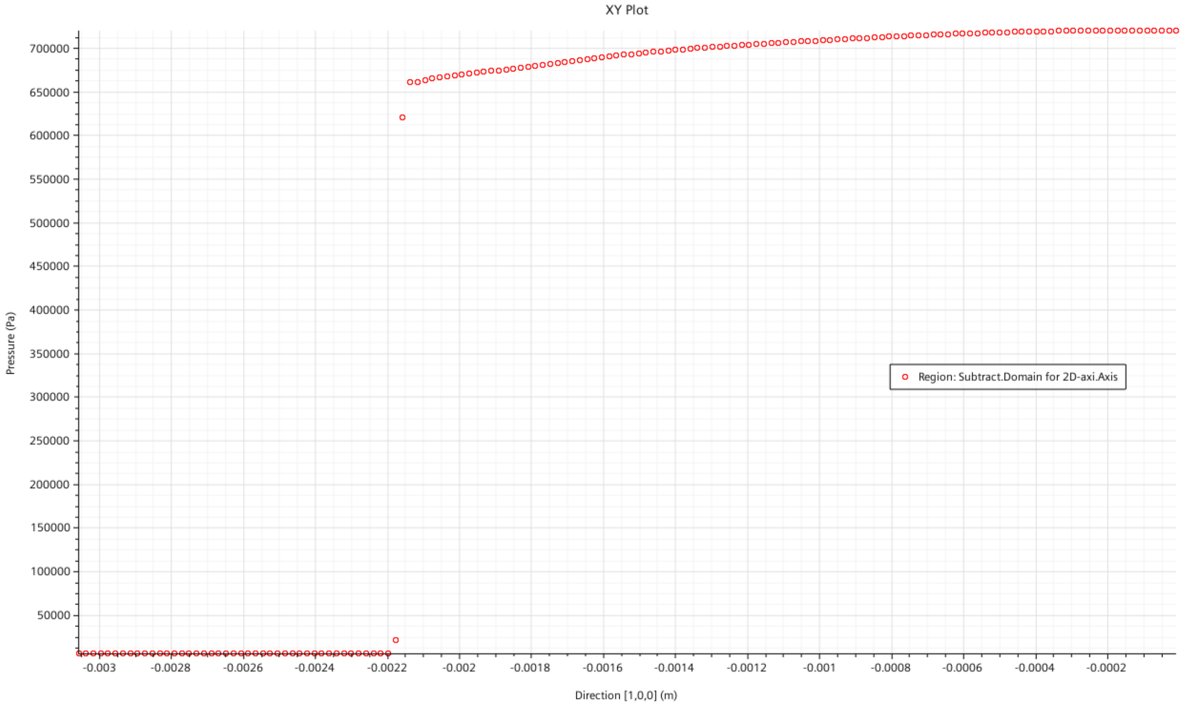

Figure 5.5: Pressure along the Axis

It results very interesting to observe the density field represented in Fig. 5.6. The limit value of density ratio for calorically perfect gases for an infinite Mach number is [11]:

$$\bar{\rho} = \frac{\gamma + 1}{\gamma - 1} = 6 \qquad \gamma = 1.4 \tag{5.2}$$

The results show values well above this limit. This phenomenon can be explained noting that, since the flow is chemically reacting, the specific heat ratio is not constant anymore. As it has been already discussed in the chapter 2, specific heat is a function of temperature only, and, when the latter increases, vibrational and electronic energy modes must be taken into account. These phenomena make the density ratio capable of reaching value far above 6. Furthermore, increased values of density imply a reduced stand-off distance of the bow shock respect to the calorically perfect gas. Observing the thermodynamic properties of the flow along axis represented in Fig5.5, 5.7 and 5.26, it is possible to detect the stand off distance of the bow shock and considered it equal to $0.0023m$. However this is an approximation due to the approach adopted to obtain the solution ("shock capturing" technique). The shock-wave, indeed, has been captured within a certain number of cells, therefore the discontinuity of the fluid dynamic variables is spread over a finite region (about four cells).

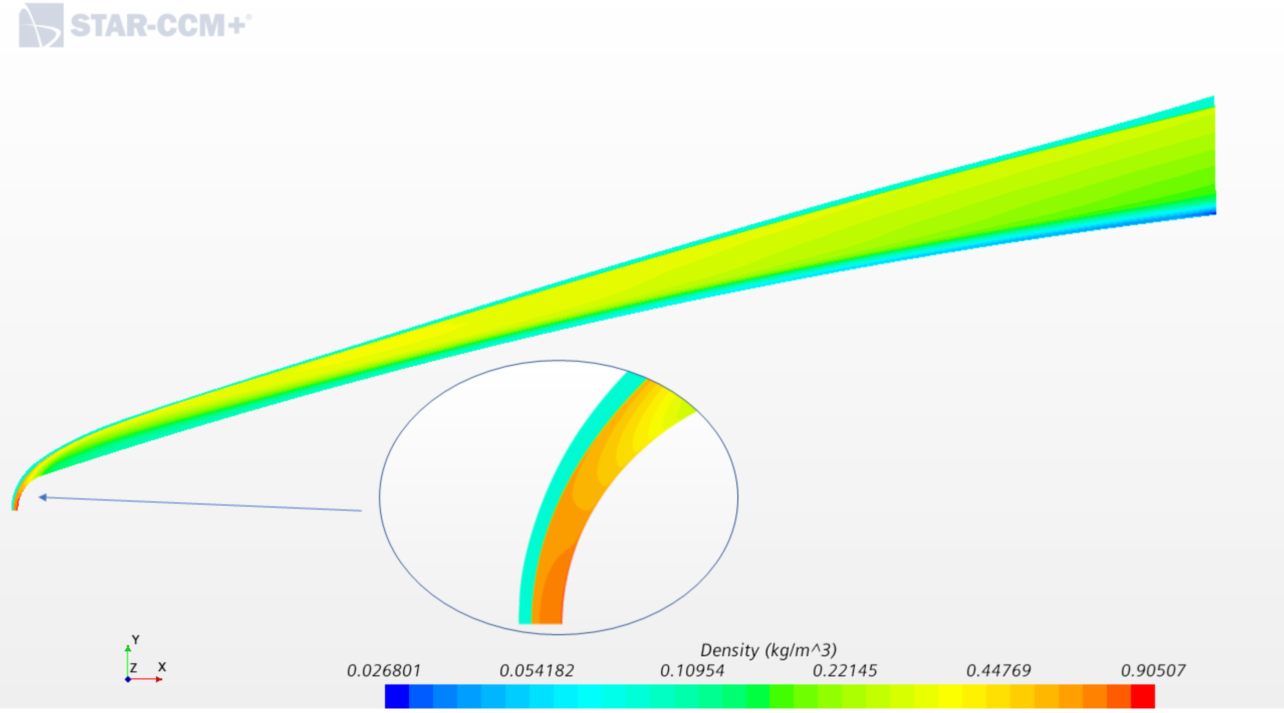

Figure 5.6: Density Field

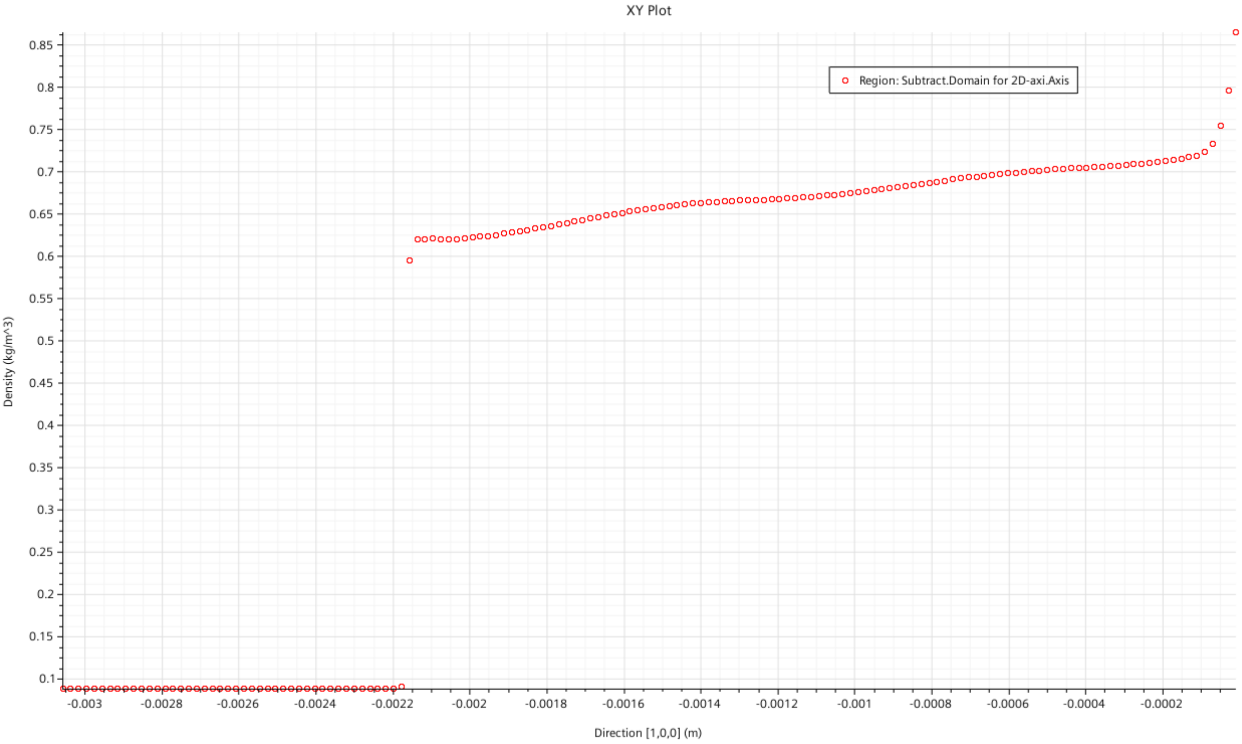

Figure 5.7: Density along Axis

As well as density and pressure, temperature field highlights critical values downstream of the normal shock-wave. The values of temperature reached in the flow field are high enough to allow the occurrence of chemical reactions and to give origin to new chemical species. Observing the Fig.5.5, 5.7 and 5.26, it can be noted that thermodynamic variables do not remain uniform, but change gradually along the axis direction. However, these slow, but appreciable variation, is significant of how much thermo-chemical processes, triggered by the high temperatures, affect the flow field properties. Considering the distribution of temperature at wall in the figure 5.10, the highest values in proximity of the stagnation region suggest the need for a thermal protection system for the HCM. Temperature quickly reduces moving along the wall and its last values at the end of the computational domain, show oscillations in the distribution owing to the boundary conditions: those cells must respect the conditions at wall, and at the same time, they have to take into account the pressure outlet condition in the outflow region.

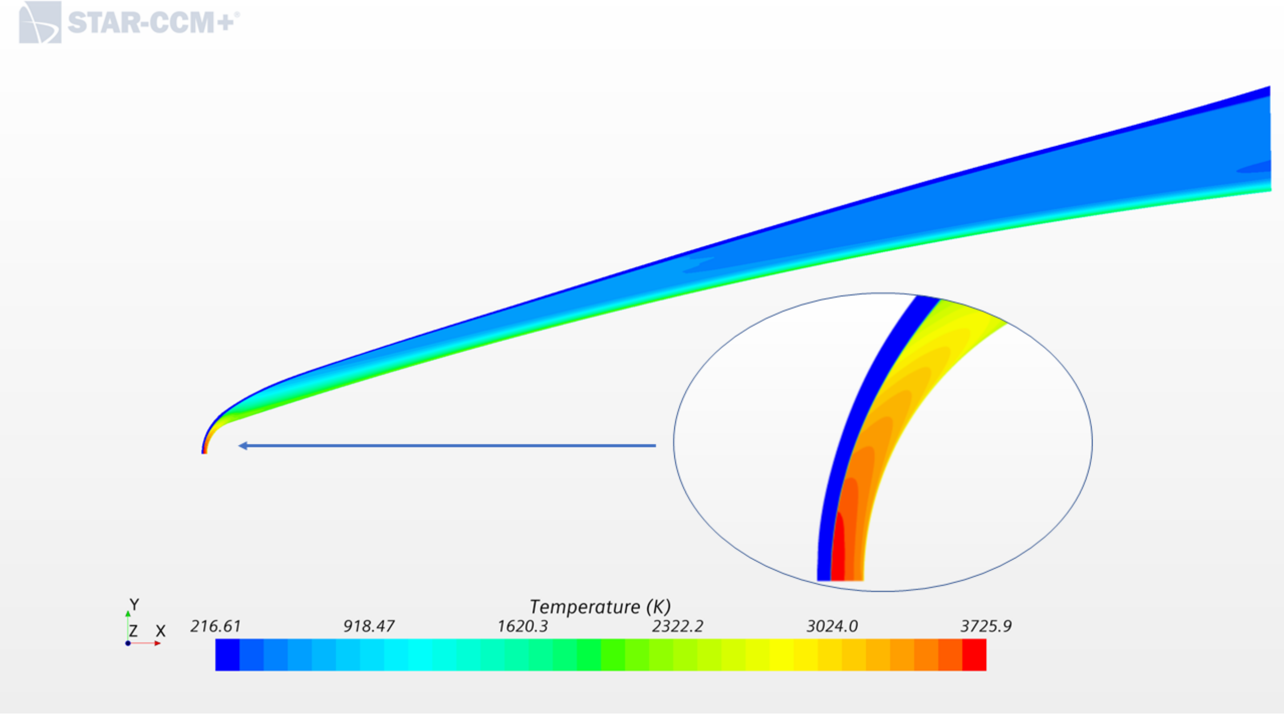

Figure 5.8: Temperature Field

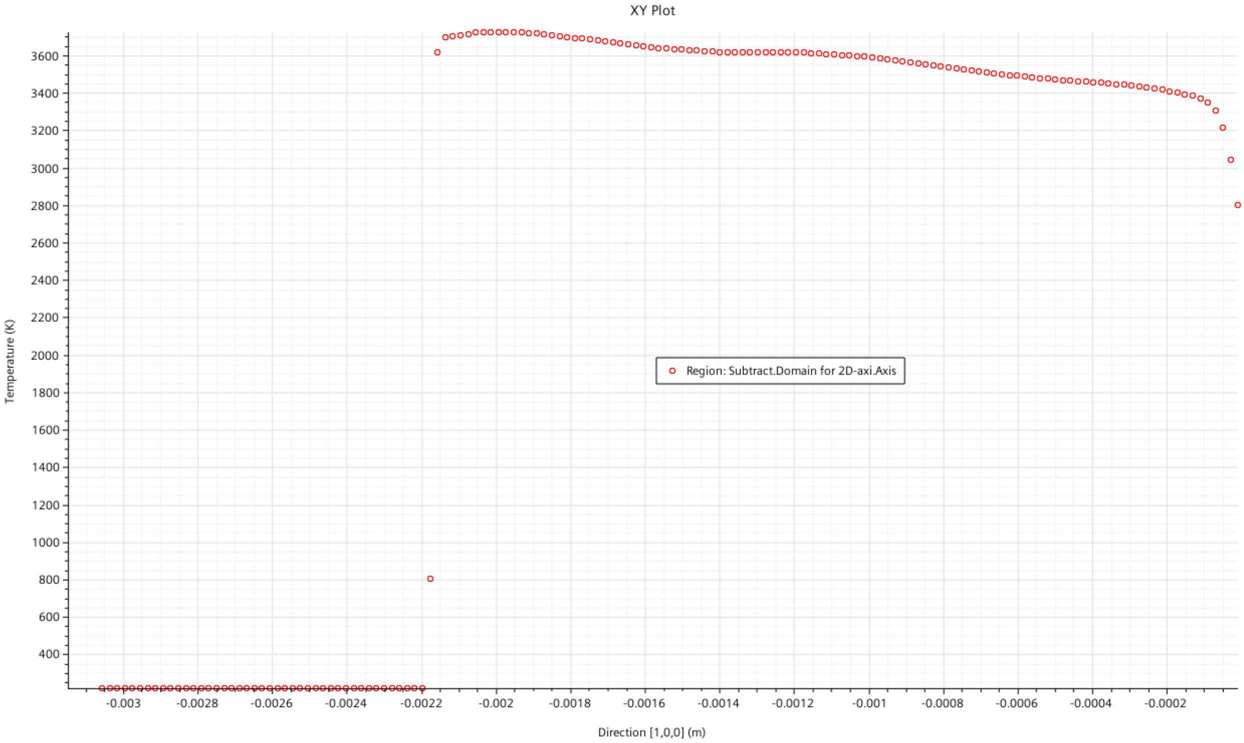

Figure 5.9: Temperature along Axis

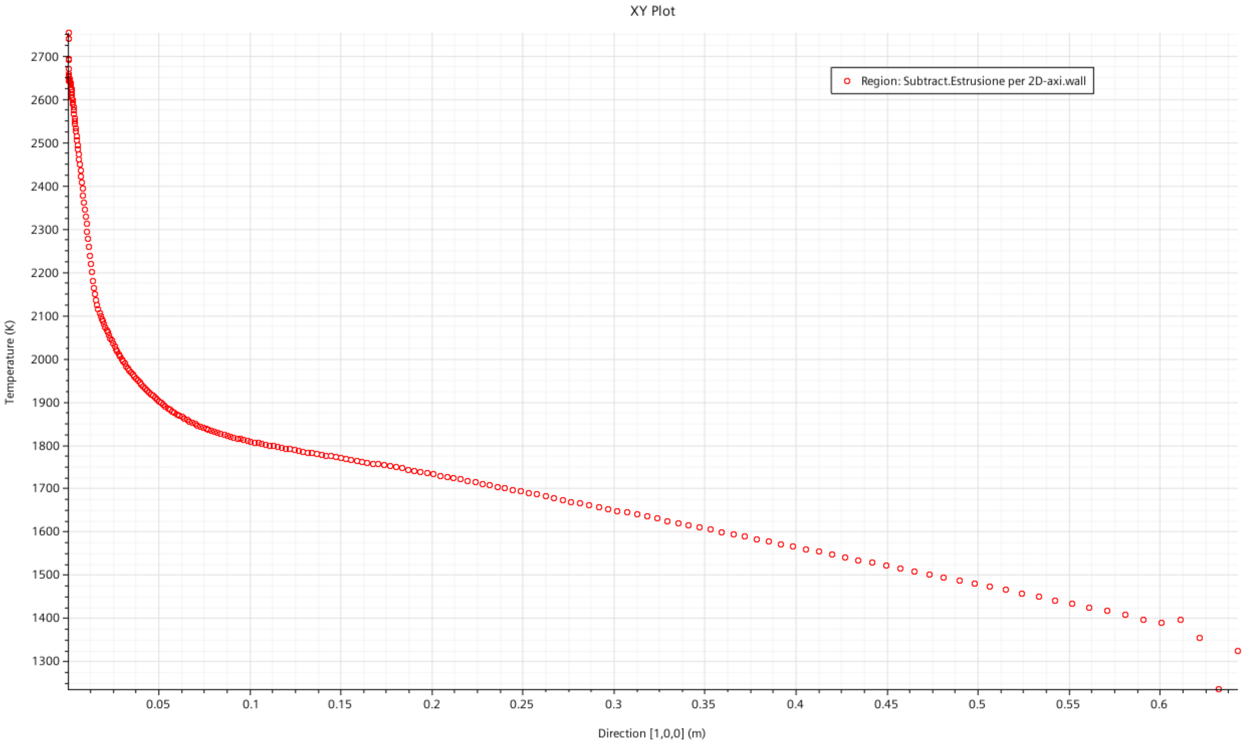

Figure 5.10: Temperature distribution at wall

Observing the mole fractions of neutral species in the figures from 5.11 to 5.15, it is possible to note a not negligible dissociation of the O_2 and, consequently, presence of atomic oxygen. Results show that the most intense dissociation of molecular oxygen is localized in the subsonic pocket where an high concentration of O is revealed. Since the reaction of dissociation is endothermic it causes a reduction of temperature along the axis, as presented in figure 5.16. A steeper reduction would be noted if temperature was sufficiently high to trigger N_2 dissociation reaction. Nevertheless, molecular nitrogen starts dissociating when temperature is over $4000\,K$ (at 1 atm), therefore, only a very small amount of N is observable in the subsonic pocket. The small quantity of nitric oxide observable in figure 5.13 can be justified considering that NO is generally formed at $2500K$ in an air flow in equilibrium condition at 1 atm [11]. Furthermore, it can be glimpsed a change of slope of the curves close to the wall. The mole fractions curves of O_2 and O remain quite horizontal, and this effect may be indicative of a local chemical equilibrium condition. This phenomenon occurs since the lowest speed in the flow fields is reached near the wall, therefore characteristic chemical times are much smaller than convective time and reactions take place very quickly.

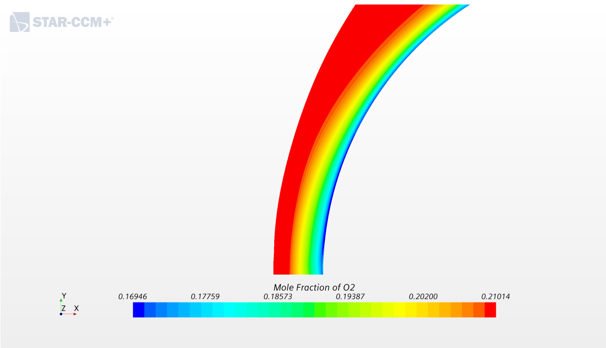

Figure 5.11: O_2 mole fraction distribution

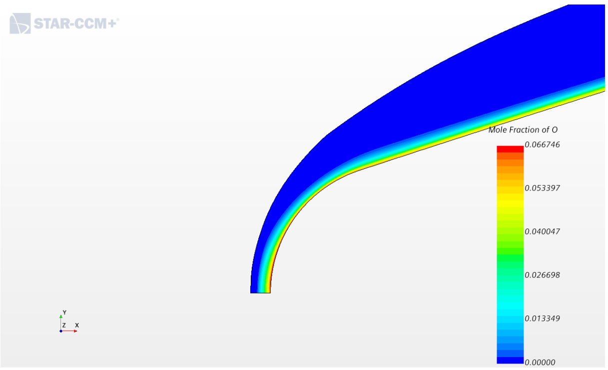

Figure 5.12: O mole fraction distribution

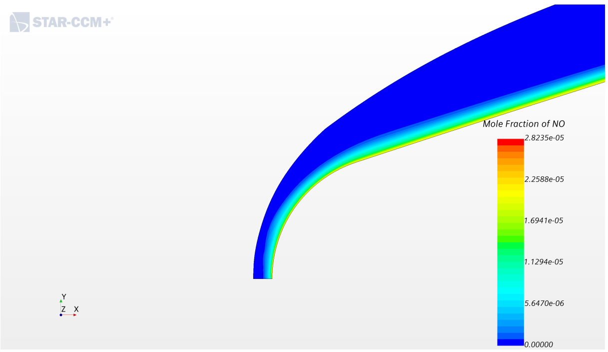

Figure 5.13: NO mole fraction distribution

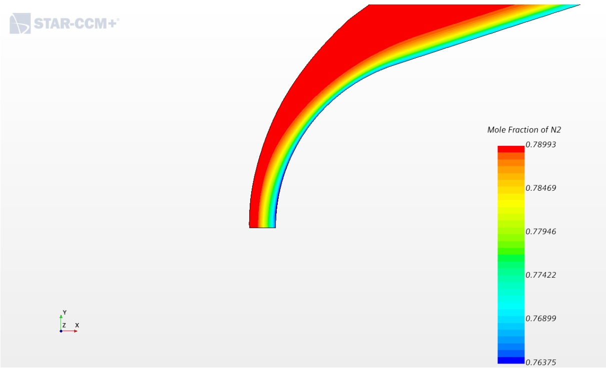

Figure 5.14: N_2 mole fraction distribution

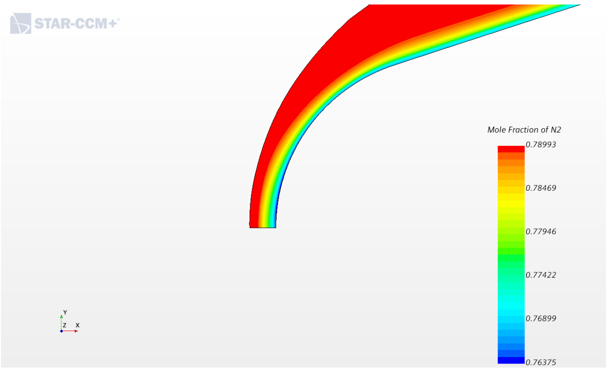

Figure 5.15: N mole fraction distribution

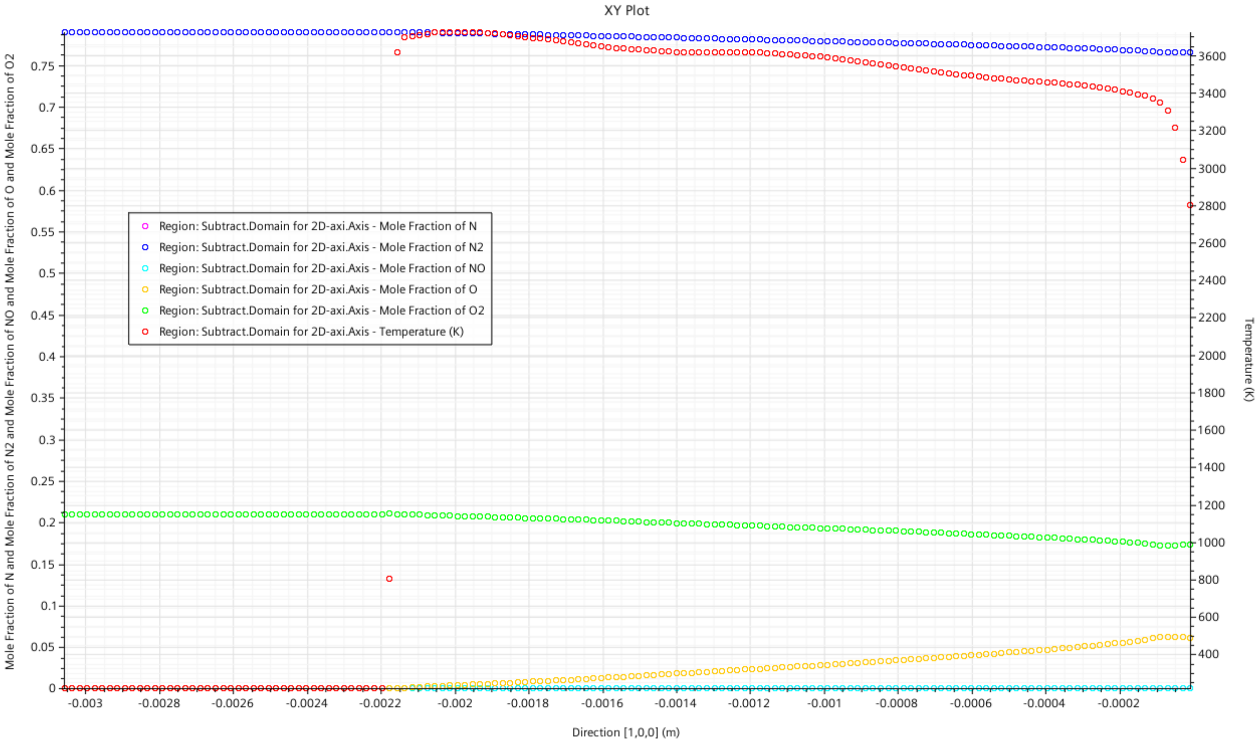

Figure 5.16: mole fractions distribution along axis

It can be easily deduced, from the previous results, that ionization phenomena are quite few. Temperatures in the flow field are far below $9000K$, which is the typical value for ionization to be relevant (at 1 atm). The Mach number of the free stream is, in fact, too low to generate high enough temperatures and to observe an appreciable amount of charged particles in the shock layer. However, it is still possible to note a very small quantity of electrons and NO^+ because of the ionization of NO, since a mild ionization of nitric oxide generally occurs between 4000 and $6000K$. Figures 5.17 and 5.19 highlight slightly higher moles fraction at wall compared to the others. Nevertheless, it is fundamental to underline that the "on set" temperature for ionization and dissociation of the species, are strongly affected by the air flow pressure. Increasing or decreasing the air pressure respect to 1 atm, respectively increases or decreases these limit values of temperature, as shown in chapter 3.

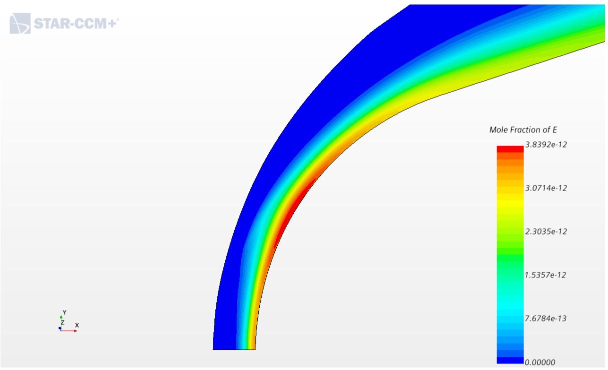

Figure 5.17: e^- mole fraction distribution

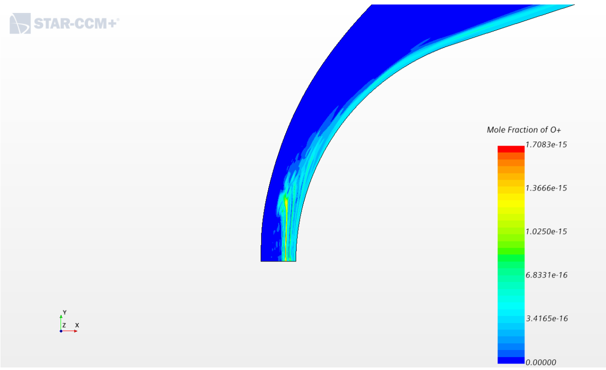

Figure 5.18: O^+ mole fraction distribution

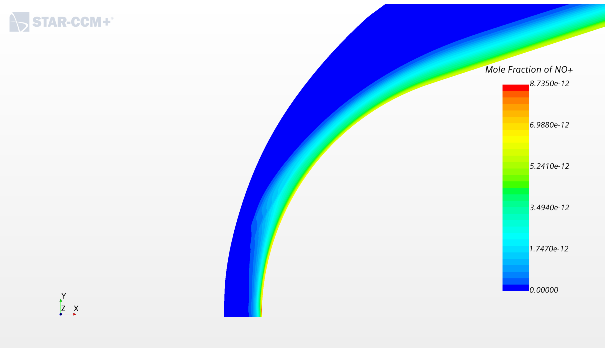

Figure 5.19: NO^+ mole fraction distribution

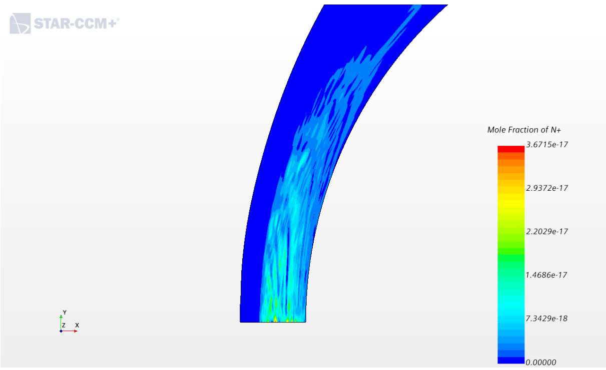

Figure 5.20: N^+ mole fraction distribution

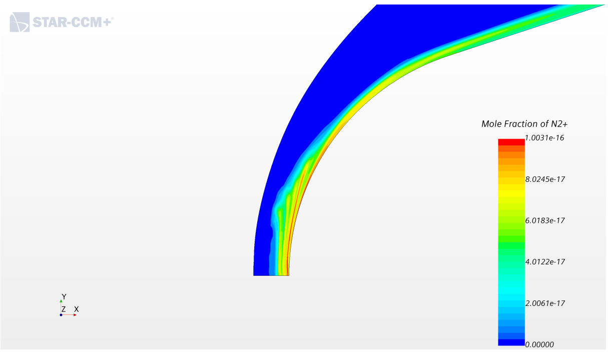

Figure 5.21: N_2^+ mole fraction distribution

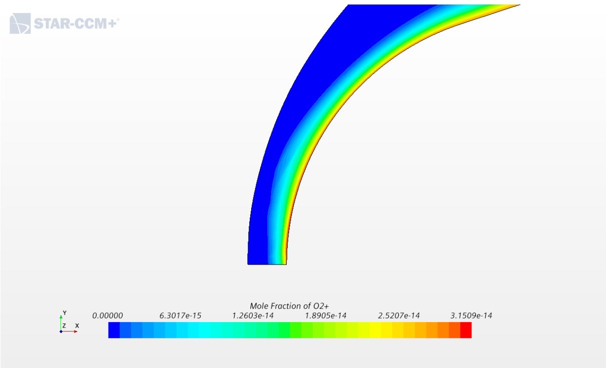

Figure 5.22: O_2^+ mole fraction distribution

5.3 Benchmark Analysis

This section is committed to the verification of the model previously implemented in Siemens STAR-CCM+. The assessment is obtained through the analysis of a hypersonic air flow around a sphere of radius $0.5\,m$. The study aims not only at verifying the model applied, but at set the limits of STAR-CCM+ in modeling and computing hypersonic flows and aerothermo-chemical processes. Few investigation concerning hypersonic phenomena (obtained by STAR-CCM+) are available in literature, therefore this is a first step to understand whether the solution in output is consistent with reliable results or not. The reference results have been obtained by a calculation code developed by the Supervisor of this thesis years ago. A comparison between the solution by STAR-CMM+ and the baseline model will be detailed[16], specifying the boundary conditions and the properties of the grid. The data for reactions and rate constants adopted in the analysis are contained in Appendix A.

5.3.1 Grid and Boundary conditions

The computational domain has been design to enclose the bow shock around the sphere. In particular, it has been modeled considering the inflow boundary as an arc of radius of $0.911\,m$ which surrounds a quarter of a circle of radius of $0.5\,m$. The directed grid presents the following properties:

- 76x76 cells;
- a constant distribution along the axis direction;
- one side geometric spacing distribution along the tangent direction at wall with a spacing at start equal to $0.005\,m$;

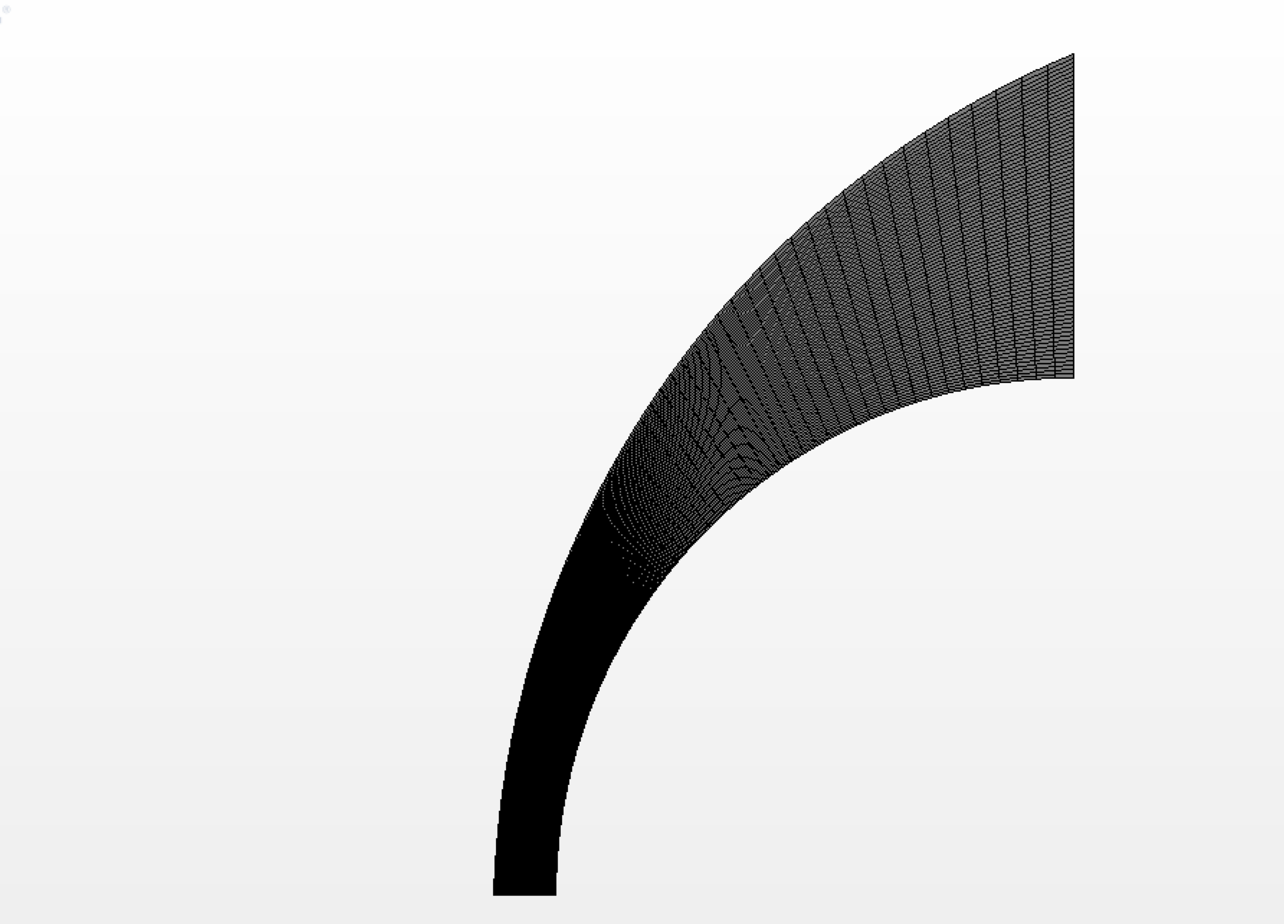

Figure 5.23: Computational domain and grid for a sphere of radius $0.5\,m$

As it has been previously done, the contour of the computational domain has been split into four parts: inflow, outflow, wall and axis. As regards the free stream conditions for the inflow and outflow boundaries, the air flow is characterized by:

- a Mach number $M = 19$;
- a temperature $T = 235\,K$;
- a pressure $p = 9.9\,Pa$;
- Molecular oxygen mass fraction $Y_{O2} = 0.233$;
- Molecular nitrogen mass fraction $Y_{N2} = 0.767$;

Meanwhile at wall and on the axis, the same condition for the HCM have been set, except for the emissivity and reflectivity coefficients which are respectively 0.85 and 0.15.

5.3.2 Results

This paragraph shows the numerical results of the investigation compared with the baseline model. Observing the figures 5.24-5.26 it is clear that the distributions of the thermodynamic variables in output by STAR-CCM+ are quite different from the benchmark results. Although pressure reaches values similar to the baseline model downstream of the bow-shock, all thermodynamic properties present not negligible differences in the stand off distance. The results obtained by STAR-CCM+ present, in fact, values of density higher than the baseline model and, consequently, a reduced stand off distance(a distance of 3 cm compared to the 4 cm of the reference model). The reduced stand-off distance is indicative of a more intense thermo-chemical activity than the benchmark values, which is occurring downstream of the bow-shock. Other substantial dissimilarity can be noticed in the region between the shock-wave and the wall. The solution presents a wide region where the distributions are approximately flat, compared with the increasing density and the descending temperature of the baseline model.

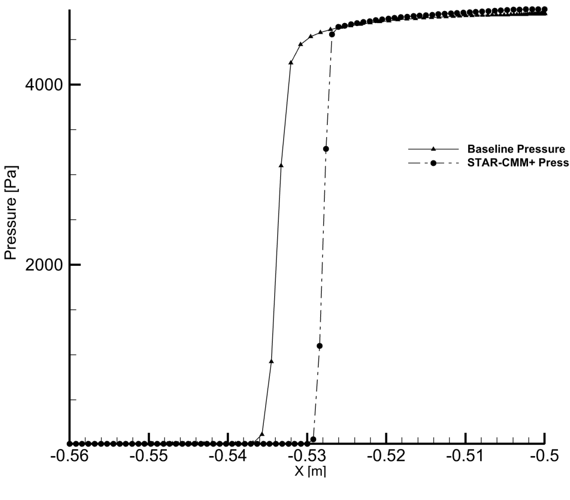

Figure 5.24: Pressure distribution along the axis

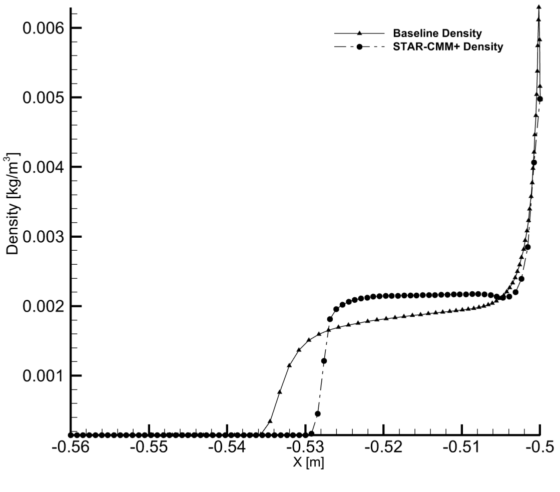

Figure 5.25: Density distribution along the axis

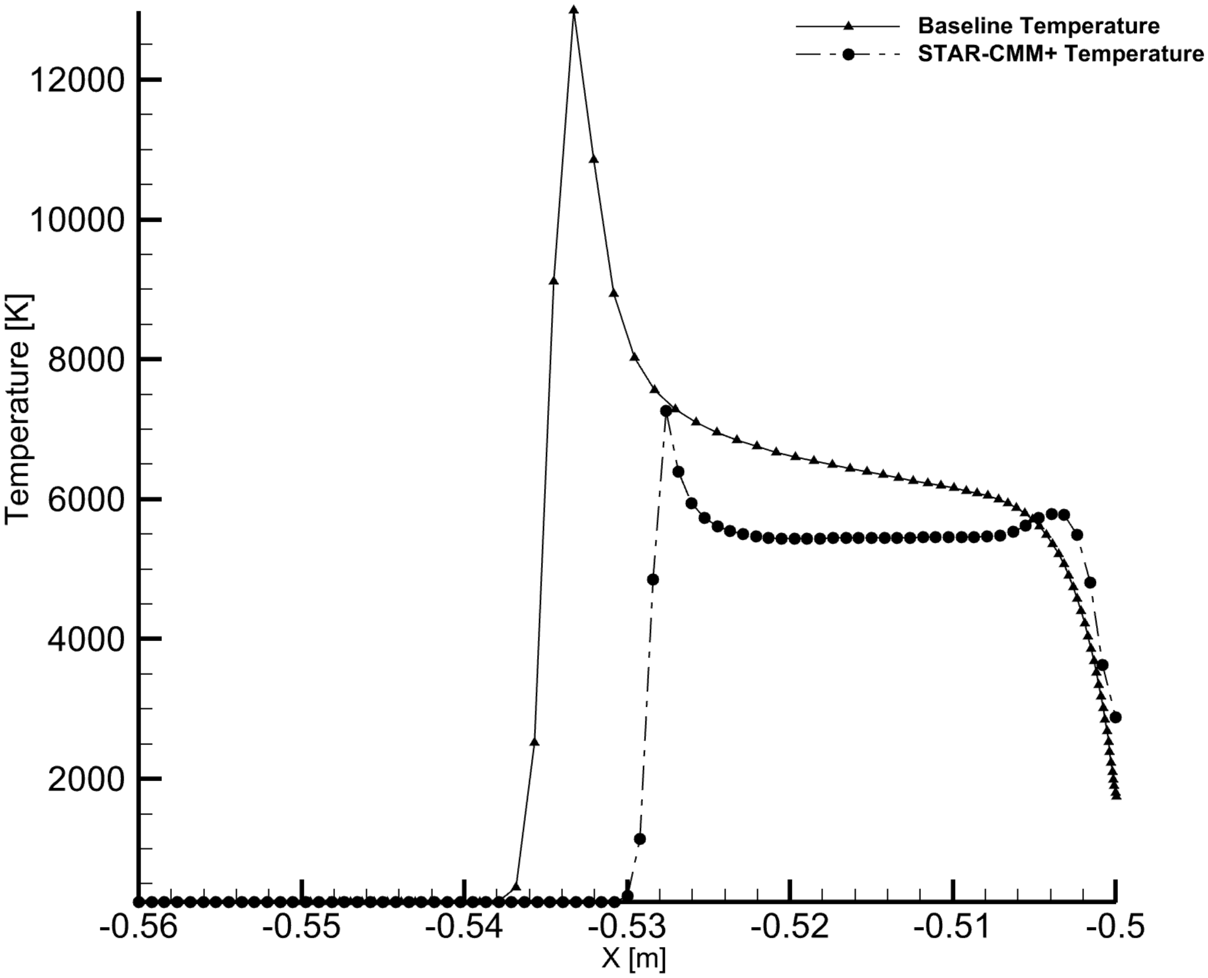

Figure 5.26: Temperature distribution along the axis

A similar condition can be observed in figure 5.27. The mass fractions present a quite flat distribution downstream of the shock-wave respect to the baseline model, indicative of a chemical equilibrium condition reached in that area. However, even if the trends are not similar, the orders of magnitude of the mass fractions are very comparable. The results of the investigations present a higher dissociation of molecular nitrogen than the benchmark values and, consequently, lower temperatures. The mass fraction of the molecular oxygen well approaches to the more reliable model, dissociating almost completely. As regards the region close to the wall, the recombination of N_2 makes its distribution more pronounced meanwhile, the mass fraction of atomic oxygen decreases. This latter is the cause of a second peak in the distribution of temperature, an higher temperature at wall (1800 respect to the benchmark value of $1700K$) and formation of NO and O_2, unpredicted by the reference model. The post-shock area, as it can be observed, is the region with the most evident dissimilarities. The mass fraction of the nitric oxide is completely absent and the maximum value of temperature is far below the one expected in the post-shock region.

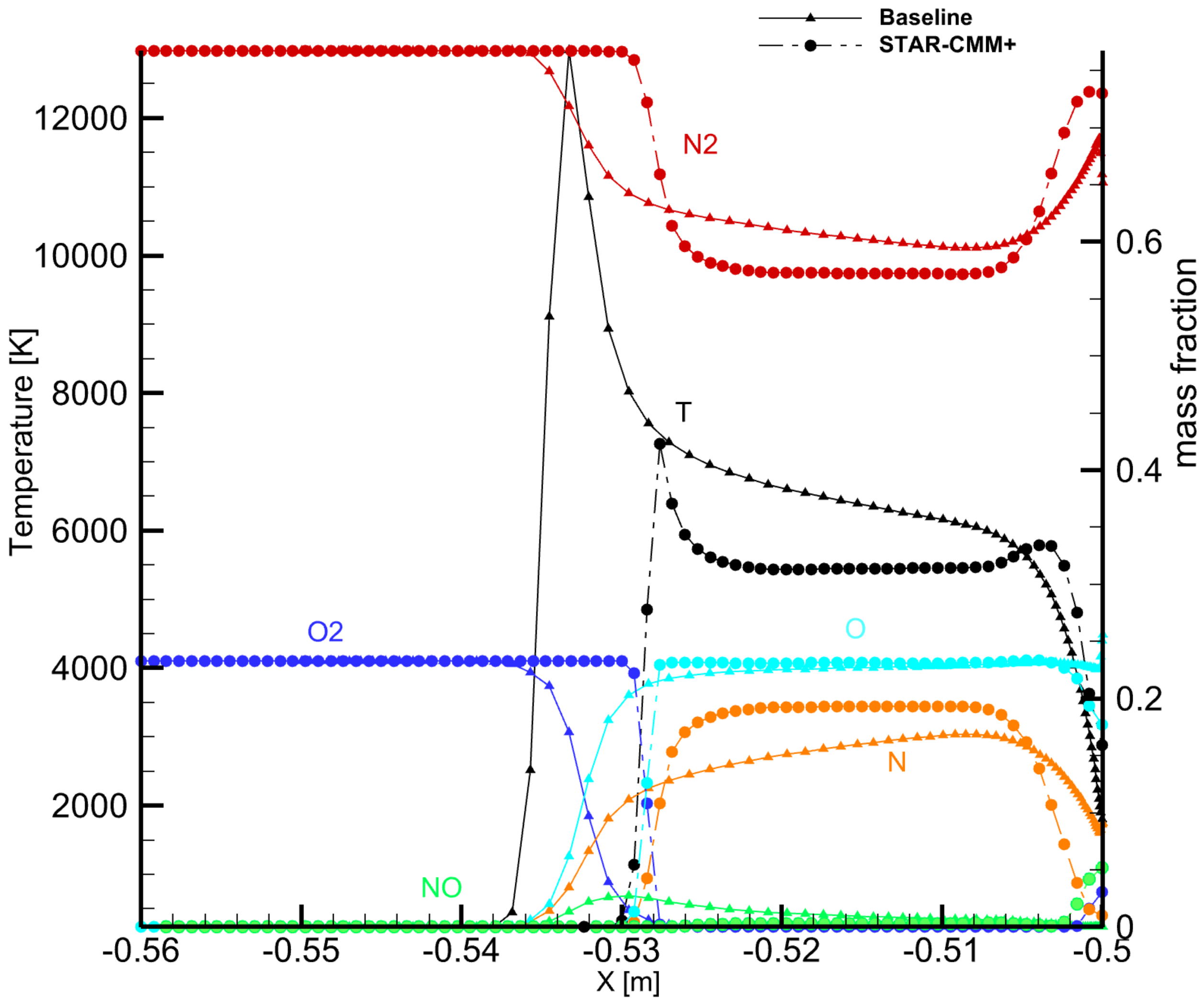

Figure 5.27: Distribution of mass fractions of the non-ionized species along the axis

Figure 5.28 shows the distribution of the mole fraction of the ionized species downstream of the bow-shock. Since the mole fractions of the charged particles are minimal, a logarithmic scale has been set to compare the orders of magnitude of the results by STAR-CCM+ with the baseline model. Although the trend are highly comparable, $N+$, N_2^+ and $O+$ mole fractions distribution present lower values than expected. The orders of magnitude of $NO+$ and $e-$ mole fractions instead, are consistent with the pattern. The concentration of O_2^+ presents values lower than the ones of the baseline model, although the trend may be acceptable since the mole fraction increases along the axis. The distribution of N_2^+ mole fraction presents an oscillation close to the wall, caused by the numerical scheme. However all the distributions, as well as the non-ionized species case, are characterized by dissimilarities in the post-shock area.

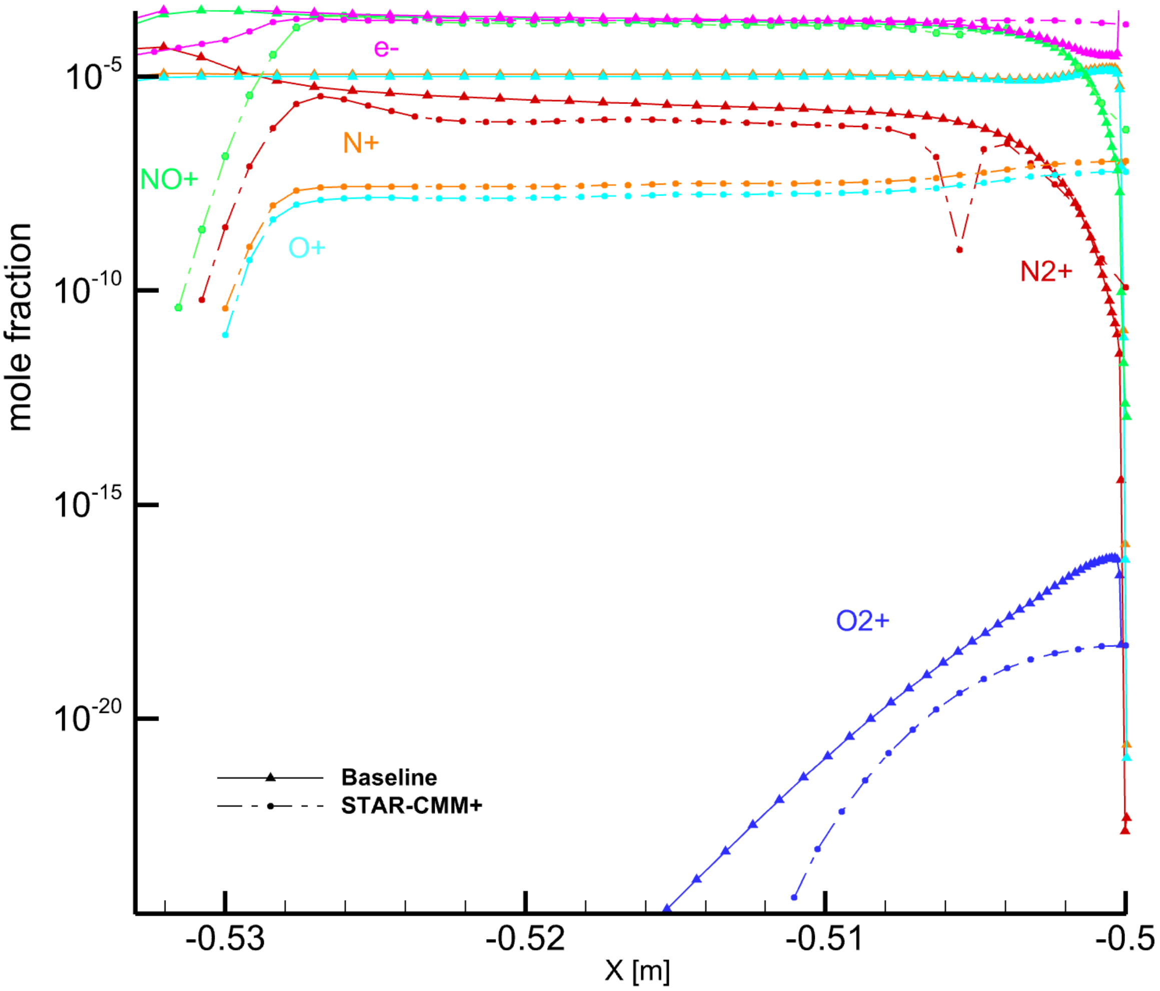

Figure 5.28: Distribution of mole fractions of the ionized species along the axis

All the discrepancies previously described, can be justified pointing out two fundamental aspects in the implemented model. First, the thermodynamic data inserted in the software(see Appendix A) cover a range of temperatures which extends up to 6000 K, lower value than the ones reached in the flow field. This limited range can strongly affect the computing of equilibrium constants and the backward reaction rates in STAR-CCM+. The software in fact, computes the equilibrium constants as follow:

$$K_p = e^{-\sum_i v_i \frac{G_i^{p=1}}{RT}} \tag{5.3}$$

where $G_i^{p=1}$ is the Gibbs free energy of each species in the reaction evaluated at 1 atmosphere pressure. It is defined as:

$$G_i = H_i - TS_i \tag{5.4}$$

Therefore, the chemical equilibrium constants (and consequently the backward reaction rates) are strongly affected by the functions H/RT and S/RT which have been approximated within a limited range of temperatures, far below the effective values which come out in the flow field. The second aspect to take into account is the limit of the developed model in describing non-equilibrium energetic phenomena. The figure 5.29 shows the distribution of vibrational temperatures along the axis in the baseline model. It is immediately possible to notice that all vibrational temperatures in the post-shock area are far from the equilibrium condition since they do not coincide with the roto-translational temperature (black curve). The post-shock region is, therefore, characterized by lower vibrational energies and consequently higher roto-translational temperature. The results provided by the developed model in STAR-CCM+, instead, presents a vibrational equilibrium reached instantly in the post-shock region, since the peak temperature is far below the value of the baseline model.

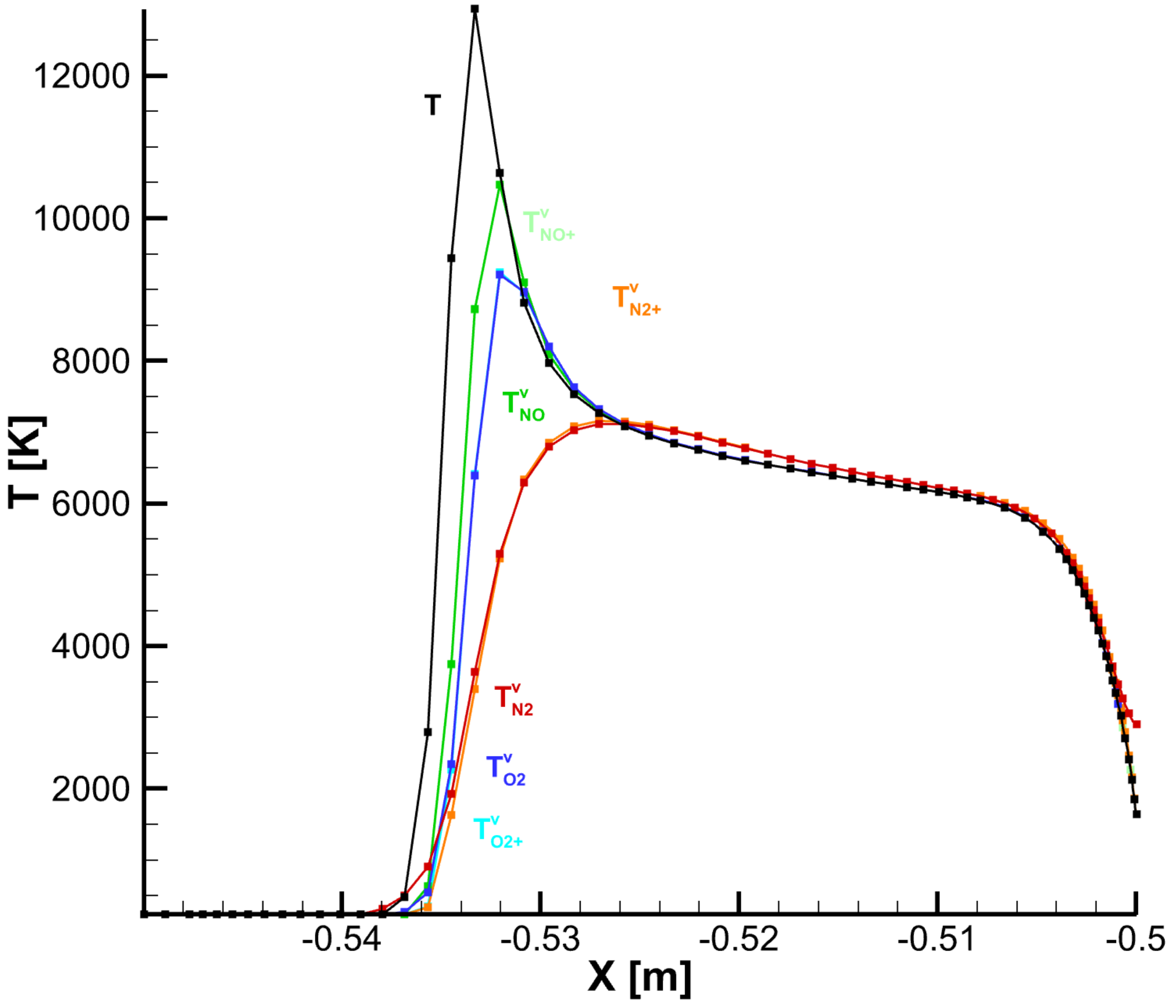

Figure 5.29: Distribution of vibrational temperatures along the axis

5.3.3 Later Developed Model

Later, it has been understood how to to model non-equilibrium energetic phenomena in STAR-CCM+ by adopting the Thermal Non-equilibrium model. This particular model allows to consider variations of internal energy of each species, due to its electronic and vibrational parts(for biatomic species). This is accomplished by considering the specific heats as "fully excited"(as in the reference model) which means that their roto-translational contribute is set as:

$$(C_{pi})_{R-T} = \frac{3}{2}RT + RT \qquad for\, biatomic\, species \tag{5.5}$$

$$(C_{pi})_{r-t} = \frac{3}{2}RT \qquad for\, monoatomic\, species \tag{5.6}$$

and the vibrational and electronic contributes are obtained by differencing:

$$(C_{pi})_{v-e} = (C_{pi})_{tot} - (C_{pi})_{r-t} \tag{5.7}$$

Furthermore, an important difference, respect to the previous developed model, is the possibility to specify other properties of the single species. Those of particular interest are:

- the vibrational temperature (which allows to evaluate the correspondent vibrational energy);
- the relaxation time required to reach the equilibrium condition;
- the standard state temperature;
- the heat of formation;

The inclusion of these data, equal to the benchmark model (except for the relaxation time), guarantees a better management of the vibrational non-equilibrium condition in the software. Furthermore the range of temperature have been extended to $15000K$ by using the model in [105] . Observing the figure 5.30 it is evident how the non-equilibrium condition affects the temperature in the post-shock area. The results obtained by STAR-CCM+ present values of temperature much more similar to the baseline model. The peak in the distribution of temperature, in fact, assumes values predicted by the benchmark results. However, the stand-off distance is still lower than expected, indicative of a more intense thermo-chemical activity downstream of the bow-shock.

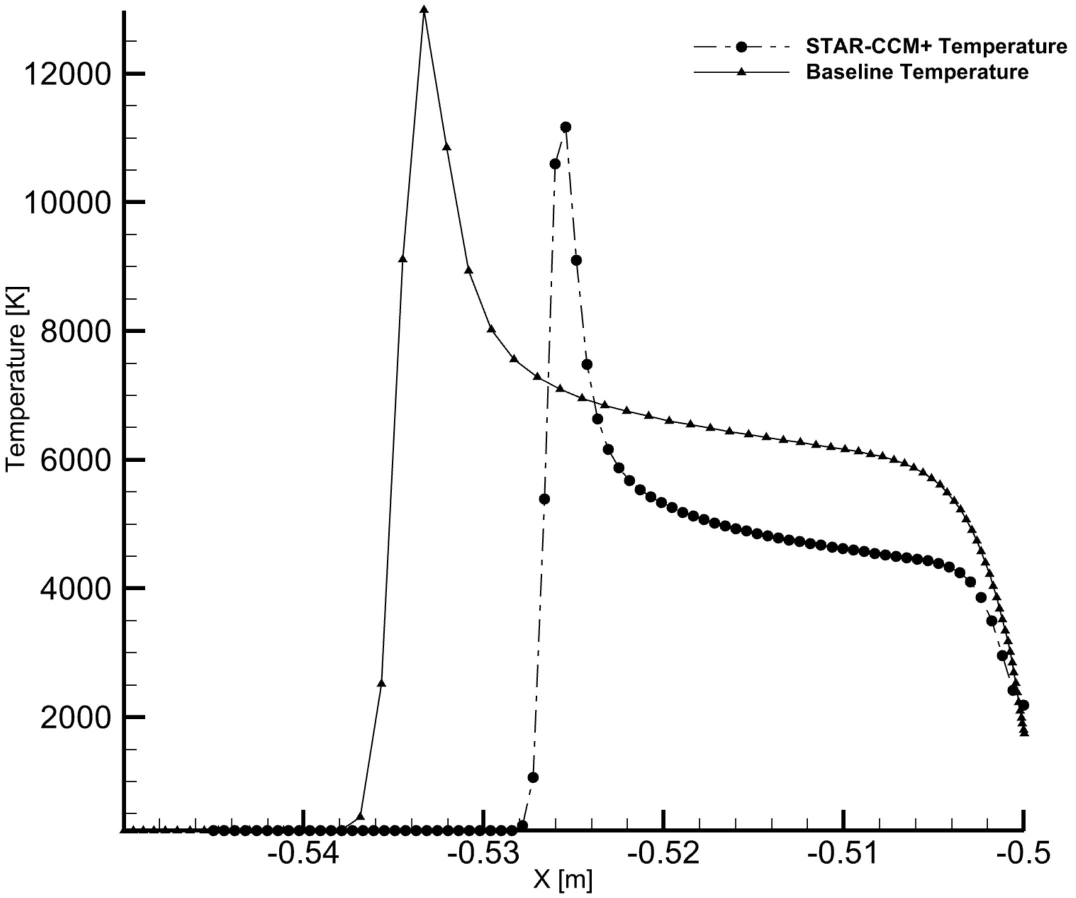

Figure 5.30: Distribution of temperature along the axis

Figure 5.31 points out this effect. Mass fraction of N_2 downstream of the shock-wave still remains below the reference values (equivalently, increased mass fraction of N) due to an excessive dissociation. However, the extremely rapid recombination of molecular nitrogen and molecular oxygen close to wall, which was present in the previous model, has disappeared. Consequently, the unexpected second peak of temperature shown in figure 5.16 goes missing. The distribution of mass fraction of NO still exhibits a quite flat trend respect to the benchmark results, but, as well as O_2 and N_2, its recombination at wall has been mitigated.

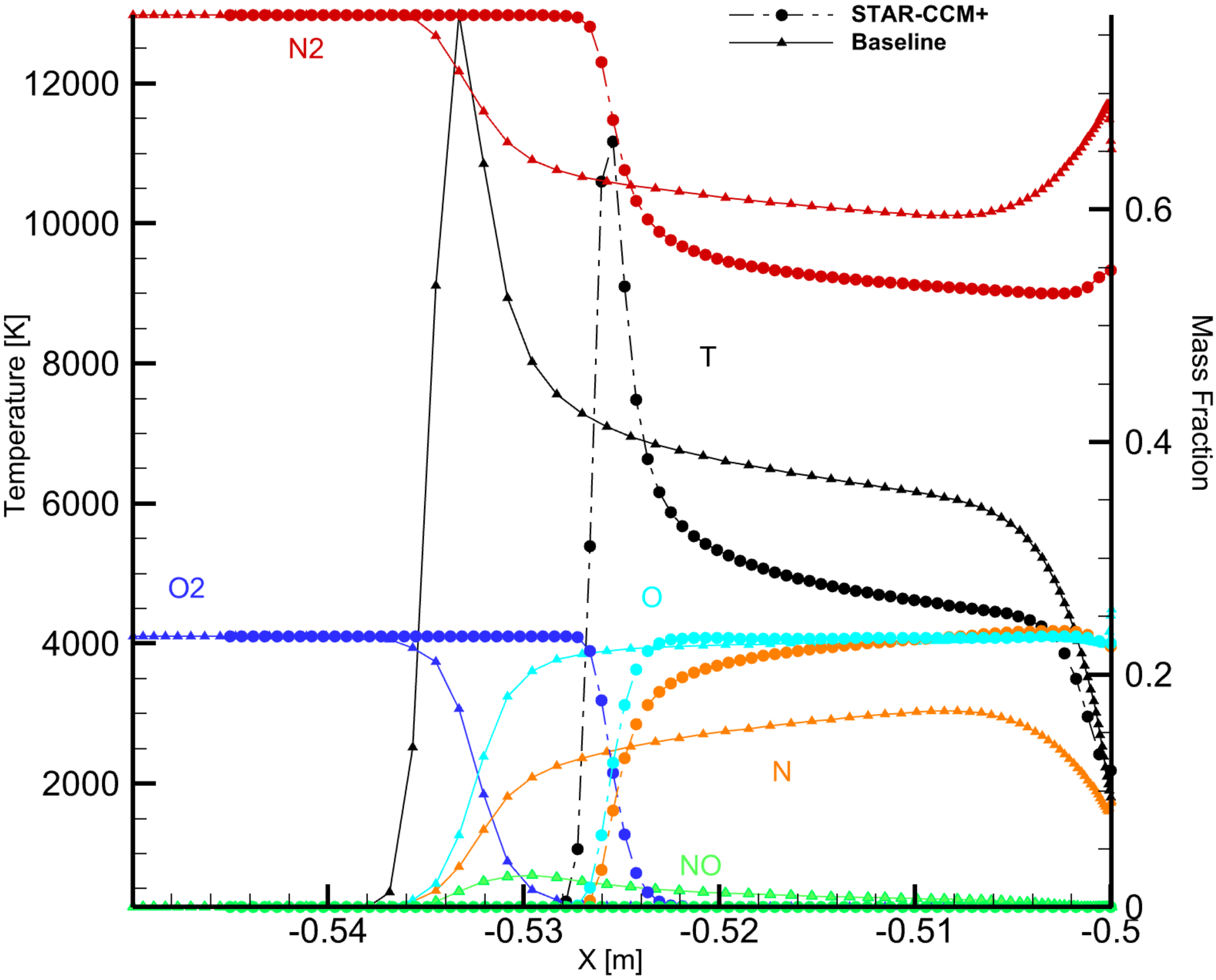

Figure 5.31: Distribution of mole fractions of the neutral species along the axis

Ionized species are not well described by the new model developed. As it can be observed in the figure 5.32, also the mole fractions N_2^+, e^- and NO^+ present different values respect to the baseline model. However the mole fraction distribution of N^2+ is sufficiently smooth and free from oscillations. Nevertheless, both results obtained by STAR-CCM+ contain a non negligible amount of electrons upstream of the shock-wave. This phenomenon is essentially due to the limits of the diffusive model considered. The implemented transport mechanisms in fact, do not take into account the ambipolar diffusion and the need to reach a quasineutrality condition in the flow field. Consequently, electrons also diffuse in the region upstream of the shock-wave as if they were neutral species.

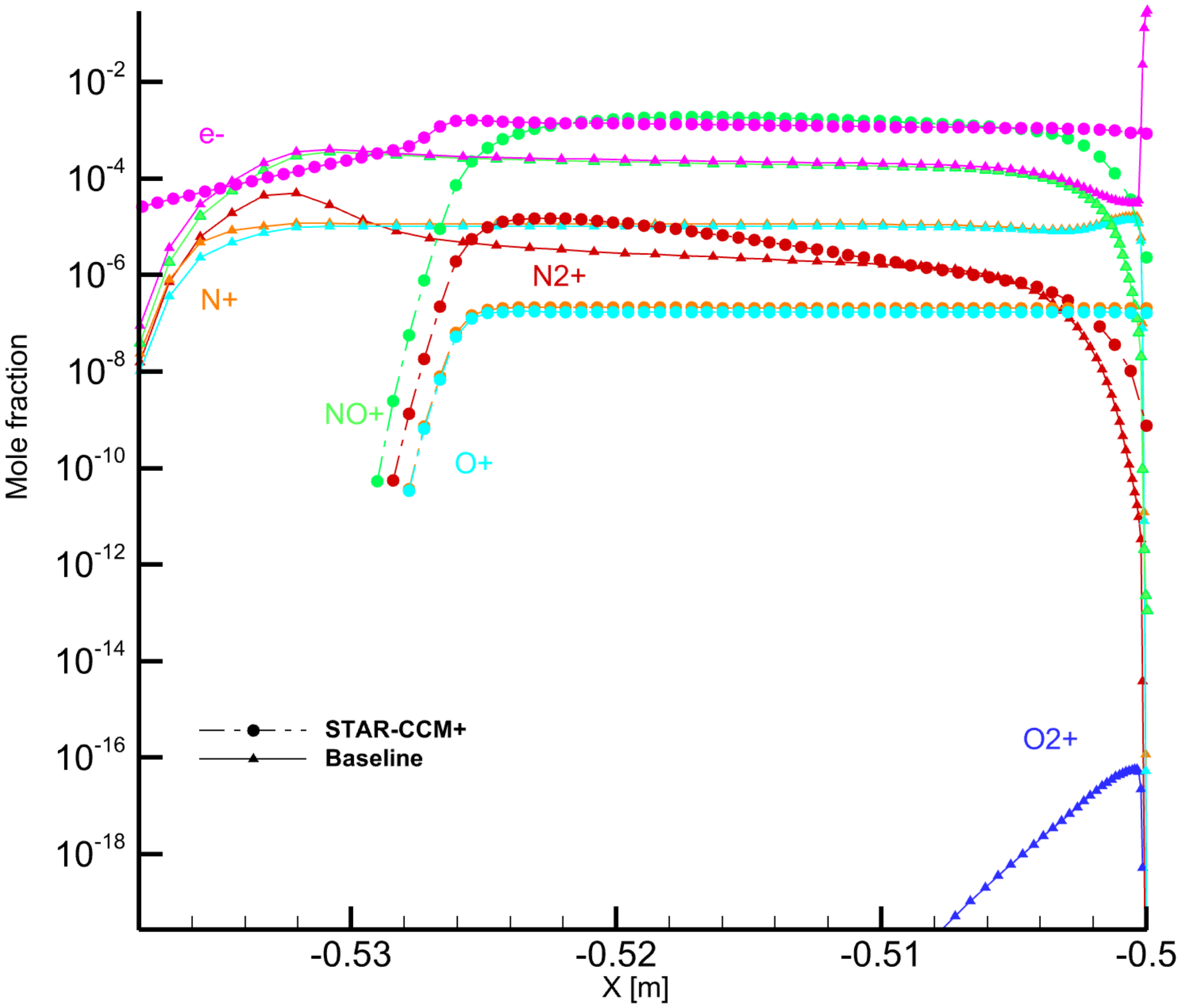

Figure 5.32: Distribution of mole fractions of the charged species along the axis

Despite the properties of the new developed model, another reason which may justify the differences with the baseline results, can be found in the vibrational non-equilibrium condition and its impact on the rate constants. Biatomic species, far from the vibrational equilibrium condition in the post-shock region, see low levels of vibrational energy and a certain time (and number of collisions) is required to increase their energy up to the equilibrium value. In this state, the probability for the dissociation to occur, is lower than the one for a particle in vibrational equilibrium condition,since the higher energetic level of the latter (see figure 5.29). This phenomenon strongly influences the rate constants and slows down the dissociation reactions. Therefore, the cause of the higher slope of the mass fraction distribution of N, in the post-shock region, may be justified with this phenomenon. Although the several models available in literature[16], STAR-CCM+, at least in the last investigation, doesn't allow to take into account the influence of the vibrational non-equilibrium on the rate constants. Furthermore, it is not clear how the relaxation times are evaluated in STAR-CCM+, therefore there may be differences with the ones used in the reference model. In addition, although the range of temperature has been extended, it is not possible to evaluate the equilibrium constants computed by STAR-CCM+ to quantify the differences with the ones inserted in the benchmark model.

5.4 Discussion

As it has been observed at the beginning of this chapter, the results of the analysis of the flow field around the HCM reveal moderate high-temperature effects. The Mach number of the free stream, combined with the conditions of temperature and pressure at that altitude, is such to generate not high enough temperatures to observe intense chemical phenomena downstream of the shock-wave . For this reason, only the dissociation of molecular oxygen and few formation of NO are remarkable phenomena in this area. As regards the charged species, a very small amounts of electrons and NO^+ are observable due to the ionization of the nitric oxide at these relatively low temperatures. However, as expected, the occurrence of these chemical processes has strongly affected the thermodynamic properties of the flow field. The benchmark analysis has shown the limits of the implemented model for the analysis of the air flow surrounding the HCM. In particular, the computational model doesn't take into account the vibrational non-equilibrium effects in the post-shock region, which affect the maximum temperature values and the rate constants. As regards the differences in the results of the benchmark analysis, several elements must be taken into account. First of all, the equilibrium constants computed by STAR-CCM+ (see equations (5.3) and (5.4)) may be different from the ones inserted in the reference model. This can explain the differences in the distributions of concentration which occur downstream of the shock-wave. Furthermore, although the vibrational non-equilibrium is inserted in the later model implemented in STAR-CCM+, its impact on the constant rates is not considered by the software and it is not clear how the relaxation times are computed. Finally, mechanisms of diffusion of the benchmark analysis are quite different from the reference model. In particular the ambipolar diffusion is not considered, therefore a not negligible concentrations of electrons is evident upstream of the shockwave.

Chapter 6

Conclusions and Future Work

In this work, a computational model has been developed by the commercial software Siemens STAR-CCM+ to analyze a flow field around the nose of a hypersonic cruise missile. The air flow has been modeled as a reacting gas mixture composed of eleven species. Data about reactions and thermodynamic properties have been inserted through CHEMKIN files, specifying rate constants of each reaction, according to the Arrhenius equation, and approximating specific heats, enthalpy and entropy, associated to each species, with 7-coefficients NASA thermodynamic polynomials. Furthermore, diffusion mechanisms have been implemented in the investigation, since the multi-component model adopted, taking into account binary diffusion and gradients of temperature effects. The Finite Volume Method has been adopted to obtain the numerical solution of the steady state analysis, using an implicit scheme for time discretization. The Pre-conditionated Biconjugated Gradient Stabilized method is the iterative procedure adopted, coupled with the Algebraic Multigrid technique, to solve the system obtained by the discretization. Finally the results have been verified through a benchmark analysis. Although high temperature effects are evident in the flow field, results show limits in STAR-CCM+ to model non-equilibrium conditions. In particular, the effects of the vibrational non-equilibrium on the reaction rates are apparently not considered in the software, showing quite different results respect to the benchmark data, above all in the post-shock region. Moreover, it is not clear how to evaluate the vibrational relaxation times and the equilibrium constants computed by the software. However the orders of magnitude and the trends predicted for the concentration of the neutral species are very similar to the reference model. Future work may consider a higher range of temperatures for the NASA polynomials to study flow fields with higher Mach numbers, or the implementation of a vibrational non-equilibrium model which takes into account all the related phenomena. Furthermore, it would be worthwhile to develop a new model which includes plasma correlated phenomena and ambipolar diffusion, and observe whether the distribution of concentration of the charged species is evaluated properly or not. Finally, it would be interesting to analyze the flow field generated by a HGV.

Appendix A

Thermo-chemical data

CHEMKIN files have been used to import thermo-chemical data of eleven species into the commercial sotware STAR-CCM+. Two distinct files have been imported to study the flow field around the HCM. The first file contains information about chemical species, reactions which occur and constant rates, while the second file coefficients to approximate thermodynamic functions of each species.

A.1 CHEMKIN Chemical Input File

The firts input file is structured in three blocks in the following order:

1. Elements block which lists all the elements contained in the species to be considered;
2. Species block which lists all the atom and molecules in the model;
3. Reaction block which lists reaction equations with rate parameters for each reaction.

The forward rate constants specified are calculated by the Arrhenius equation:

$$k_f = AT^{\beta}e^{-\frac{E_a}{RT}} \tag{A.1}$$

The parameters A, β and E_a are specified in this order, next to each reaction, and separated by spaces. In the top line of the Reactions block there are two keywords specifying units for the activation energy ($J/KMOL$). Pre-exponential factor is expressed in $cm^3/s\,mol$. For reactions which include third body (identified in the file by symbol M), a constant rate enhancement factor is specified. Depending on the third body, the rate constant is obtained by multiplying by the corresponding enhancement factor. STAR-CMM+ requires factors to be multiplied by 10^3 [106]. The reactions implemented in the software are:

$$N_2 + M \leftrightarrow N + N + M \tag{A.2}$$

$$O_2 + M \leftrightarrow O + O + M \tag{A.3}$$

$$NO + M \leftrightarrow N + O + M \tag{A.4}$$

$$N_2 + O \leftrightarrow NO + N \tag{A.5}$$

$$NO + O \leftrightarrow N + O_2 \tag{A.6}$$

$$e^- + N_2 \leftrightarrow e^- + 2N \tag{A.7}$$

$$e^- + O \leftrightarrow O^+ + 2e^- \tag{A.8}$$

$$e^- + N \leftrightarrow N^+ + 2e^- \tag{A.9}$$

$$N + N \leftrightarrow N_2^+ + e^- \tag{A.10}$$

$$O + O \leftrightarrow O_2^+ + e^- \tag{A.11}$$

$$NO^+ + O \leftrightarrow N^+ + O_2 \tag{A.12}$$

$$N^+ + N_2 \leftrightarrow N_2^+ + N \tag{A.13}$$

$$O_2^+ + N \leftrightarrow N^+ + O_2 \tag{A.14}$$

$$O_2^+ + N_2 \leftrightarrow N_2^+ + O_2 \tag{A.15}$$

$$O_2 + O \leftrightarrow O^+ + O_2 \tag{A.16}$$

$$NO^+ + N \leftrightarrow O^+ + N_2 \tag{A.17}$$

$$NO^+ + O_2 \leftrightarrow O_2^+ + NO \tag{A.18}$$

$$NO^+ + O \leftrightarrow O_2^+ + N \tag{A.19}$$

$$O^+ + N_2 \leftrightarrow N_2^+ + O \tag{A.20}$$

$$NO^+ + N \leftrightarrow N_2^+ + O \tag{A.21}$$

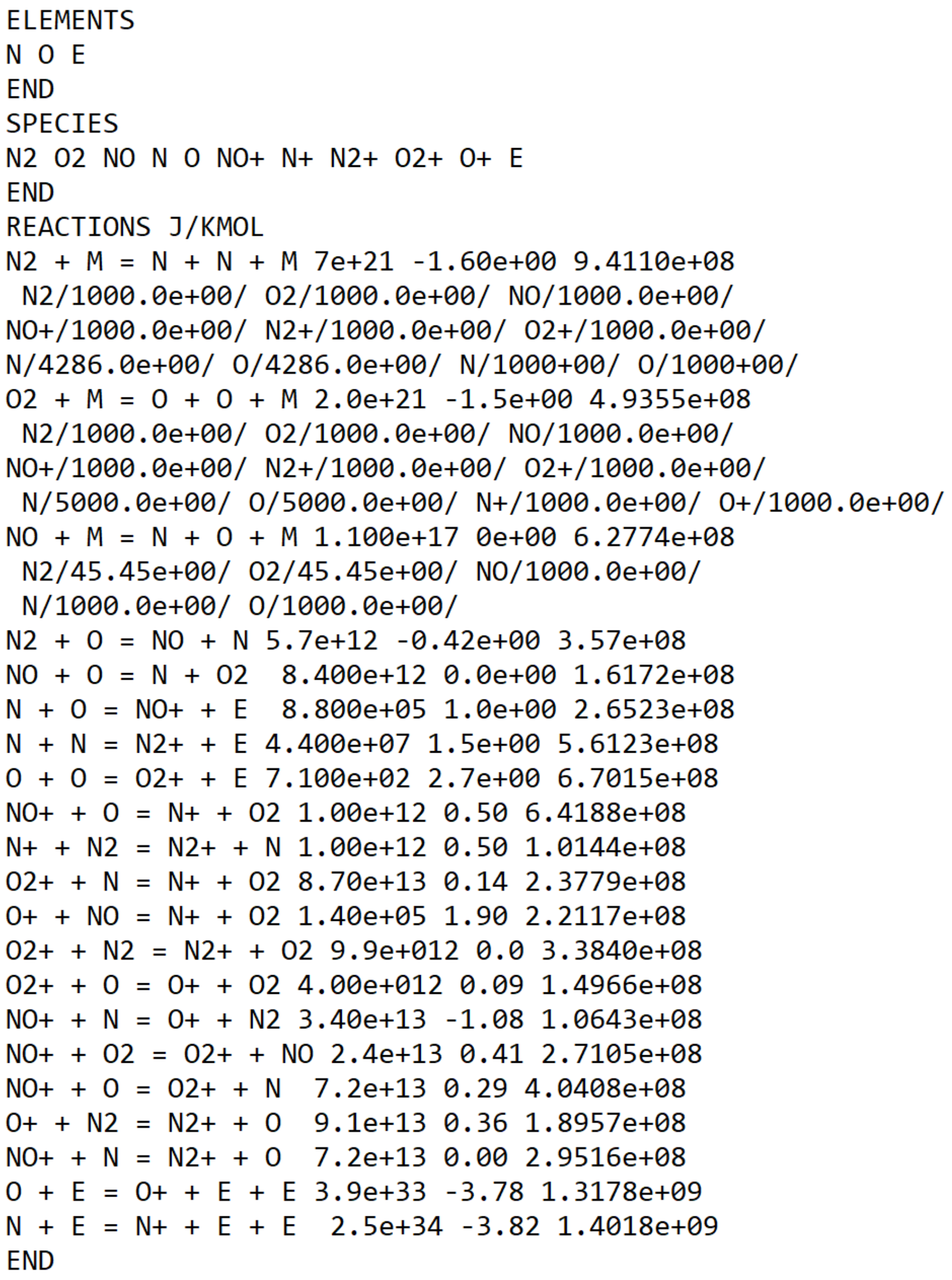

```
ELEMENTS
N O E
END
SPECIES
N2 O2 NO N O NO+ N+ N2+ O2+ O+ E
END
REACTIONS J/KMOL
N2 + M = N + N + M 7e+21 -1.60e+00 9.4110e+08
 N2/1000.0e+00/ O2/1000.0e+00/ NO/1000.0e+00/
NO+/1000.0e+00/ N2+/1000.0e+00/ O2+/1000.0e+00/
N/4286.0e+00/ O/4286.0e+00/ N/1000+00/ O/1000+00/
O2 + M = O + O + M 2.0e+21 -1.5e+00 4.9355e+08
 N2/1000.0e+00/ O2/1000.0e+00/ NO/1000.0e+00/
NO+/1000.0e+00/ N2+/1000.0e+00/ O2+/1000.0e+00/
 N/5000.0e+00/ O/5000.0e+00/ N+/1000.0e+00/ O+/1000.0e+00/
NO + M = N + O + M 1.100e+17 0e+00 6.2774e+08
 N2/45.45e+00/ O2/45.45e+00/ NO/1000.0e+00/
 N/1000.0e+00/ O/1000.0e+00/
N2 + O = NO + N 5.7e+12 -0.42e+00 3.57e+08
NO + O = N + O2  8.400e+12 0.0e+00 1.6172e+08
N + O = NO+ + E  8.800e+05 1.0e+00 2.6523e+08
N + N = N2+ + E 4.400e+07 1.5e+00 5.6123e+08
O + O = O2+ + E 7.100e+02 2.7e+00 6.7015e+08
NO+ + O = N+ + O2 1.00e+12 0.50 6.4188e+08
N+ + N2 = N2+ + N 1.00e+12 0.50 1.0144e+08
O2+ + N = N+ + O2 8.70e+13 0.14 2.3779e+08
O+ + NO = N+ + O2 1.40e+05 1.90 2.2117e+08
O2+ + N2 = N2+ + O2 9.9e+012 0.0 3.3840e+08
O2+ + O = O+ + O2 4.00e+012 0.09 1.4966e+08
NO+ + N = O+ + N2 3.40e+13 -1.08 1.0643e+08
NO+ + O2 = O2+ + NO 2.4e+13 0.41 2.7105e+08
NO+ + O = O2+ + N  7.2e+13 0.29 4.0408e+08
O+ + N2 = N2+ + O  9.1e+13 0.36 1.8957e+08
NO+ + N = N2+ + O  7.2e+13 0.00 2.9516e+08
O + E = O+ + E + E 3.9e+33 -3.78 1.3178e+09
N + E = N+ + E + E  2.5e+34 -3.82 1.4018e+09
END
```

Figure A.1: CHEMKIN Chemical Reactions file[14]

A.2 CHEMKIN Thermodynamic Data File

The second input file contains coefficients needed to represent thermodynamic functions with NASA polynomials[107]:

$$\frac{c_p}{R} = a_1 + a_2T + a_3T^2 + a_4T^3 + a_5T^4 \tag{A.22}$$

$$\frac{H^\circ}{RT} = a_1 + a_2T + a_3T^2 + a_4T^3 + a_5T^4 + \frac{a_6}{T} \tag{A.23}$$

$$\frac{s}{RT} = a_1lnT + a_2T + a_3^2 + a_4T^3 + a_5T^4 + a_7 \tag{A.24}$$

For each species there is a line which specifies sequentially:

- species name;
- data (not always specified);
- Atomic symbols and formula;
- phase of species;
- low temperature;
- high temperature;
- common temperature;

Low, high and common temperature describe two temperature ranges. This means that for each species 14 coefficients will be specified. The thermodynamic data consist of a_1,a_2,...,a_7 for high temperature range and a_8,a_9,...a_{14} for low temperature range. The coefficients are specified just below each species description.

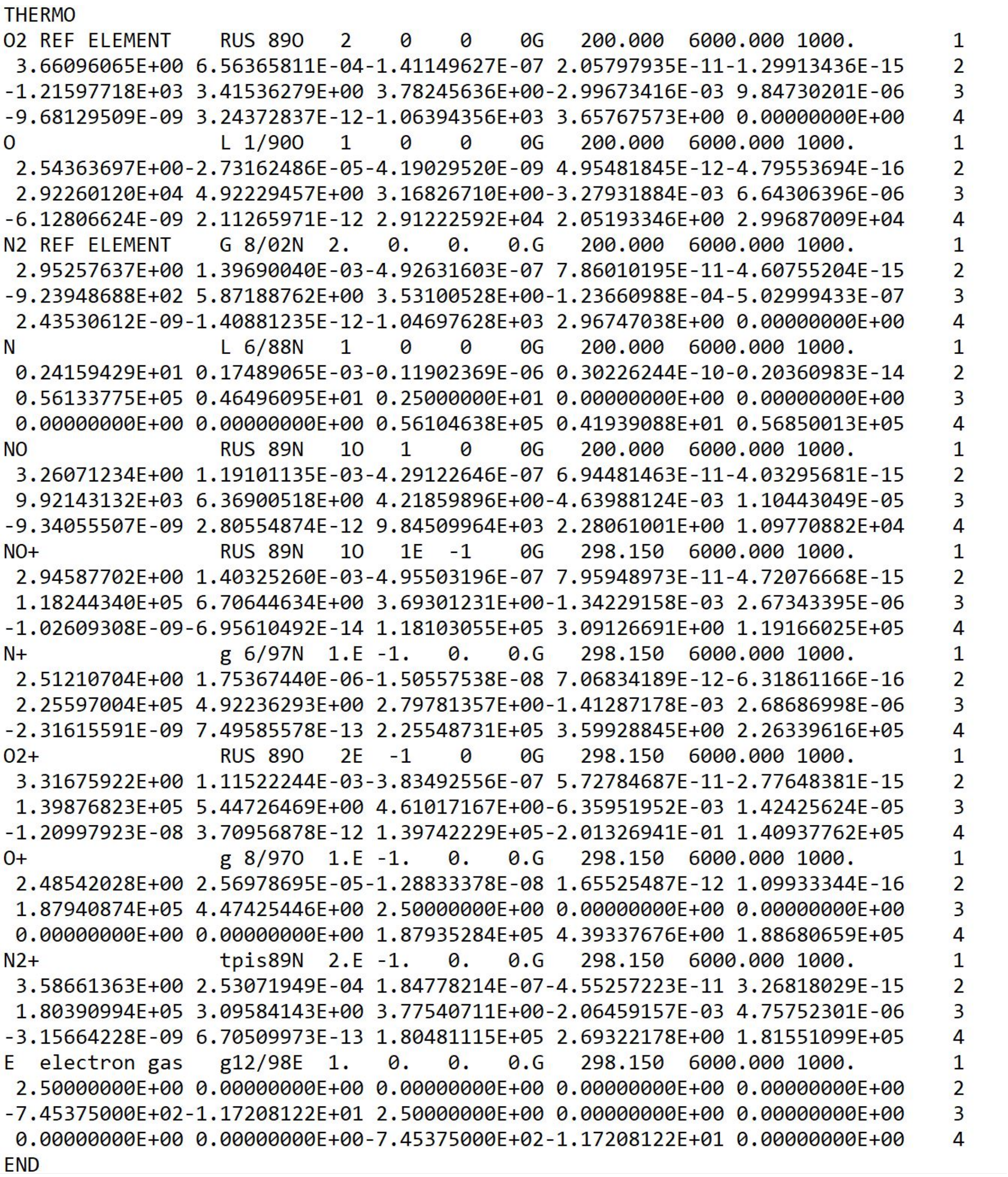

```
THERMO
O2 REF ELEMENT    RUS 89O   2    0    0    0G   200.000  6000.000 1000.        1
 3.66096065E+00 6.56365811E-04-1.41149627E-07 2.05797935E-11-1.29913436E-15    2
-1.21597718E+03 3.41536279E+00 3.78245636E+00-2.99673416E-03 9.84730201E-06    3
-9.68129509E-09 3.24372837E-12-1.06394356E+03 3.65767573E+00 0.00000000E+00    4
O                 L 1/90O   1    0    0    0G   200.000  6000.000 1000.        1
 2.54363697E+00-2.73162486E-05-4.19029520E-09 4.95481845E-12-4.79553694E-16    2
 2.92260120E+04 4.92229457E+00 3.16826710E+00-3.27931884E-03 6.64306396E-06    3
-6.12806624E-09 2.11265971E-12 2.91222592E+04 2.05193346E+00 2.99687009E+04    4
N2 REF ELEMENT    G 8/02N  2.   0.   0.   0.G   200.000  6000.000 1000.        1
 2.95257637E+00 1.39690040E-03-4.92631603E-07 7.86010195E-11-4.60755204E-15    2
-9.23948688E+02 5.87188762E+00 3.53100528E+00-1.23660988E-04-5.02999433E-07    3
 2.43530612E-09-1.40881235E-12-1.04697628E+03 2.96747038E+00 0.00000000E+00    4
N                 L 6/88N   1    0    0    0G   200.000  6000.000 1000.        1
 0.24159429E+01 0.17489065E-03-0.11902369E-06 0.30226244E-10-0.20360983E-14    2
 0.56133775E+05 0.46496095E+01 0.25000000E+01 0.00000000E+00 0.00000000E+00    3
 0.00000000E+00 0.00000000E+00 0.56104638E+05 0.41939088E+01 0.56850013E+05    4
NO                RUS 89N  1O    1    0    0G   200.000  6000.000 1000.        1
 3.26071234E+00 1.19101135E-03-4.29122646E-07 6.94481463E-11-4.03295681E-15    2
 9.92143132E+03 6.36900518E+00 4.21859896E+00-4.63988124E-03 1.10443049E-05    3
-9.34055507E-09 2.80554874E-12 9.84509964E+03 2.28061001E+00 1.09770882E+04    4
NO+               RUS 89N  1O   1E  -1    0G   298.150  6000.000 1000.        1
 2.94587702E+00 1.40325260E-03-4.95503196E-07 7.95948973E-11-4.72076668E-15    2
 1.18244340E+05 6.70644634E+00 3.69301231E+00-1.34229158E-03 2.67343395E-06    3
-1.02609308E-09-6.95610492E-14 1.18103055E+05 3.09126691E+00 1.19166025E+05    4
N+                g 6/97N  1.E -1.   0.   0.G   298.150  6000.000 1000.        1
 2.51210704E+00 1.75367440E-06-1.50557538E-08 7.06834189E-12-6.31861166E-16    2
 2.25597004E+05 4.92236293E+00 2.79781357E+00-1.41287178E-03 2.68686998E-06    3
-2.31615591E-09 7.49585578E-13 2.25548731E+05 3.59928845E+00 2.26339616E+05    4
O2+               RUS 89O  2E  -1    0    0G   298.150  6000.000 1000.        1
 3.31675922E+00 1.11522244E-03-3.83492556E-07 5.72784687E-11-2.77648381E-15    2
 1.39876823E+05 5.44726469E+00 4.61017167E+00-6.35951952E-03 1.42425624E-05    3
-1.20997923E-08 3.70956878E-12 1.39742229E+05-2.01326941E-01 1.40937762E+05    4
O+                g 8/97O  1.E -1.   0.   0.G   298.150  6000.000 1000.        1
 2.48542028E+00 2.56978695E-05-1.28833378E-08 1.65525487E-12 1.09933344E-16    2
 1.87940874E+05 4.47425446E+00 2.50000000E+00 0.00000000E+00 0.00000000E+00    3
 0.00000000E+00 0.00000000E+00 1.87935284E+05 4.39337676E+00 1.88680659E+05    4
N2+               tpis89N  2.E -1.   0.   0.G   298.150  6000.000 1000.        1
 3.58661363E+00 2.53071949E-04 1.84778214E-07-4.55257223E-11 3.26818029E-15    2
 1.80390994E+05 3.09584143E+00 3.77540711E+00-2.06459157E-03 4.75752301E-06    3
-3.15664228E-09 6.70509973E-13 1.80481115E+05 2.69322178E+00 1.81551099E+05    4
E  electron gas   g12/98E  1.   0.   0.   0.G   298.150  6000.000 1000.        1
 2.50000000E+00 0.00000000E+00 0.00000000E+00 0.00000000E+00 0.00000000E+00    2
-7.45375000E+02-1.17208122E+01 2.50000000E+00 0.00000000E+00 0.00000000E+00    3
 0.00000000E+00 0.00000000E+00-7.45375000E+02-1.17208122E+01 0.00000000E+00    4
END
```

Figure A.2: Thermodynamic Data [15]

A.2.1 CHEMKIN Input File For Benchmark Analysis

The benchmark analysis has been carried out considering the same thermo.dat file, previously used for the HCM investigation, but a different file for the chemical reactions.

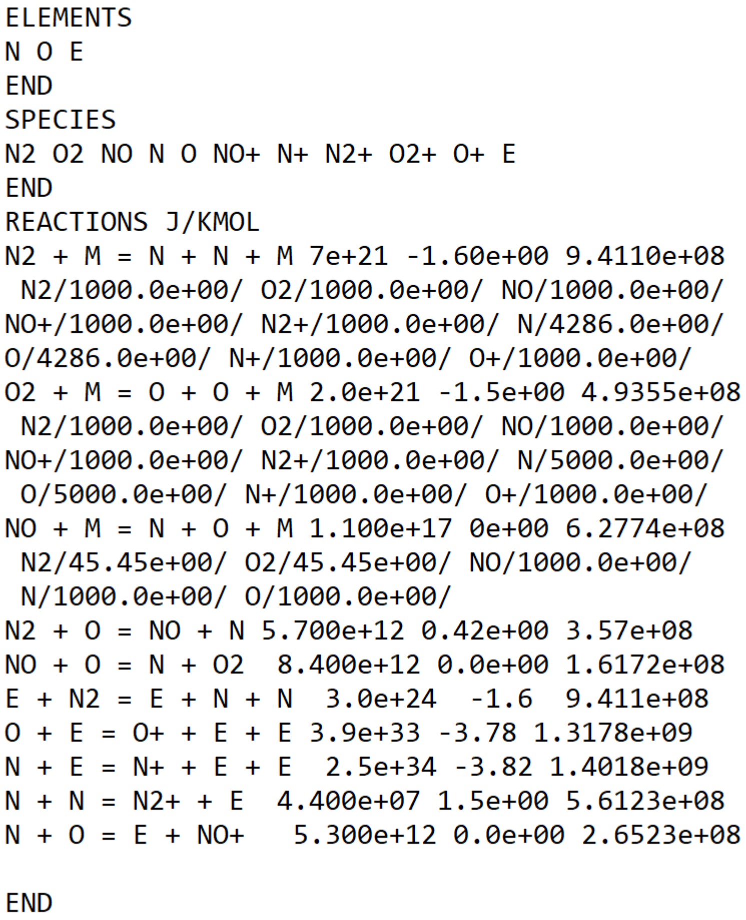

```
ELEMENTS
N O E
END
SPECIES
N2 O2 NO N O NO+ N+ N2+ O2+ O+ E
END
REACTIONS J/KMOL
N2 + M = N + N + M 7e+21 -1.60e+00 9.4110e+08
 N2/1000.0e+00/ O2/1000.0e+00/ NO/1000.0e+00/
NO+/1000.0e+00/ N2+/1000.0e+00/ N/4286.0e+00/
O/4286.0e+00/ N+/1000.0e+00/ O+/1000.0e+00/
O2 + M = O + O + M 2.0e+21 -1.5e+00 4.9355e+08
 N2/1000.0e+00/ O2/1000.0e+00/ NO/1000.0e+00/
NO+/1000.0e+00/ N2+/1000.0e+00/ N/5000.0e+00/
 O/5000.0e+00/ N+/1000.0e+00/ O+/1000.0e+00/
NO + M = N + O + M 1.100e+17 0e+00 6.2774e+08
 N2/45.45e+00/ O2/45.45e+00/ NO/1000.0e+00/
 N/1000.0e+00/ O/1000.0e+00/
N2 + O = NO + N 5.700e+12 0.42e+00 3.57e+08
NO + O = N + O2  8.400e+12 0.0e+00 1.6172e+08
E + N2 = E + N + N  3.0e+24  -1.6  9.411e+08
O + E = O+ + E + E 3.9e+33 -3.78 1.3178e+09
N + E = N+ + E + E  2.5e+34 -3.82 1.4018e+09
N + N = N2+ + E  4.400e+07 1.5e+00 5.6123e+08
N + O = E + NO+   5.300e+12 0.0e+00 2.6523e+08

END
```

Figure A.3: CHEMKIN reactions file for benchmark analysis[16]

Bibliography

[1] MDAA. 3m22 zirkon. URL https://missiledefenseadvocacy.org/missile-threat-and-proliferation/todays-missile-threat/russia/3m22-zircon/.

[2] Kinzhal: un pugnale per il mig-31. *Aeronatuica Difesa N.383*, 2018.

[3] T.S. SubramanianY. Mallikarjun. India successfully test-fires shourya missile. *THE HINDU*, 206.

[4] Richard H Speier, George Nacouzi, Carrie Lee, and Richard M Moore. *Hypersonic missile nonproliferation: hindering the spread of a new class of weapons*. Rand Corporation, 2017.

[5] Amanda Macias. Russia moves 20 hypersonic missiles to testing site, signaling another milestone for the weapons program. *CNBC*, 2019.

[6] Hemant Kumar Rout. India successfully test-fires new nuclear capable hypersonic missile shaurya. *The New India Express*, 2020.

[7] Jiang Zhao and Rui Zhou. Reentry trajectory optimization for hypersonic vehicle satisfying complex constraints. *Chinese Journal of Aeronautics*, 26(6):1544–1553, 2013.

[8] Alessandro Broglia. *Preliminary Design of Waverider Aircraft*. PhD thesis, 04 2016.

[9] Yang Ma, Tao Yang, Zhiwei Feng, and Qingbin Zhang. Hypersonic lifting body aerodynamic shape optimization based on the multiobjective evolutionary algorithm based on decomposition. *Proceedings of the Institution of Mechanical Engineers, Part G: Journal of Aerospace Engineering*, 229(7):1246–1266, 2015.

[10] Zhen-tao Zhao, Wei Huang, Bin-bin Yan, Li Yan, Tian-tian Zhang, and R Moradi. Design and high speed aerodynamic performance analysis of vortex lift waverider with a wide-speed range. *Acta Astronautica*, 151:848–863, 2018.

[11] John D Anderson Jr. *Hypersonic and high-temperature gas dynamics*. American Institute of Aeronautics and Astronautics, 2006.

[12] G Koppenwallner. Fundamentals of hypersonics: aerodynamics and heat transfer. *1984. 61*, 1984.

[13] Millena Martins Villar, Aristeu da Silveira Neto, and Alexandre Megiorin Roma. The multigrid method for the unsteady incompressible navier-stokes equations: Comparative analysis between different cycles and smoothers.

[14] Chul Park. On convergence of computation of chemically reacting flows. In *23rd Aerospace Sciences Meeting*, page 247, 1985.

[15] Alexander Burcat, Branko Ruscic, et al. Third millenium ideal gas and condensed phase thermochemical database for combustion (with update from active thermochemical tables). Technical report, Argonne National Lab.(ANL), Argonne, IL (United States), 2005.

[16] Chul Park. Review of chemical-kinetic problems of future nasa missions. i-earth entries. *Journal of Thermophysics and Heat transfer*, 7(3):385–398, 1993.

[17] Ajey Lele, Lele, and Bose. Disruptive technologies for the militaries and security. 2019.

[18] Corin Segal. *The scramjet engine: processes and characteristics*. Number 25. Cambridge University Press, 2009.

[19] Helley M Sayler. *Hypersonic Weapons: Background and Issues for Congress*. Congressional Research Service, 2019.

[20] Amy F Woolf. Conventional prompt global strike and long-range ballistic missiles: background and issues. LIBRARY OF CONGRESS WASHINGTON DC United States, 2019.

[21] James M Acton. China's advanced weapons. *testimony before the US-China Economic and Security Review Commission, https://carnegieendowment.org/2017/02/23/china-s-advanced-weapons-pub-68095*, 2017.

[22] Steve Trimble. New long-term pentagon plan boosts hypersonics, but only prototypes. *Aviation Week,https://aviationweek.com/defense/new-long-term-pentagon-plan-boosts-hypersonics-only-prototypes*, 2019.

[23] Department of the Navy. Highlights of the department of the navy fy 2021 budget, 2020. URL `https://www.secnav.navy.mil/fmc/fmb/Documents/21pres/Highlights_book.pdf`.

[24] Dylan Malyasov. U.s. army displays model of new hypersonic weapon, 2020. URL `https://defence-blog.com/news/army/u-s-army-displays-model-of-new-hypersonic-weapon.html`.

[25] Stephen Trimble. Lockheed martin claims both usaf hypersonic programmes. *Flight Global,https://www.flightglobal.com/news/articles/lockheed-martin-claims-both-usaf-hypersonic-programm-450968/*, 2018.

[26] Guy Norris. U.s. air force plans road map to operational hypersonics. *Aviation Week, https://aviationweek.com/defense/us-air-force-plans-road-map-operational-hypersonics*, 2017.

[27] Darpa. Tactical boost glide program information, . URL `https://www.darpa.mil/program/tactical-boost-glide`.

[28] Darpa. Operational fires, . URL `https://www.darpa.mil/program/tactical-boost-glide`.

[29] DARPA. Hypersonic air-breathing weapon concept program information. URL `https://www.darpa.mil/program/hypersonic-air-breathing-weapon-concept`.

[30] Global Security. Hypersonic technology vehicle.

[31] Graham Warwick. Darpa refocuses hypersonics research on tactical missions, aviation week & space technology, july 8. 2013.

[32] Guy Norris. X-51a waverider achieves hypersonic goal on final flight. *Aviation Week*, 2, 2013.

[33] Z Rosenberg. Hypersonic x-51 programme ends in success. *Flight International. Accessed online http://www. flightglobal. com/news/articles/hypersonic-x-51-programme-ends-in-success-385481*, 2013.

[34] Steve Trimble. A hypersonic sputnik? *Aviation Week*, 2019.

[35] Dave Majumdar. Russia's lethal hypersonic zircon cruise missile to enter production. *National Interest*, 2016.

[36] Dave Majumdar. Russia: New kinzhal aero-ballistic missile has 3,000 km range if fired from supersonic bomber. *National Interest*, 2018.

[37] Erika Solem and Karen Montague. Chinese hypersonic weapons development. *China Brief*, pages 6–11, 2016.

[38] Ankit Panda. Introducing the df-17: China's newly tested ballistic missile armed with a hypersonic glide vehicle. *The Diplomat*, 28, 2017.

[39] Arka Biswas. China's wu-14 nuclear device: Impact on deterrence equation. *IndraStra Global*, (6): 5, 2015.

[40] Jessie Yeung. China claims to have successfully tested its first hypersonic aircraft, 2018.

[41] Defense News. France studies nuclear missile replacement. *Defense News*, 2014.

[42] Charlie Gao. Meet brahmos ii: The super hypersonic missile russia and india may never build. *The National Interest*, 2019.

[43] Anonymous. Australia and usa in hifire link-up. *Flight International*, 170(5063), 2006.

[44] Guy Norris. Hyper hurdles. *Aviation Week and Space Technology*, 2013.

[45] Tom Forbes David Lewis. Researchers at university of queensland mothball scramjet experiment after failed test in norway. *Australia Broadcasting Corpo- ration News*, 2013.

[46] JAXA. Jaxa 2025(jaxa long-term vision), apr 2009. URL `https://www.youtube.com/watch?v=jgs8G_EScz4`.

[47] Hideyuki Taguchi, Akira Murakami, Tetsuya Sato, and Takeshi Tsuchiya. Conceptual study on hypersonic turbojet experimental vehicle (hytex). *TRANSACTIONS OF THE JAPAN SOCIETY FOR AERONAUTICAL AND SPACE SCIENCES, SPACE TECHNOLOGY JAPAN*, 7(ists26): Pa_27–Pa_32, 2009.

[48] Johan Steelant, Mats Dalenbring, Markus Kuhn, Marc Bouchez, and Jens von Wolfersdorf. Achievements obtained within atllas-ii on aero-thermal loaded material investigations for high-speed vehicles. In *21st AIAA International Space Planes and Hypersonics Technologies Conference*, page 2393, 2017.

[49] Kimberley A Clarke. *Performance optimization study of a common aero vehicle using a legendre pseudospectral method*. PhD thesis, Massachusetts Institute of Technology, 2003.

[50] S Slivinsky, R Galloway, S Breitling, and C Wilborn. Missile technology demonstration 3 (mtd-3) demonstrating global positioning system (gps) technology in an application to range safety tracking and precision guidance, navigation and control. In *Space Technology Conference and Exposition*, page 4432, 1999.

[51] Kenan Zhang and Wanchun Chen. Reentry vehicle constrained trajectory optimization. In *17th AIAA International Space Planes and Hypersonic Systems and Technologies Conference*, page 2231, 2011.

[52] Terry H Phillips. A common aero vehicle (cav) model, description, and employment guide. *Schafer Corporation for AFRL and AFSPC*, 27, 2003.

[53] Frederick Ferguson, Shengyong Zhang, and Hydar Apdin. A design concept for the construction of a complete hypersonic vehicle from 2d flowfields. In *AIAA/CIRA 13th International Space Planes and Hypersonics Systems and Technologies Conference*, page 3363, 2005.

[54] H Sobieczky, FC Dougherty, and K Jones. Hypersonic waverider design from given shock waves. In *Proceedings of the first international hypersonic waverider symposium*, pages 17–19. University of Maryland College Park, MD, 1990.

[55] Ryan P Starkey. Design of waverider based re-entry vehicles. *AIAA/CIRA 13 th International Space Planes and Hypersonics Systems and Technologies*, pages 1–13, 2005.

[56] Konstantinos Kontogiannis, András Sóbester, and Nigel J Taylor. On the conceptual design of waverider forebody geometries. In *53rd AIAA aerospace sciences meeting*, page 1009, 2015.

[57] T. Silvester and Richard Morgan. Computational hypervelocity aerodynamics of a caret waverider. 07 2004. doi: 10.2514/6.2004-3848.

[58] Beom-Soo Kim. *Optimization of waverider configurations generated from non-axisymmetric flows past a nearly circular cone.* PhD thesis, 1983.

[59] Li-li Chen, Xiao-long Deng, Zheng Guo, Zhong-xi Hou, and Wen-kai Wang. A novel approach for design and analysis of volume-improved osculating-cone waveriders. *Acta Astronautica*, 161: 430–445, 2019.

[60] Zhang Zhenming, Liu Yi, and Ding Yunliang. Parametric geometry modeling and shape optimization method for hypersonic flight vehicles [j]. *Journal of Nanjing University of Aeronautics & Astronautics*, 2, 2012.

[61] Zhonghua Han, Keshi Zhang, Wenping Song, and Jun Liu. Surrogate-based aerodynamic shape optimization with application to wind turbine airfoils. In *51st AIAA aerospace sciences meeting including the new horizons forum and aerospace exposition*, page 1108, 2013.

[62] Vis Sripawadkul, Mattia Padulo, and Marin Guenov. A comparison of airfoil shape parameterization techniques for early design optimization. In *13th AIAA/ISSMO multidisciplinary analysis optimization conference*, page 9050, 2010.

[63] Siva Nadarajah, Patrice Castonguay, and Arash Mousavi. Survey of shape parameterization techniques and its effect on three-dimensional aerodynamic shape optimization. In *18th AIAA computational fluid dynamics conference*, page 3837, 2007.

[64] John David Anderson Jr. *Fundamentals of aerodynamics.* Tata McGraw-Hill Education, 2010.

[65] James E House. *Principles of chemical kinetics.* Academic press, 2007.

[66] Ralph H Petrucci, F Geoffrey Herring, Carey Bissonnette, and Jeffry D Madura. *General chemistry: principles and modern applications.* Pearson, 2017.

[67] John D Anderson. *Modern compressible flow.* Tata McGraw-Hill Education, 2003.

[68] DR Stull, H Prophet, et al. Janaf thermochemical tables, nsrds-nbs 37. *Washington, DC*, 1971.

[69] TL Hill. Statistical mechanics; mcgrawhill: New york, 1956. *Kubo, R. J Phys Soc Jpn*, 17:1100, 1962.

[70] Bonnie J McBride. *Thermodynamic properties to 6000 K for 210 substances involving the first 18 elements*, volume 3001. Office of Scientific and Technical Information. National Aeronautics and . . . , 1963.

[71] John David Anderson and J Wendt. *Computational fluid dynamics*, volume 206. Springer, 1995.

[72] Randall J LeVeque et al. *Finite volume methods for hyperbolic problems*, volume 31. Cambridge university press, 2002.

[73] James A Fay and Frederick R Riddell. Theory of stagnation point heat transfer in dissociated air. *Journal of the Aerospace Sciences*, 25(2):73–85, 1958.

[74] Randall J LeVeque and Randall J Leveque. *Numerical methods for conservation laws*, volume 132. Springer, 1992.

[75] Gino Moretti. Computation of flows with shocks. *Annual Review of Fluid Mechanics*, 19:313–337, 1987.

[76] Maurizio Pandolfi and Domenic D'Ambrosio. Numerical instabilities in upwind methods: analysis and cures for the "carbuncle" phenomenon. *Journal of Computational Physics*, 166(2):271–301, 2001.

[77] PLM Siemens. Star-ccm+ documentation. *Siemens PLM Software Inc*, 12, 2017.

[78] Robert C Reid, John M Prausnitz, and Bruce E Poling. The properties of gases and liquids. 1987.

[79] Ya B Zel'Dovich and Yu P Raizer. *Physics of shock waves and high-temperature hydrodynamic phenomena.* Courier Corporation, 2002.

[80] Sydney Chapman, Thomas George Cowling, and David Burnett. *The mathematical theory of non-uniform gases: an account of the kinetic theory of viscosity, thermal conduction and diffusion in gases.* Cambridge university press, 1990.

[81] Robert J Kee, Graham Dixon-Lewis, Jürgen Warnatz, Michael E Coltrin, and James A Miller. A fortran computer code package for the evaluation of gas-phase multicomponent transport properties. *Sandia National Laboratories Report SAND86-8246*, 13:80401–1887, 1986.

[82] Louis Monchick and EA Mason. Transport properties of polar gases. *The Journal of Chemical Physics*, 35(5):1676–1697, 1961.

[83] J Warnatz and N Peters. Numerical methods in flame propagation. *Wiesbaden: Vieweg and Sohn*, 1982.

[84] JG Parker. Rotational and vibrational relaxation in diatomic gases. *The Physics of Fluids*, 2(4): 449–462, 1959.

[85] J Warnatz. Calculation of the structure of laminar flat flames i: Flame velocity of freely propagating ozone decomposition flames. *Berichte der Bunsengesellschaft für physikalische Chemie*, 82(2): 193–200, 1978.

[86] Scott D Cohen, Alan C Hindmarsh, and Paul F Dubois. Cvode, a stiff/nonstiff ode solver in c. *Computers in physics*, 10(2):138–143, 1996.

[87] A Babajimopoulos, DN Assanis, DL Flowers, SM Aceves, and RP Hessel. A fully coupled computational fluid dynamics and multi-zone model with detailed chemical kinetics for the simulation of premixed charge compression ignition engines. *International journal of engine research*, 6(5):497–512, 2005.

[88] Michael F Modest. *Radiative heat transfer.* Academic press, 2013.

[89] Joseph Caniou. *Passive infrared detection: theory and applications.* Springer Science & Business Media, 2013.

[90] LS Rothman, IE Gordon, RJ Barber, H Dothe, RR Gamache, A Goldman, VI Perevalov, SA Tashkun, and J Tennyson. Hitemp, the high-temperature molecular spectroscopic database. *Journal of Quantitative Spectroscopy and Radiative Transfer*, 111(15):2139–2150, 2010.

[91] Nathan Ida and Joao PA Bastos. *Electromagnetics and calculation of fields.* Springer Science & Business Media, 2013.

[92] John David Jackson. Classical electrodynamics, 1999.

[93] Peter J Mohr, Barry N Taylor, and David B Newell. Codata recommended values of the fundamental physical constants: 2006. *Journal of Physical and Chemical Reference Data*, 80(3):633–1284, 2008.

[94] Jonathan M Weiss and Wayne A Smith. Preconditioning applied to variable and constant density flows. *AIAA journal*, 33(11):2050–2057, 1995.

[95] Meng-Sing Liou. A sequel to ausm: Ausm+. *Journal of computational Physics*, 129(2):364–382, 1996.

[96] F Moukalled, L Mangani, and M Darwish. Gradient computation. In *The Finite Volume Method in Computational Fluid Dynamics*, pages 273–302. Springer, 2016.

[97] V Venkatakrishnan. On the convergence of limiters and convergence to steady state solutions. In *AIAA, 31st Aerospace Sciences Meeting*, 1994.

[98] Timothy Barth and Dennis Jespersen. The design and application of upwind schemes on unstructured meshes. In *27th Aerospace sciences meeting*, page 366, 1989.

[99] Noel Black, Shirley Moore, and Eric W Weisstein. Gauss-seidel method. *From MathWorld-A Wolfram Web Resource*, 1:1, 2006.

[100] MT Heath. Scientific computing: An introductory survey. mcgraw-hill. *NY, USA*, 2002.

[101] Pieter Wesseling. Introduction to multigrid methods. Technical report, INSTITUTE FOR COMPUTER APPLICATIONS IN SCIENCE AND ENGINEERING HAMPTON VA, 1995.

[102] Henk A Van der Vorst. Bi-cgstab: A fast and smoothly converging variant of bi-cg for the solution of nonsymmetric linear systems. *SIAM Journal on scientific and Statistical Computing*, 13(2): 631–644, 1992.

[103] Mustafa Cavcar. The international standard atmosphere (isa). *Anadolu University, Turkey*, 30(9): 1–6, 2000.

[104] Engineering ToolBox. Emissivity coefficients materials. 2003.

[105] Roop N Gupta, Kam-Pui Lee, Richard A Thompson, and Jerrold M Yos. A review of reaction rates and thermodynamic and transport properties for an 11-species air model for chemical and thermal nonequilibrium calculations to 30000 k. 1990.

[106] James Ruiz. Hypersonic third body reactions part 1, June 2011. URL `https://support.sw.siemens.com/knowledge-base/KB000039591_EN_US`.

[107] Reaction Design. The chemkin thermodynamic database. *CHEMKIN Collection, Release*, 3, 2000.